A Geochemical and Hydrological Assessment of Oil and Related Compounds from the 2010 Deepwater Horizon Oil Spill in Gulf Coastal Saltmarshes

by

Kirsten Nicole Guerra

A thesis submitted to the Graduate Faculty of
Auburn University
in partial fulfillment of the
requirements for the Degree of
Master of Science in Geology

Auburn, Alabama
December 14, 2013

Approved by

Ming-Kuo Lee, Chair, Professor of Geology and Geography
Jim Saunders, Professor of Geology and Geography
Charles Savrda, Professor of Geology and Geography

Abstract

In April of 2010, the Macondo-1 wellhead ruptured in the Gulf of Mexico, releasing an estimated 4.9 million barrels of crude oil. Ten saltmarsh sites along the northern Gulf coast were investigated to determine the fate, transport, and transformation of oil and metal contaminants associated with the spill. Sites ranged from heavily contaminated (Bay Jimmy North, Bay Jimmy South, Bayou Dulac, and Batiste), moderately contaminated (Walker Island, Point Aux Chenes Bay, and Rigolets), and pristine (Weeks Bay, Longs Bayou, and Bayou Heron).

Weathered oil samples at heavily-contaminated sites were fingerprinted for two targeted biomarkers with special mass-to-charge ratios (m/z). Fragmentograms of m/z 217 and 218 reveal a strong correlation between oiled sediments and original MC-252 crude oil. Tarballs collected from the Alabama coast in September 2012, 28 months after the spill also were fingerprinted to the 2010 Deepwater Horizon spill by fragmentograms of m/z 191, 217, and 218. Isolated plumes of MC-252 spilled oil thus still exist on the Gulf of Mexico seafloor, and it is probable that these oil plumes will continue to wash into coastal regions over time with the aid of storm surges or hurricane activity. Fragmentograms of the tarballs and weathered oil samples both indicate the enrichment of heavier hydrocarbon compounds due to preferential weathering and biodegradation of lighter compounds.

MC-252 crude oil was identified in Gulf coastal sediments at depths down to 15 cm. Saltwater-freshwater dynamics may have played a role in this intrusion of crude oil. Physical tank experiments and numerical modeling both support the viability of two proposed intrusion mechanics: intrusion with a saltwater wedge and downward intrusion with onlapping seawater that infiltrates the sediment surface.

Following the spill in 2010, BP and NOAA applied 2.1 million gallons of COREXIT 9500A to disperse oil slicks throughout the water column. Gas and liquid chromatography-mass spectrometric (GC-MS and LC-MS) analyses of COREXIT 9500A revealed several compounds:

light hydrocarbons, dioctyl sodium sulfosuccinate (DOSS), palmitic acid, and a sulfonic acid base to a series of polyethylene glycols (PEGs). Among these, DOCC will serve as the most effective conservative biomarker to trace the occurrence and geochemical evolution of the dispersant in natural environments.

Inductively coupled plasma-mass spectrometry (ICP-MS) reveals generally low concentrations (a few to hundreds of ppb) of various trace metals in pore waters, despite high levels of those trace metals in sediments. Elevated total sulfur concentrations at contaminated sites and at shallower depths suggest a large influx of sulfur along with crude oil. Low dissolved iron and very high levels of sulfide indicate that bacterial sulfate reduction has fixed most reduced Fe through the formation of iron sulfide solids, such as pyrite. High levels of arsenic and manganese in both sediments and pore water at contaminated sites indicate the influx of these metals with crude oil but suggest the possible sequestration of arsenic into iron sulfide solids.

A series of geochemical models illustrate the probable evolution of oil-inundated saltmarshes. An activity model indicates that pH and H_2S conditions at oiled saltmarshes occur within the stability field of pyrite under reducing conditions (pE = -3). In a system affected by crude oil influx, pyrite is shown to precipitate and hematite to dissolve as conditions transition from oxidizing to sulfate reducing (increasingly negative Eh). Sequestration of metals into pyrite and adsorption to hydrous ferric oxides (HFOs) in coastal marsh sediments may temporarily mitigate groundwater contamination concerns, but geochemical models show that a rise in pH from 7 to 9 would result in the desorption of over 500 μg/kg arsenic into pore waters. Furthermore, competing ions dissolved in seawater may replace arsenic on HFO sorption sites, prompting additional increases of arsenic in solution.

Table of Contents

List of Tables

List of Figures

INTRODUCTION

Petroleum hydrocarbons rank as the most ubiquitous marine contaminant in the world, entering the environment through natural seepages, pollution from ships and ports, pipeline failures, and most notably, deep-water drilling accidents (Cappello et al., 2007). The explosion and subsea rupture of BP's Macondo-1 prospect well on April 20, 2010 resulted in the release of approximately 4.9 million barrels of crude oil over the course of 84 days (Crone & Tolstoy, 2010). Numerous other spills preceded the Deepwater Horizon spill, but none have matched its extent or scale. The amount of crude oil spilled from the Macondo-1 well exceeds the next-largest spill, the 1989 Exxon-Valdez spill, by more than 3.5 times (Maki, 1991; Atlas & Hazen, 2011). Due to our limited knowledge of the fate and transformation of oil in marine and coastal environments, a spill of this magnitude requires further investigation into the extent of environmental effects and improved remediation practices.

The massive amounts of oil released by Macondo-1 into the Gulf met several fates. The immediate response of BP to the crisis was the application of dispersant solutions that served to spread the oil throughout the water column rather than forming a surficial slick (Kujawinski et al., 2011). Still, a slick formed that extended for an estimated 68,000 square miles across the Gulf of Mexico (Amos, 2010). Furthermore, vast quantities of crude oil made their way to the northern Gulf coast of the United States.

The introduction of oil into coastal ecosystems brought on many immediate, damaging effects that have been well documented. Some wildlife populations experienced drastic decreases. Many food sources were threatened through the bioaccumulation of spill-related toxins such as mercury and arsenic (Delaune et al., 2004; Kongchum et al., 2006). Although great emphasis has been placed on the remediation of these immediate concerns, the detrimental effects of sustained contamination should not be overlooked. Iverson et al. (2010) concluded that, in some bird species, cumulative mortality counts from prolonged exposure to oil contaminants likely exceed counts of acute mortality. The culprit behind the continued inimical effects on wildlife in affected areas may be the persistence of heavier oil fragments on coastal sediments. The diminished presence of a once-expansive oil slick and decreased sightings of oil on the land surface suggest near eradication from affected areas. However, distributions of total organic carbon with depth (Natter et al., 2012) clearly indicate that oil contamination penetrates beyond the surface into deeper sediments. The high organic content at oiled saltmarsh sites (Keevan, 2012; Natter, 2012) has been shown to increase the sorption of heavier crude oil compounds onto sediments (Burnol & Charlet, 2010). It is also suspected that dynamics of saltwater intrusion may further exacerbate the oil's penetration into deeper sediments.

Oil contamination in wetlands also has a secondary effect. Wetlands are ecologically important to wildlife and human populations. Often, wetland sediments serve as sinks for trace metals that are transported and deposited by neighboring river systems, reducing the likelihood for those metals to enter the water column and become bioaccumulated through the food chain (Essaid et al., 2011; Ribeiro et al., 2011). Trace metal concentrations are impacted naturally on a small scale by microbes within the wetlands. However, an oil spill provides an overabundance of carbon food supply to the microbes, thereby enhancing microbial activities. Two types of microbes in particular, sulfate-reducing bacteria (SRB) and iron-reducing bacteria (FeRB), have been studied in relation to previous oil contamination events (Kleikemper et al., 2002; Lee & Saunders, 2003) and the Deepwater Horizon oil spill (Keevan, 2012; Natter, 2012; Valentine et al., 2010; Edwards et al., 2011). Toxic metals, such as arsenic and mercury, may desorb from sediment surfaces by bacterial iron reduction and become mobilized in pore water. In contrast, activity of sulfate reducers also may promote the co-precipitation of metals into newly formed biogenic minerals, removing them from pore water (Farquhar et al., 2002). Furthermore, co-precipitation may help to mitigate the high concentrations of trace metals commonly associated with crude oil.

This study aims to assess the geochemical evolution of selected Gulf coastal wetlands that experienced different degrees of oil contamination (Figure 1). At heavily oiled sites, the biotransformation and persistence of heavier crude oil compounds was assessed using

specific petroleum biomarkers (i.e. terpane, hopane, and steranes). These biomarkers show strong resistance to environmental alteration as compared to most organic compounds, thus providing a reliable way to correlate the spilled oils with their initial source. The chemistry of dispersants also was explored through a combination of liquid and gas chromatography-mass spectrometry (LC-MS and GC-MS) in an effort to determine the most effective method for assessing their occurrence and potential evolution in coastal marsh sediments. Additionally, the concentrations of trace metals in sediments and extracted pore waters were measured to assess the mobility and cycling of metals at heavily oiled sites. Finally, this study considers potential hydrological and geochemical methods for improved remediation. A physical tank model and corresponding numerical models were created to investigate the hydrodynamics of interactions between oil, saltwater, and fresh water. Geochemical modeling also was conducted to investigate the biogeochemical changes of sediment and pore waters in response to the inflow of seawater and spilled oil. The geochemical models simulate (1) the effects of saltwater intrusion on metals desorption from iron oxides, and (2) the effects of oil-induced, bacterial sulfate-reduction on reactions and mobility of metals. A clear understanding of these interactions reveals the potential transformation of oils and metals in saltmarsh environments. The data provide critical information to implement long-term remediation and restoration strategies for Gulf coastal marshes.

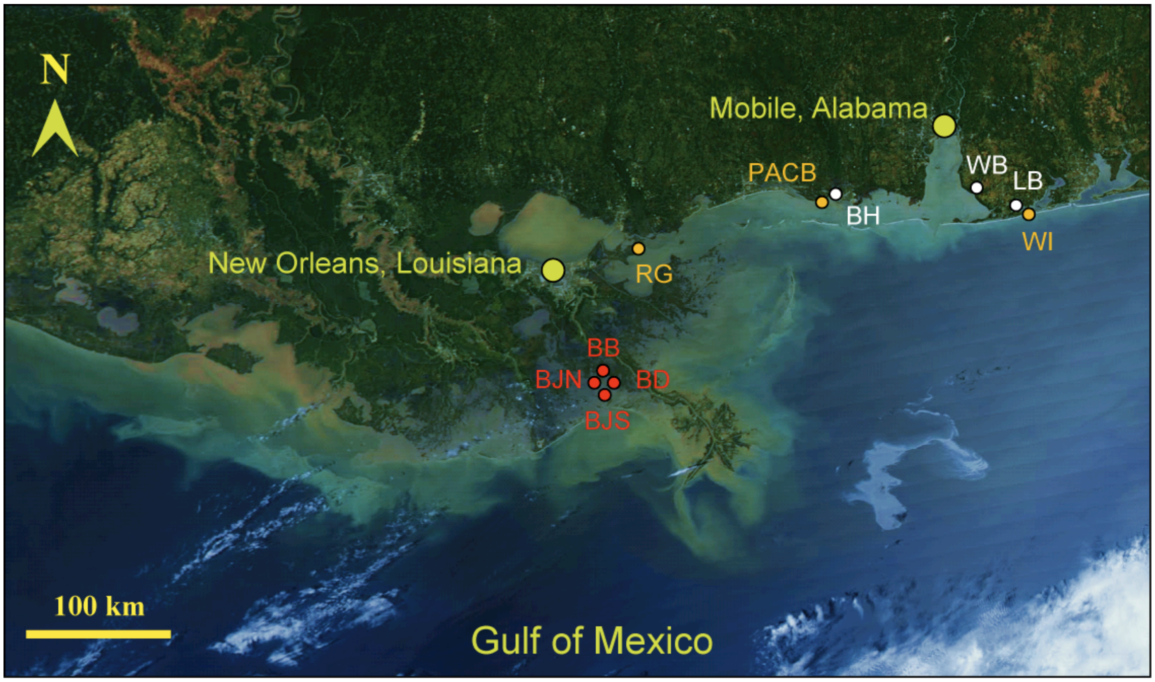

Figure 1. Map of coastal saltmarsh sampling sites along the northern Gulf of Mexico. Red, yellow, and white labels indicate heavily-contaminated, moderately-contaminated, and unaffected sites, respectively (after Natter et al., 2012).

BACKGROUND

Geologic Setting

This study focuses on the effects of the Deepwater Horizon oil spill in typical saltmarshes across the northern Gulf of Mexico. All sampling sites are located within wetlands along the coasts of Louisiana, Mississippi, and Alabama. These wetlands and surrounding coastal plains are covered in Holocene alluvium, deposited by rivers that feed into the Gulf of Mexico. Because the core samples only penetrate 30 cm into the uppermost layer, the Holocene alluvium is the main focus in this study. The alluvium consists of fine- to medium-grained quartz sand, silt, and clays. Sediments in the coastal region also exhibit relatively high organic content, which is significant to the capacity of oil and metals sorption.

Wetlands commonly act as the ultimate sinks for many trace metals that are transported and deposited by neighboring river systems (Essaid et al., 2011). By sorbing to the minerals of wetlands, many trace metals are effectively removed from the water column, reducing the risks of bioaccumulation (Ribeiro et al., 2011). Many of the factors that control metals cycling are highly dependent on a region's geochemical conditions. The waters of saltmarshes are typically anoxic and generally maintain a pH lower than that of seawater. Additionally, saltmarshes are rich in nitrogen and phosphorous, essential nutrients for effective microbial respiration (Cappello et al., 2007).

A thorough characterization of each sampling site is presented in the theses of Jeff Keevan (2012) and Mike Natter (2012), including mineralogy, grain-size distribution, total organic carbon contents, and bulk geochemistry of sediments.

Crude Oil

The crude oil released by the ruptured Macondo-1 well was classified as a light, mature crude with an API gravity of 38.8° (Rosenbauer et al., 2010). Crude oil can be an incredibly complex mixture, consisting of an immense variety of hydrocarbon and non-hydrocarbon components. The basic structure of most crude oil compounds is an isoprene (or isoterpene), C_5H_8. Multiple isoprenes are bound together to form an isoprenoid (or terpenoid), $(C_5H_8)_n$. An infinite number of isoprenoids can be created from any quantity of isoprenes and their many possible configurations. For example, the compound $C_{30}H_{62}$ alone can form as 4,111,846,783 unique structures. Additionally, isoprenoids may bond with other atoms such as nitrogen, oxygen, and sulfur to form over 20,000 distinct compounds in various forms of $C_cH_hN_nO_oS_s$ (Marshall, 2004). Various metals are also commonly associated with crude oil, including Ni, V, Fe, Ba, Al, Cr, Cu, and U (Karchmer & Gunn, 1952; Ball et al., 1960).

The primary classification of hydrocarbons is based on their fundamental structures: saturates are straight and branched chains; olefins are unsaturated structures with double carbon bonds; aromatics are conjugated rings of unsaturated bonds; polar resins have polar substituents; and asphaltenes are polar with very high molecular weights (Wang & Stout, 2007). The scope of this study is limited primarily to the saturate subgroups of terpanes, hopanes, and steranes, but one group of aromatics also is considered. Owing to their carcinogenic nature, polycyclic aromatic hydrocarbons (PAHs) are an important component of crude oil. PAHs have low volatility, decreasing their likelihood to evaporate, and some PAHs are highly resistant to degradation (Arulazhagan et al., 2010). These characteristics amplify the potential of PAHs to remain trapped within coastal sediments for extended periods. Oudot and Chaillan (2010) determined that only 82% of aromatics from the Amoco-Cadiz spill had biodegraded 23 years after the initial spill.

The most common cyclic isoprenoids to occur in crude oil are limited to 5-6 carbons. By contrast, terpanes range from 15-30 carbons, hopanes contain 27-35, and steranes contain between 21-30 (Wang & Stout, 2007). Therefore, hopanes, terpanes, and steranes occur in immensely more varieties that are each highly representative of their sources. It is this uniqueness in source specificity that allows for oil-to-oil correlation, or hydrocarbon fingerprinting.

The practice of hydrocarbon fingerprinting was developed in the 1970's by Chevron Corporation. It was developed for purposes of petroleum exploration, but its application also translates to environmental forensics. Fingerprinting serves to identify a likely source by characterizing the presence of specific biomarkers and their abundance. The chemistry of biomarkers in crude oil is strongly influenced by the primary controls of source-rock lithology and organic composition. However, their chemistry can be significantly impacted by later transformation through the secondary controls of in-reservoir alteration, evaporation, and biodegradation (Wang & Stout, 2007). In instances of environmental forensics, such as the Deepwater Horizon oil spill, abundances of certain biomarkers also can characterize the degree of degradation experienced by the hydrocarbons (Rosenbauer et al., 2010; Natter et al., 2012).

The most common approach to hydrocarbon fingerprinting is through gas chromatography-mass spectrometry (GC-MS) (Wang et al., 2003). Due to the high volatility of many compounds in crude oil, ions will elute through spectrometry after different dwell times based on their mass to charge (m/z) ratio. Lighter ions, those with lower m/z ratios, tend to elute earlier in the process than heavier compounds. Fingerprinting studies typically focus on several specific m/z ratios, as those ratios are known to contain especially meaningful biomarkers. The most common include the hopane and terpane biomarkers of m/z ratio 191 and the steranes of m/z ratios 217 and 218. Analysis of a crude oil sample with GC-MS takes about 1-2 hours and results in chromatographs like those in Figures 2 and 3. GC-MS chromatographs depict the time of flight and intensities for a wide range of ion m/z ratios. For a more detailed analysis that focuses the entire run-time on a single m/z ratio, the oil sample is run through GC-MS selected ion monitoring (GC-MS-SIM). With GC-MS-SIM, the instrument's heightened sensitivity to a single m/z ratio provides a more accurate quantification of the target ion (Wang, 2007).

Environmental applications of hydrocarbon fingerprinting begin with the characterization of the original source crude. In a previous study, Natter et al. (2012) analyzed via GC-MS a pure crude oil sample from the Macondo-1 wellhead (Figure 2). Next, Natter et al. (2012) analyzed the full GC-MS chromatograph of a weathered oil sample from the heavily-contaminated surface sediments at the Bay Jimmy South site (Figure 3). For further correlation, Natter et al. (2012)

used GC-MS-SIM to specifically analyze the 191 ratio biomarkers in a sample of Macondo-1 crude (Figure 4) and weathered oil recovered from plants at Bay Jimmy South (Figure 5). The full suite of 191 fragmentograms for all other sampling sites related to this study can be found in Natter et al. (2012). The results of m/z 191 are very encouraging, so this study will further test the correlation by evaluating sterane biomarkers (i.e. m/z 217 and 218) in the initial crude oil and weathered oils.

Keevan (2012) and Natter (2012) drew several conclusions based on the comparisons between the pure crude from the Macondo-1 source and the weathered crude collected along the coastal wetlands. Foremost, the presence of numerous unique biomarkers in both the pure and weathered crude oil indicates with high certainty that the oil inundating this study's Gulf coastlines is in fact sourced from the Deepwater Horizon wellhead. Furthermore, the relatively low intensities of light hydrocarbon compounds to heavy compounds indicate incomplete degradation of the spilled oil in saltmarsh sediments. Heavier compounds dominate the fraction of oil persisting in affected sediments.

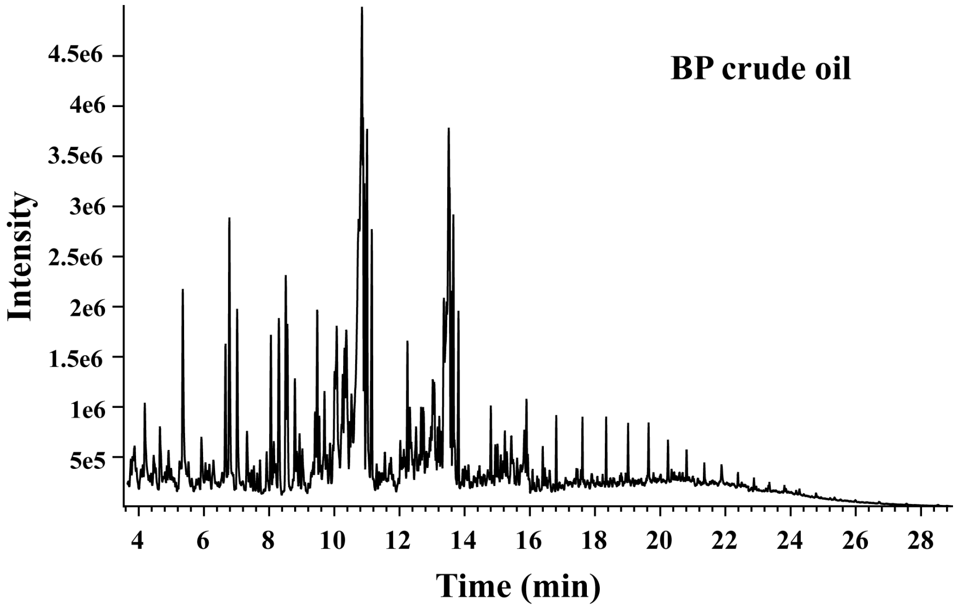

Figure 2. GC-MS chromatograph of the original crude oil spilled from the Macondo-1 well (from Natter et al., 2012).

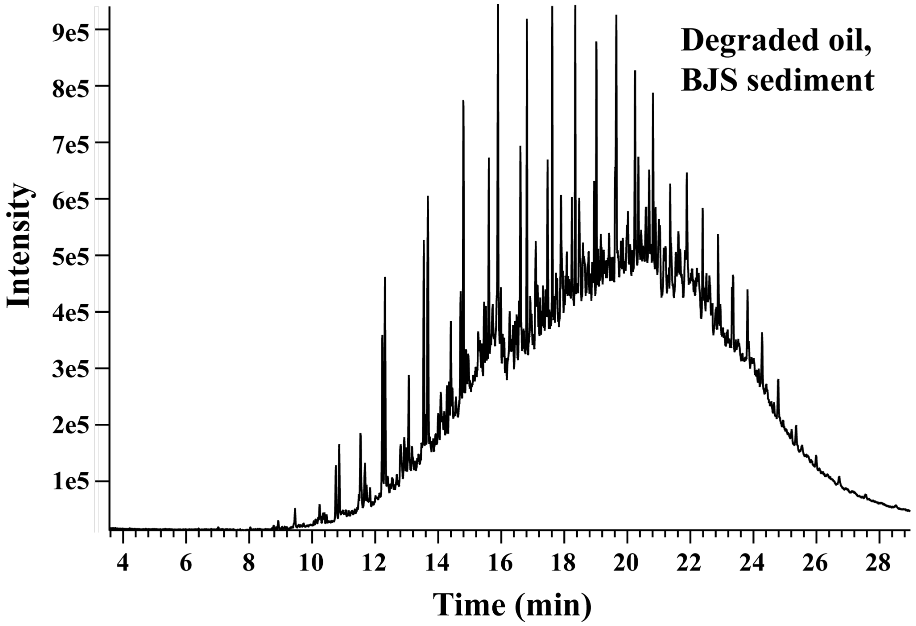

Figure 3. GC-MS chromatograph of weathered oil collected from surface sediments in Bay Jimmy South (from Natter et al., 2012).

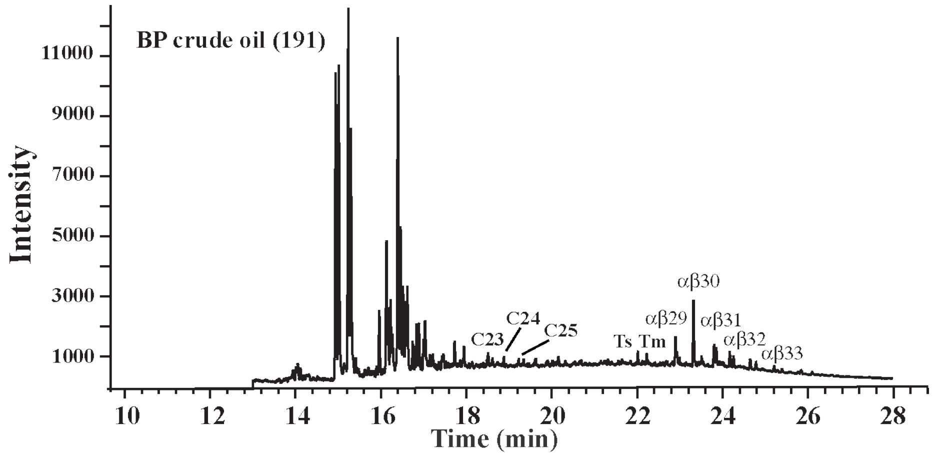

Figure 4. GC-MS-SIM fragmentogram focusing on target ion m/z 191 of the original crude oil spilled from the Macondo-1 well (from Natter et al., 2012).

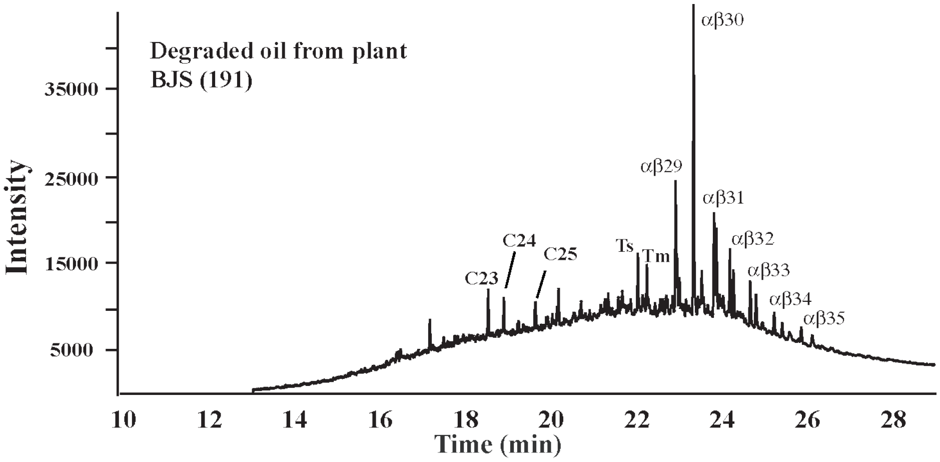

Figure 5. GC-MS-SIM fragmentogram focusing on target ion m/z 191 of surface sediments from Bay Jimmy South (from Natter et al., 2012).

Dispersants

BP, in coordination with NOAA, implemented several oil-remediation strategies following the severance of the Macondo-1 well. Due to the lack of knowledge or experience with such an expansive oil spill, remediation efforts were unprecedented. Public outcry for immediate action led to the use of potentially harmful dispersants that never before had been tested on such a large scale.

The purpose of the applied dispersants was to prevent accumulations of oil with higher molecular weight in the water column or at the water's surface. A dispersant has two main components: (1) a surfactant and (2) a hydrocarbon-based solvent (Judson et al., 2010). The surfactant induces emulsification by coating the surface of the crude oil and lowering the tension at the interface between the oil and surrounding water. Once emulsified, the oil is no longer immiscible with water and can move freely throughout the water column. The goal for the application of these dispersants was to hinder the formation of large, highly viscous oil slicks that could blanket coastlines and harm aquatic life.

Remediation efforts included the release of 2.1 million gallons of dispersant into the Gulf of Mexico between May 15th and July 12th of 2010. Small aerial vessels released 1.4 million of those gallons at the surface in the form of dispersants COREXIT 9500A and COREXIT 9527. The other 0.77 million gallons were released at the wellhead via a jet that ejected COREXIT 9500A directly into the stream of flowing crude oil (Kujawinski et al., 2011).

Figure 6. Dispersants COREXIT 9500A and COREXIT 9527 as applied by seaplanes and pumped directly into flow from the wellhead.

Dispersants have been utilized in previous oil spills but never to the extent that they were in the 2010 Deepwater Horizon oil spill. Very little was known about secondary effects of these dispersants, and even less was known about their fate and transformation at such a large scale. A study conducted by the EPA (2010) on small silverside fish and mysid shrimp indicated no endocrine disruption; however, other studies suggest that there may be some negative environmental impacts associated with the dispersants COREXIT 9500A and COREXIT 9527. The component *nonylphenol ethoxylate* (NPE) of various dispersants, including COREXIT 9500A, has been reported as cytotoxic to mammalian endocrine cells (Judson et al., 2010). Additionally, dispersants may have greater effects on small life forms. Hamdan and Fulmer (2011) report that COREXIT 9500A is highly toxic to some microbial communities that are directly involved in natural hydrocarbon degradation. Studies by BP (2010b) indicate that COREXIT 9500A is the least harmful choice among dispersants. By contrast, Judson et al. (2010) suggests dispersants JD 2000 and SAF-RON GOLD as safer alternatives.

Although the composition of COREXIT 9500 is available on the USEPA website and in other publications (Singer et al., 1996; Judson et al., 2010; Place et al., 2010), very little is known about its chemical evolution in natural environments. Kujawinski et al. (2011) indicated that some degradation-resistant ingredients in dispersants (e.g., dioctyl sodium sulfosuccinate) may be used as a conservative biomarker to trace their transport in natural environments. Place et al. (2010) presented biomarker standards of COREXIT dispersants associated with m/z 81 and 241 using negative-ion detection mode.

It is suspected that COREXIT dispersants may have migrated with crude oil toward the southeastern US coastlines, affecting several of the heavily-contaminated sites included in this study: Bayou Dulac, Bay Jimmy North, and Bay Jimmy South. This study analyzed a pure sample of COREXIT 9500 by LC-MS and GC-MS to characterize its chemical make-up. In a related study, Dr. Elizabeth Kujawinski of Woods Hole Oceanographic Institute (WHOI) is developing a new protocol to extract and analyze adsorbed dispersant from oiled wetland sediments. Collectively, these studies allow for the determination of the occurrence, fate, and transformation of dispersants in oiled marsh environments.

Metals & Metalloids

Around the world, arsenic contamination of groundwater systems represents a potential health hazard. The health effects of arsenic poisoning are severe but delayed by 5-20 years, and it is therefore difficult to determine the scale of the problem. Arsenic enters the groundwater naturally and through various anthropogenic practices (Smedley and Kinniburgh, 2002; Saunders et al., 2008). Natural arsenic contamination occurs in many countries, including the United States, Argentina, Thailand, China, and most notably, Bangladesh. Many communities along floodplains experience problems with arsenic contamination as a result of reductive interactions between organic matter and minerals, which provide sorption surfaces for arsenic.

In solution, arsenic may appear in a variety of oxidation states depending upon its origin. Often, As(V) occurs as the charged anionic complex AsO_4^{3-}. As(III) commonly appears as the charged anionic species, $As(OH)_4^-$, or as the neutral species, $As(OH)_3$. Due to the neutral or relatively low charges of arsenite complexes, As(III) tends to be more mobilized in solution.

Concentrations of arsenic in groundwater systems are controlled by two main processes: adsorption reactions and co-precipitation. The surfaces of minerals and amorphous precipitates often carry a slight charge, which encourages the adsorption of dissolved ions from solution onto those surfaces. The net surface charge of a mineral is determined by its chemistry and other environmental factors, such as pH. In the case of arsenic, which typically occurs as anionic complexes, surfaces with a positive net charge, such as Fe- and Mn-oxides, will yield greater rates of adsorption. Arsenic and other trace metals may adsorb to a variety of phases, such as silicates, organic matter, pyrite, or iron oxides, but the interactions between metals and many of these phases have not been fully characterized. The sorption reactions that have been most thoroughly discussed are those of iron oxides (Dzombak & Morel, 1990). The sorption reactions of iron oxides are especially fundamental, as iron oxides are a ubiquitous mineral coating in various hydrogeologic environments (Hinkle, 1999).

The interactions between arsenic and sorption surfaces are highly pH dependent (Saunders et al., 2003). Generally, the net surface charge of an iron oxide transitions from positive to negative as pH increases in the range of 6 to 9 (Dzombak & Morel, 1990). Therefore, sorption concentrations of anionic arsenic complexes on iron oxide surfaces decreases with increasing pH in the same range. Negatively-charged As(V) could desorb strongly when pH reaches the desorption front of about 8.5 (Lee et al., 2005). This concept is especially important in the saltmarsh sediments of this study due to the potential threat of rising pH through saltwater intrusion (pH of 8–8.4).

Factors other than pH also affect the fate and mobility of arsenic in geologic environments. Dissolution of minerals that provide sorption sites decreases the available surface area on which ions such as arsenic may adsorb. Ions adsorbed to a mineral's surface also may be replaced by more kinetically favored ions. For example, a typical saltwater contains high concentrations of dissolved ions (e.g. silicate, carbonate, calcium, sulfate, etc.) that may compete with arsenic for sorption sites on hydrous oxides (Bethke, 2008; Tyrovola and Nikolaidis, 2009). When such a saltwater is introduced into a freshwater system, the competition between ions results in desorption of existing adsorbed ions from charged mineral surfaces. Similarly, when investigating the geochemical evolution of an area impacted by an oil spill, it is important to consider the effect of newly-introduced ions that commonly occur in crude oil. The influx of oil-associated metals Ni, V, Fe, Ba, Al, Cr, Cu, and U (Karchmer & Gunn, 1952; Ball et al., 1960) may compete with existing sorbate for a limited number of sorption sites.

The other primary control on dissolved arsenic concentrations is mineral precipitation. Arsenic is a main structural component of many minerals: arsenopyrite (FeAsS), realgar (AsS), orpiment (As_2S_3), and others. In other cases, arsenic ions and their complexes adsorb to a variety of mineralogic and organic surfaces. However, small changes in physiochemical and redox states may cause the dissolution of a mineral and thereby reduce the available sorbing surface area. The dissolution of existing arsenic-bearing minerals mobilizes high concentrations of arsenic into solution. Conversely, the precipitation of arsenic-bearing minerals removes arsenic from solution. When incorporated into a mineral's structure or bound to a mineral's surface, arsenic is removed as a hazard from potential drinking water sources. Many studies have shown the strong control of redox conditions on the inclusion of trace metals during pyritization (Berner, 1970; Morse &

Luther, 1999; Saunders et al., 2008; Ye, 2010). In this study, the most important consideration is the effect of redox conditions induced by microbial activity following an oil spill.

Hydrous ferric oxides and iron sulfides often have strong reactions with many metals and metalloids. Aside from arsenic, this study also considers Cu, Pb, Co, Zn, Cr, and Mn. The interactions between pyrite and various trace metals have been thoroughly studied. The degree of pyritization (DOP) is a function of acid volatile sulfides, redox conditions, and pore-water metal concentrations (Ye et al., 2010). Ye et al. (2011) showed that the DOP in subtidal zones was primarily controlled by concentrations of iron and sulfur rather than other reactive trace metals. Still, the DOP is strongly linked to the degree of trace metal pyritization (DTMP) in many cases. Both the DOP and DTMP are especially augmented in anoxic conditions (Alvarez-Iglesias, 2008; Ye et al., 2010), such as those common to wetlands. The limitation of iron relative to sulfur, which is also a common condition of wetlands, is another major contributor of low pyritization (Huerta-Diaz 2010).

Copper (Cu) is strongly favored thermodynamically and kinetically to associate with pyrite, and the DTMP of Cu is especially high closer to the sediment surface (in the 6-8cm range) (Alvarez-Iglesias, 2008) noted. Mercury (Hg) also exhibits a very high DTMP, although its exact association with pyrite is difficult to measure and therefore remains unclear. Based on kinetics, Hg likely precipitates as a sulfide solid (cinnabar, H_2S) prior to the precipitation of pyrite (Ye et al., 2010). However, Hg also may co-precipitate with pyrite or intermediary FeS minerals (Natter, 2012).

Manganese (Mn) and chromium (Cr) consistently display low DTMP. However, both are commonly found sorbed to the surfaces of silicates (Alvarez-Iglesias, 2008). Additionally, the kinetics of Mn suggest incorporation into carbonates prior to pyritization (Otero et al., 2003), and Cr has a very high affinity for organic matter relative to other dissolved metals (Alvarez-Iglesias, 2008). Kinetically, associations between Cr and S are highly unfavorable, and any chromium within pyrite is likely a product of isomorphic substitution (Otero et al., 2003).

Iron- and Sulfate-Reducing Bacteria

An oil spill affects dissolved metal concentrations in wetlands in two ways. First, crude oil commonly contains many metals, and those metals may be directly introduced into wetlands through the physical migration of an oil slick. Second, an oil spill enhances microbial activity, which indirectly affects dissolved metal concentrations by altering geochemical conditions to the point of mineral dissolution or precipitation.

Microbial respiration follows the same basic process, whether authigenic or anthropogenic; it is merely augmented by the introduction of spilled hydrocarbons. After oxidation of a hydrocarbon by sulfate-reducing bacteria (SRB) or iron-reducing bacteria (FeRB) (Edwards et al., 2011), the final step of the electron transport chain is the deposition of the remaining electron onto a terminal electron-accepting phase (TEAP). SRB deposit electrons onto dissolved sulfate (SO_4^{2-}), which is then reduced from 6+ to 2- and becomes a sulfide species. Similarly, FeRB (e.g., *Geobacter*), deposit electrons onto the iron of ferric minerals, reducing the iron's oxidation state from 3+ to 2+ (Essaid et al., 2011). The reduction of iron creates instability within a mineral's structure, causing it to dissolve. Saunders et al. (2008) showed that, with the addition of an artificial source of carbon to simulate an oil spill, dissolved concentrations of ferrous iron (and also arsenic) increased dramatically as a result of enhanced FeRB activity.

The activity of microbes, which feed on organic carbon, is strongly influenced by massive releases of hydrocarbons. Following an oil spill, the mass influx of hydrocarbons into coastal marshes enhances microbial respiration to unnaturally-high levels. As a result of the Deepwater Horizon spill, microbial respiration in the oil slick near the wellhead increased by a factor of approximately five (Edwards et al., 2011). However, the study led by Edwards was focused in a deep-water region relatively devoid of microbial nutrients (2011) as compared to shallower, nitrogen- and phosphorous-rich Gulf settings (Cappello et al., 2007) where the samples for this study were collected. Therefore, it is probable that microbial activity in the coastal saltmarshes of this study also was augmented significantly (Natter et al., 2012).

As Saunders et al. (2008) showed, the enhanced respiration of FeRB leads to high concentrations of dissolved ferrous iron from the dissolution of ferric minerals. Along with the ferric minerals, other metals within the mineral's structure or metals adsorbed to the mineral's surface enter solution. However, continued microbial activity also can stimulate the reverse effect. Through the dissolution of ferric minerals and reduction of dissolved sulfate, microbial respiration provides an ample source of reduced iron and sulfur, which allows for the precipitation of new minerals. The precipitation of pyrite (FeS_2) may decrease the concentrations of dissolved metals with high DTMP through co-precipitation or adsorption.

Framboidal pyrite, thought to form biogenically or authigenically in sediments, was found primarily at those sites most heavily contaminated: BD, BB, and BJN (Keevan, 2012; Natter, 2012). Framboidal pyrite also was recovered from the upper sediments of a core from the Weeks Bay (WB) site. The biomineralization of framboidal pyrite suggests that sulfate-reducing conditions are well established in the salt marsh sediments (Wilkin et al., 1997). Through laser ablation ICP-MS of individual pyrite crystals (Figure 7), Keevan (2012) and Natter (2012) showed that the stoichiometry of the framboidal pyrite consisted primarily of Fe and S. The samples also contain elevated amounts of Mn, Pb, Zn, and V (average concentrations > 1,000 mg/kg) and various amounts of Co, Ni, Cu, As, Se, Hg, Mo, and Cd (ranging from a few to hundreds of mg/kg). They conclude that sulfides produced from sulfate reduction also may react with dissolved metals to form insoluble metal sulfides; such a reaction would decrease the concentrations of dissolved metals by sequestering them in the insoluble metal sulfides.

ICP-MS studies of sediments were carried out to characterize the metal concentrations in saltmarshes across the Gulf coast (Keevan, 2012). The ICP-MS determinations of metal contents in sediments generally occur on the scale of ppm. Another apparent trend occurs with depth; Keevan (2012) and Natter (2012) report that concentrations of some metals (e.g. Fe, S, Pb, Co, As, and Hg) increase with depth in the range of 0-15cm but most metals decrease with further depth in the range of 15-30 cm. Higher concentrations toward the middle of their sediment cores may be attributed to oil intrusion processes, and the slight enrichment of metals in the upper 20 cm of sediments is hypothesized to be a result of increased industrial activity in the last 100 years (Keevan, 2012). In general, the concentrations of many elements (e.g., Ni, Cu, Pb, Zn, Sr, Co, V, Ba, Hg, As, S, and Fe) displayed a positive correlation with the degree of oil contamination. Metal concentrations at heavily-oiled sites were notably higher than those at pristine sites. Keevan (2012) and Natter (2012) noted that the average grain size of wetland sediments plays a major role in the retention of metals; generally, finer grains more surface area for metal sorption.

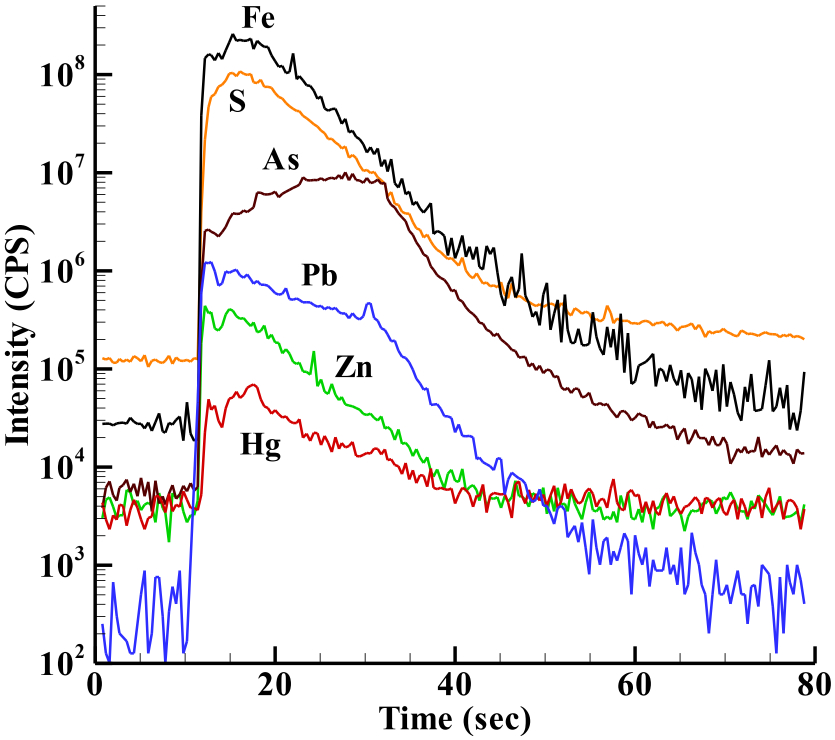

Figure 7. Laser ablation ICP-MS graph of a single pyrite crystal from a sediment core at a depth of <20 cm in Weeks Bay (from Keevan, 2012).

METHODOLOGY

Sample Collection

In October of 2010 and January of 2011, Jeff Keevan and Mike Natter collected the saltmarsh sediment and pore-water samples analyzed in this study. The samples, collected from various locations around Barataria Bay, Louisiana, were heavily contaminated by the Deepwater Horizon oil spill. The sites of sample collection are illustrated in Figure 1. At each site, samples were collected in the form of 30 cm cores, containing bulk sediments and pore water. Water quality parameters (e.g. pH, DOC, H_2S etc.) of surface water were measured at each sampling site via in-situ readings using a TROLL 9000. After collection, core samples were quickly transported to a nearby wet chemistry lab at the Stennis Space Center for processing. Further details on sample collection, including sample processing and storage procedures, can be found in Natter (2012) and Keevan (2012).

In late August of 2012, Hurricane Isaac made contact with the US Gulf coast. Isaac's intensity spurred the relocation of tar balls from the ocean floor onto coastal beaches. On September 4, 2012, tarball samples were collected from a shoreline in Gulf State Park, Alabama at (30.2490°, -87.6682°). The tarballs were bagged and preserved in a freezer until the time of analysis.

Physical Tank Experiments

Several analyses were performed on the effects of saltwater and oil intrusion using a hydrologic tank model. The setup of the artificial aquifer tank is shown in Figure 8. The tank was initially developed by Matt Obley, a physics specialist with the Alabama Science in Motion program, to study the effect of sea-level rise on saltwater intrusion (Lee, et al., 2012). The artificial aquifer is 54.6 cm long (in the flow direction), 27 cm high, and 2.5 cm wide.

The main aquifer chamber is packed with small glass beads and connected to constant-head freshwater and saltwater reservoirs by permeable screens. Overflow outlets positioned at varying levels can adjust water levels in both freshwater and saltwater reservoirs. The freshwater chamber acts as an up-gradient recharge source. Freshwater enters the sand chamber and migrates toward the saltwater chamber at a fixed hydraulic gradient to establish a steady-state flow across the main sand chamber. Saltwater intrusion can be initialized by injecting saltwater into the saltwater chamber.

Several experiments were run using the tank model. Between each experiment, the tank was cleaned and reset to the state in Figure 8. In the preliminary experiments, differences in the toe of the saltwater/freshwater interface due to adjustments in saltwater head were measured with respect to time. Once interfaces were established, a separate source of saltwater (dyed blue) was introduced into the system from directly above the sand chamber. Experiments were designed to test the likelihood of saltwater and oil intrusion dynamics in coastal environments.

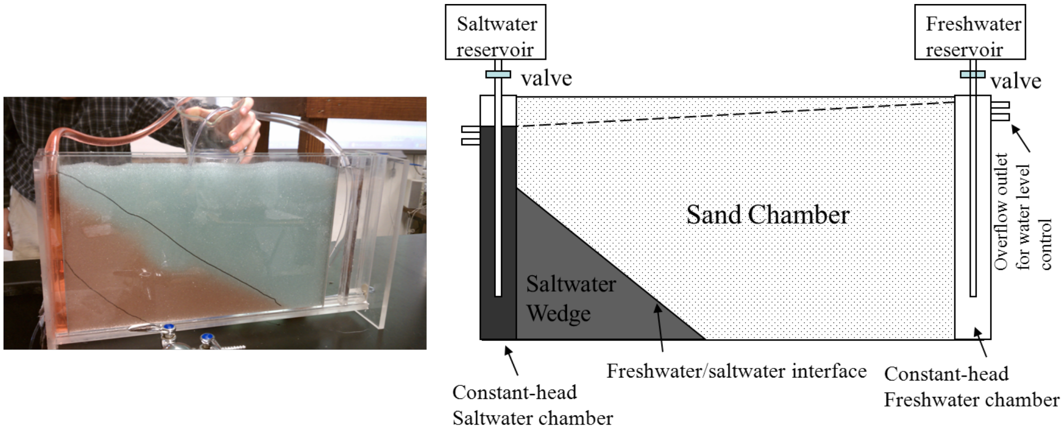

Figure 8. Photograph and diagrammatic illustration of tank model for experimentation into the effects of saltwater hydrodynamics on oil intrusion.

A constant-head permeameter was used to determine the hydraulic conductivity of the glass beads used in tank experiments. The permeameter setup is shown in Figure 9. The glass beads are encased in a cylindrical chamber with a diameter of 6.4 cm, height of 12.5 cm, and a total area of 402.1 cm^2. Several experiments were run at various head values, each for three minutes. For each experiment, the amount of discharge from the permeameter was measured and recorded to the nearest milliliter. Hydraulic conductivity values were calculated according to Darcy's law:

$$K = \frac{Q * L}{A * \Delta h}$$

where K = hydraulic conductivity (m/s); Q = discharge (m^3/s); L = length of chamber (m); A = cross-sectional area of chamber (m^2); and Δh = the difference in constant heads between input and output (m).

Figure 9. Photograph of permeameter setup. Water flows from a set head through a hydraulic chamber and collects in a bucket.

Hydrologic Modeling

Numerical modeling was conducted using Basin2 (Bethke et al., 2003) to mimic the physical tank experiments. The input files used to generate the groundwater and solute transport models can be found in Appendix 3. The fundamentals of the model, outlined in Figure 10, were defined to closely resemble the idealized physical properties of the tank model. The computer model was created with the same dimensions as the tank, and the average hydraulic conductivity value was set close to that of a silty sand in coastal aquifers. Nodal spacing was constructed with 40 nodes in the flow direction (x) and 16 nodes in the direction of depth (z).

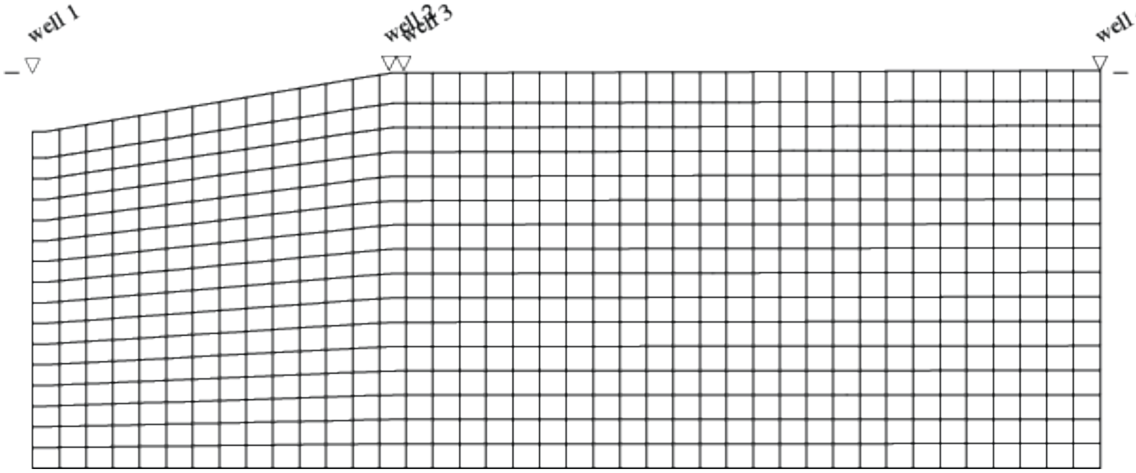

Figure 10. Finite difference grid used in Basin2 numerical simulations, displaying nodal structure and well placement. 60x34 cm. Ocean and seafloor are located on the left side.

The Basin2 model was run to simulate the same saltwater intrusion dynamics revealed in the tank experiments. To model groundwater flow and solute transport, which are controlled by diffusion, dispersion, and advection, Basin2 solves the following partial differential equation in the two-dimensional form:

$$\frac{\partial}{\partial t}(C) = \frac{\partial}{\partial x}D_x(\frac{\partial C}{\partial x}) + \frac{\partial}{\partial z}D_z(\frac{\partial C}{\partial z}) - q_x(\frac{\partial C}{\partial x}) - q_z(\frac{\partial C}{\partial z})$$

where C is concentration (mol/cm^3), q is specific discharge (cm/s), t is time (s), and D is the hydrodynamic dispersion coefficient (cm^2/s) that accounts for both mechanical dispersion and molecular diffusion (Penny et al., 2003).

Geochemical Modeling

Geochemist’s Workbench (GWB) (Bethke, 2008) was used to calculate mixing of freshwater and saltwater and potential geochemical evolution of saltmarsh sediments and pore water in areas impacted by the Deepwater Horizon spill. GWB sub-program Act2 was used to plot the stability fields of iron under varying pH and concentrations of H_2S. Basic parameters used in the models, such as pE or Eh, were estimated as closely as possible based on field measurements of Eh in similar reducing waters. Temperature and pressure were set at 25^oC and 1.013 bars, respectively. Wherever possible, real field measurements were used within the models, such as H_2S concentrations and pH values.

Geochemical reaction-path modeling can be conducted to assess the geochemical evolution of a solution and solid mineral phases in response to mass transfer (Bethke et al., 2008). In this study, several reaction path models were created using the GWB sub-program React to illustrate the geochemical effects of introducing saltwater into a freshwater system. The models simulate surface complexation processes through desorption of pre-existing ions and their replacement by adsorption of ions newly introduced with the saltwater (Lee & Saunders, 2003). The surface complexation model utilizes the double-layer, hydrous ferric oxide model developed by Dzombak and Morel (1990). A chemical analysis of Amazon River water (Hem, 1985; Bethke, 1996) was used to represent a typical freshwater chemistry (Table 1). Similarly, the chemistry of the saltwater reactant was defined based on a typical surface seawater (Drever, 1988; Bethke, 1996), shown in Table 2. In some cases, the formation of particular minerals (e.g., hematite, goethite, and magnetite) were suppressed; the formation of such minerals are kinetically favored on a long-term scale, but an amorphous hydrous ferric oxide is more likely to form within a short time frame.

Table 1. Basis for freshwater composition in reaction path models for this study, based on compositions of Amazon River water (Hem, 1985).

Freshwater		
$SiO_2(aq)$	7	mg/kg
Al^{3+}	0.07	mg/kg
Fe^{2+}	0.06	mg/kg
Ca^{2+}	4.3	mg/kg
Mg^{2+}	1.1	mg/kg
Na^{+}	1.8	mg/kg
$HCO3^{-}$	19	mg/kg
$SO4^{2-}$	3	mg/kg
Cl^{-}	1.9	mg/kg
$O_{2(aq)}$	5.8	mg/kg

Table 2. Basis for seawater composition in reaction path models for this study, based on analysis of typical seawater chemistry (Drever, 1988; Bethke, 1996).

Seawater		
$SiO_2(aq)$	6	mg/kg
Ca^{2+}	411	mg/kg
Mg^{2+}	1290	mg/kg
Na^{+}	10760	mg/kg
K^{+}	399	mg/kg
$HCO3^{-}$	142	mg/kg
$SO4^{2-}$	2710	mg/kg
Cl^{-}	19350	mg/kg

Trace Metals Analysis

Sediment cores from each site were sectioned into 3 cm segments. Each segment was centrifuged in 50 mL tubes to isolate pore water. Pore-water geochemical analyses were conducted using inductively coupled plasma mass spectrometry (ICP-MS) to determine the presence of trace metals and their concentrations. ICP-MS analysis was performed in Dr. Alison Keimowitz's lab at Vassar College.

Hydrocarbon Fingerprinting

Extraction of petroleum compounds from oiled sediments is based on EPA Method 3570 (Appendix 1). Solvents were extracted into 2 mL vials. The extracted oil samples were analyzed using an Agilent 5975C gas chromatograph-mass spectrometer (GC-MS) at ALS Environmental. Peak profiles of unique biomarkers output by the GC-MS were used to verify the potential correlation between the extracted oils and oil from the original source, Macondo-1. In the case of samples whose contamination sources were positively identified as the Macondo-1 well, the GC-MS results for those samples also were used to quantify the degree of contaminant degradation of heavy and light compounds over time.

After broader, more generalized results were obtained through full-scan GC-MS, a high-sensitivity run was conducted in GC-MS-Selected Ion Monitoring (SIM) mode. GC-MS-SIM focuses on specific hydrocarbon compounds with unique mass-to-charge ratios, providing data with much greater precision. The SIM results were used to identify specific petroleum biomarkers, including terpanes, hopanes, steranes, and polycyclic aromatic hydrocarbons (PAHs), highly weather-resistant compounds of crude oil. Biomarkers with a mass-to-charge ratio of 191 were examined in previous studies (Natter et al., 2012), so the main target for this study includes terpane and sterane compounds with mass-to-charge ratios of 171 and 181.

COREXIT 9500, the dispersant applied in response to the Deepwater Horizon spill, was characterized using gas and liquid chromatography-mass spectrometry (GC-MS and LC-MS) facilities in the Department of Chemistry and Biochemistry at Auburn University. The dispersant sample used in in the analysis was provided by the Florida Department of Environmental Protection (FDEP). Due to the nonvolatile nature of most dispersants (Plante et al., 2011), it was unclear whether COREXIT 9500 would produce more distinguishable peak profiles through liquid or gaseous form. Therefore, the sample was analyzed using both GC-MS and LC-MS. The resulting GC-MS and LC-MS chromatograms were analyzed to determine which produced characteristic peak profiles that would allow for more reliable source fingerprinting.

RESULTS & DISCUSSION

Hydrocarbon Fingerprinting

Fingerprinting of Oiled Sediments and Plants

Hydrocarbon fingerprinting techniques use gas chromatography-mass spectrometry (GC-MS) to correlate spilled oils with their initial source. Specific oil compounds with unique mass-to-charge ratios (m/z) can be analyzed by GC-MS operated in the Single Ion Monitoring (SIM) mode. Natter et al. (2012) used terpanes and hopanes (m/z 191) as geochemical biomarkers to trace the source, weathering, and biotransformation of oils in the coastal wetlands study areas. Biomarkers associated with steranes (m/z 217 and m/z 218) are targeted in this study for oil-to-oil correlations. Terpanes and steranes are derived from biological precursors of terpenoids and steroids, compounds that make great biomarkers due to their resistance to many degradation processes within natural environments.

Comparisons of m/z 217 and 218 f fragmentograms of initial BP crude oil to various weathered oil samples illustrate the effects of environmental weathering on the crude oil. In GC-MS analysis, lighter compounds elute earlier at lower temperatures, whereas heavier compounds have longer retention times. In full-scan GC-MS chromatographs and GC-MS-SIM fragmentograms (Figures 11-16), the initial BP crude sample exhibits a full spectrum of lighter and heavier compounds. By contrast, samples of weathered oil collected from plants, surface sediments, and sediments at depth, show a much stronger presence of heavier hydrocarbons relative to lighter hydrocarbons. The overall increased presence of heavier hydrocarbon compounds relative to lighter compounds occurs as a result of preferential biodegradation, evaporation, and photo-oxidation of lighter compounds (Wang and Stout, 2007). Although heavier compounds are concentrated relative to lighter compounds, it is important to note that the overall intensities of most compounds tend to be greatly reduced in weathered oils extracted from sediments. For example, GC-MS-SIM m/z 217 readings of the initial BP crude (Figure 12, top) peak at an intensity of 22,871, whereas a weathered crude oil sample collected from BJN sediment peaks at 1,729 (Figure 12, middle).

The m/z 217 fragmentogram of pure BP crude oil (Figure 11, top) displays a strong bimodal trend in the ranges of 17-19 minutes and 21-23 minutes. The intensity of these two modes is nearly at the same level. An additional smaller cluster of biomarkers centers around 16 minutes. Of all the weathered oils analyzed, oil scraped from plants at sites BJN and BJS (Figure 11) display the strongest correlation to the initial BP crude oil based on m/z 217 biomarkers. All three modes identified in the m/z fragmentogram of BP crude oil also appear in the weathered oil on plants at BJN and BJS. The first two modes (16 minutes; 17-19 minutes) are created from the elution of relatively lighter hydrocarbons than those that comprise the largest mode (21-23 minutes). Preferred weathering of lighter hydrocarbon compounds appears to have lowered the relative intensity of the first two modes compared to the enriched heavier hydrocarbons comprising the latest mode.

M/z 217 fragmentograms of surface sediments (0-3 cm) at BJN and BJS (Figure 12) also indicate a strong presence of BP crude. The fragmentograms of surficial oil at BJS and BJN contain the same three modes identified in the BP crude oil. In addition to these, oil at BJN displays an individual peak at 15.12 minutes and an extra mode in the range of 24-25 minutes. These additional peaks indicate the mixing of an external hydrocarbon source with BP crude oil at BJN.

M/z 217 fragmentograms of sediments at depths of 12-15 cm at BJS and BD (Figure 13) also show evidence of a separate hydrocarbon source, independent of the BP spill. Oil recovered from deeper sediments at BJS (Figure 13, middle) strongly displays the two clusters of peaks at 17-19 minutes and 21-23 minutes that indicate the presence of BP crude oil; the same fingerprint also reveals hydrocarbons in individual peaks at 15.12 minutes and in the range of 24-25 minutes.

Evidence of mixing BP crude with an additional hydrocarbon source is present in surface sediments at BJN and deeper sediments (12-15 cm) at BJS. Mixing is also evident in the deeper sediments of BD; however, the fingerprint at BD is dominated by a hydrocarbon source independent of the BP spill and appears to have mixed with only a small amount of BP crude oil. All fingerprints that display evidence of mixing contain the same hydrocarbon anomalies. The same peak at 15.12 minutes and cluster of peaks at 24-25 minutes appears in BJN surface sediment, deeper BJS sediments, and deeper BD sediments. The same anomalies in each fingerprint suggest that sites BJN, BJS, and BD have all experienced contamination by other hydrocarbon sources in addition to the BP crude oil. These additional hydrocarbons may be derived from other natural oil seeps in the Gulf of Mexico. The National Research Council (2003) reported that between 560,000 and 1,400,000 barrels of crude oil per year seep into the Gulf of Mexico from natural sources. The volume of oil released from these natural seeps is much less than that of the Deepwater Horizon spill.

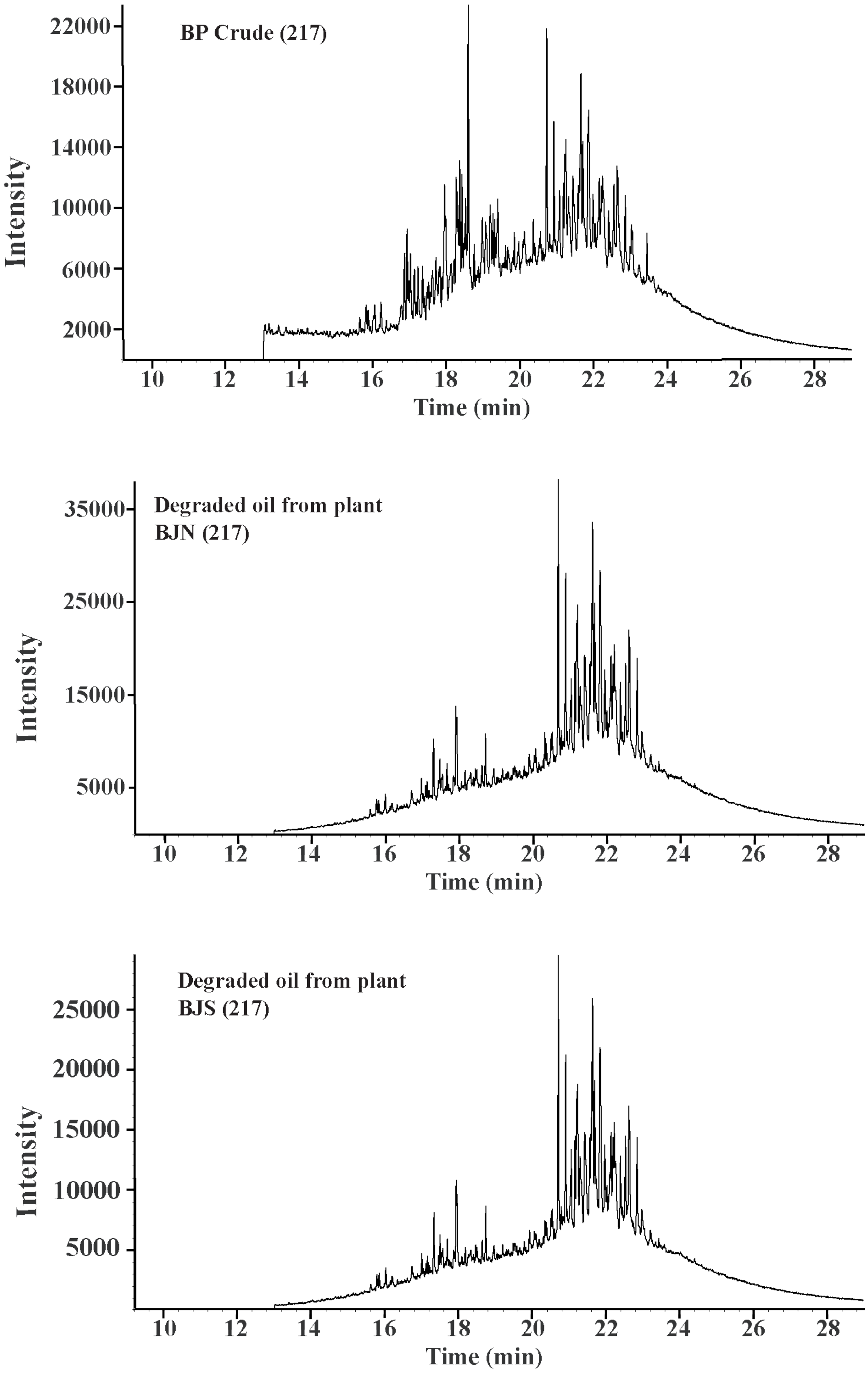

Figure 11. A GC-MS-SIM m/z 217 fragmentogram of pure MC-252 crude oil (top) in comparison to weathered oil scraped from suppressed plants at sites BJN (middle) and BJS (bottom).

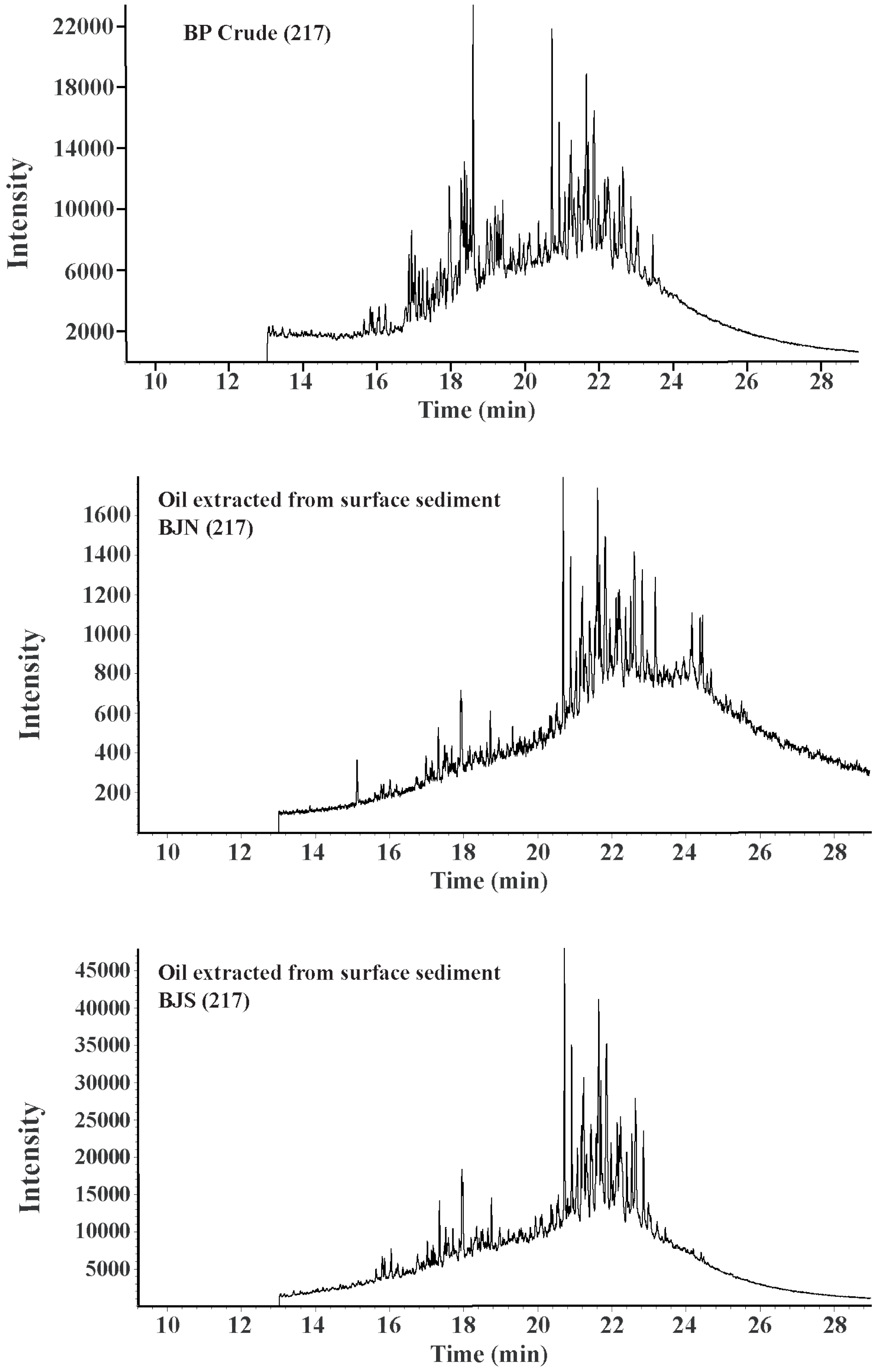

Figure 12. A GC-MS-SIM m/z 217 fragmentogram of pure MC-252 crude oil (top) in comparison to weathered oil recovered from surface sediments at sites BJN (middle) and BJS (bottom).

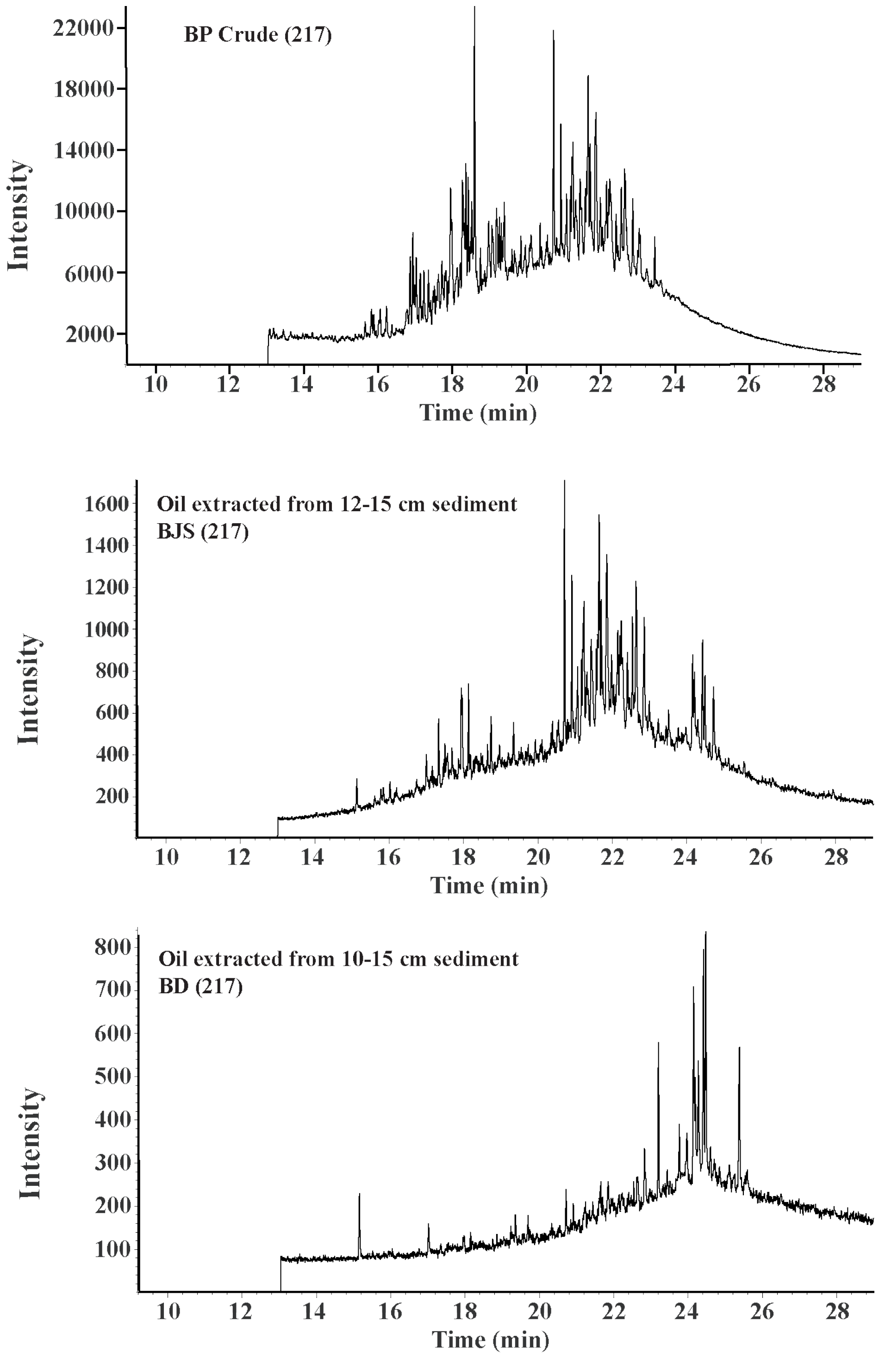

Figure 13. A GC-MS-SIM m/z 217 fragmentogram of pure MC-252 crude oil (top) in comparison to weathered oil recovered from sediments at a depth of 12-15cm at sites BJS (middle) and BD (bottom).

Hydrocarbon fingerprinting with GC-MS-SIM analysis of m/z 218 reveals very similar results to those of m/z 217. M/z 218 fragmentograms of pure BP crude oil display two larger modes in the ranges of 17-19 minutes and 21-23 minutes and a smaller mode centered on the 16-minute mark. Each of these modes is also evident in m/z 218 fragmentograms of oil scraped from plants at BJN and BJS (Figure 14). In addition to indicators of BP crude oil contamination, peaks at 18.72, 19.47, and 19.53 minutes (not seen in BP crude) suggest that these weathered oils were mixed with an additional hydrocarbon source.

M/z 218 fragmentograms of oil collected from surface sediments at BJN and BJS (Figure 15) strongly indicate the presence of BP crude oil. Fragmentograms of both BJN and BJS display the same three modes identified in initial BP crude oil. In addition to these, BJN contains compounds that elute at 18.72 minutes and in a cluster from 24-25 minutes. Although the presence of BP crude oil in these sediments is clear, it is also probable that some mixing has occurred with an additional source. M/z 218 fragmentograms of oil collected from deeper sediments (12-15 cm) at BJS and BD (Figure 16) provide further evidence to suggest that BP crude oil has infiltrated as deep as 15 cm. Oils in deeper BJS sediments contain the smaller mode (16 minutes) and two larger modes (17-19 and 21-23 minutes) that are reminiscent of initial BP crude oil; additional hydrocarbon compounds (at e.g. at 18.72 and 19.322 minutes) suggest moderate mixing with another source independent of the BP spill. By contrast, oils in deeper BD sediments show signs of slight mixing with BP crude but are dominated by a different hydrocarbon source.

Overall, m/z 217 and 218 fragmentograms provide strong indications of the presence of BP crude oil at saltmarsh sites around the Barataria Bay. The hydrocarbon fingerprints of BP crude exist in deeper sediments as well, indicating possible infiltration of oil into sediments as deep as 15 cm. The possible mechanisms of oil infiltration will be discussed in a later chapter.

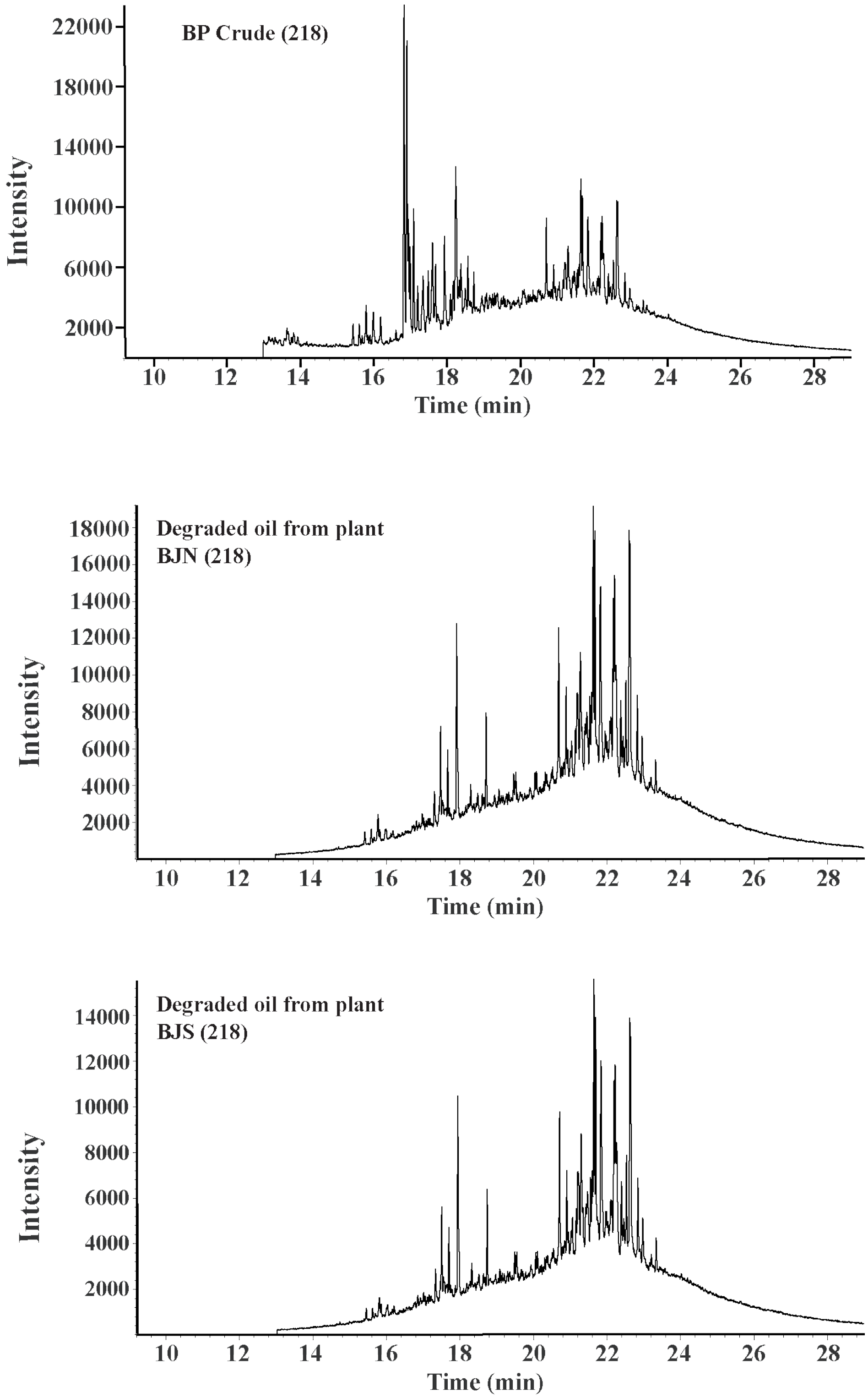

Figure 14. A GC-MS-SIM m/z 218 fragmentogram of initial MC-252 crude oil (top) in comparison to weathered oil scraped from suppressed plants at sites BJN (middle) and BJS (bottom).

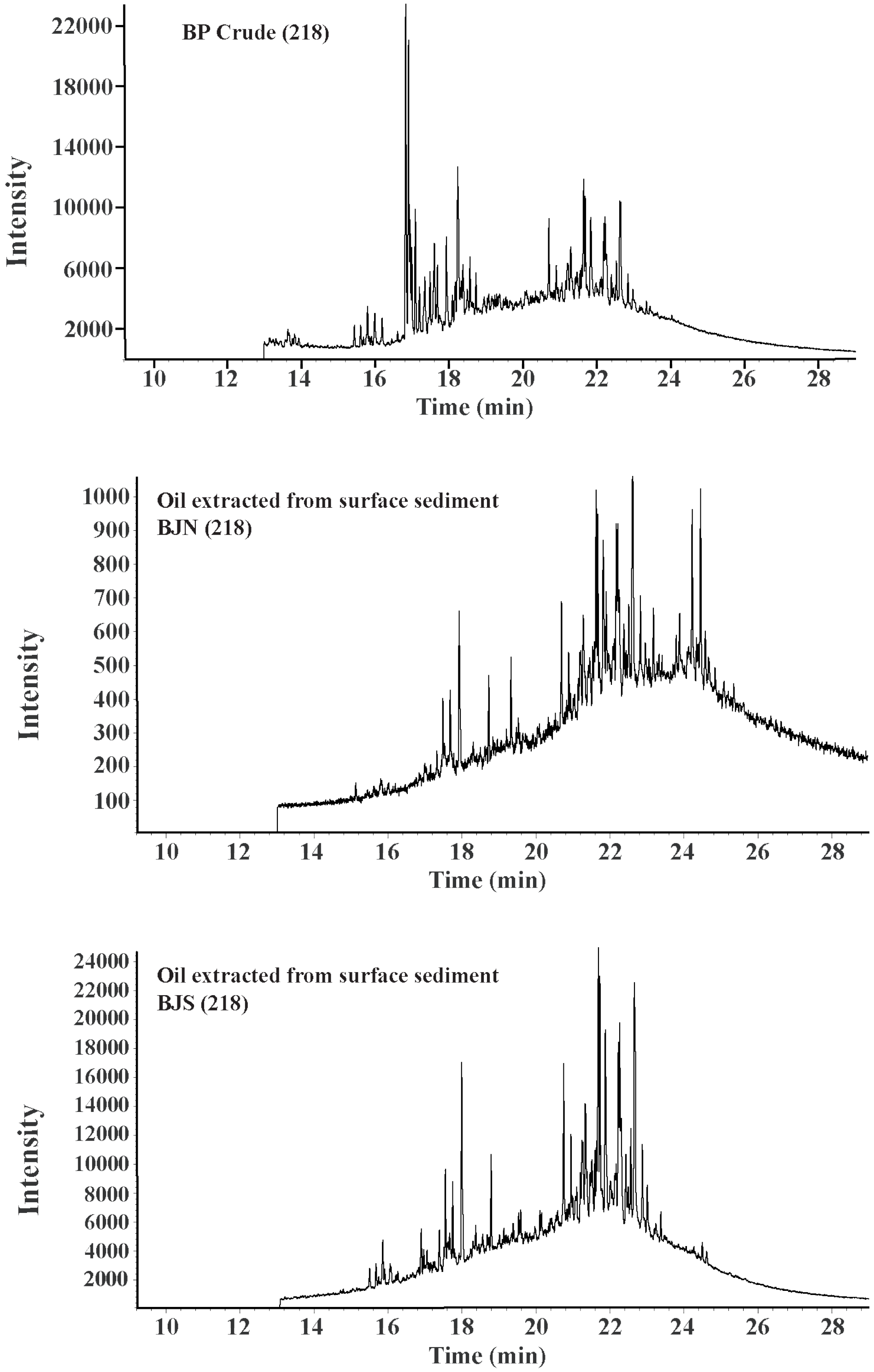

Figure 15. A GC-MS-SIM m/z 218 fragmentogram of initial MC-252 crude oil (top) in comparison to weathered oil recovered from surface sediments at sites BJN (middle) and BJS (bottom).

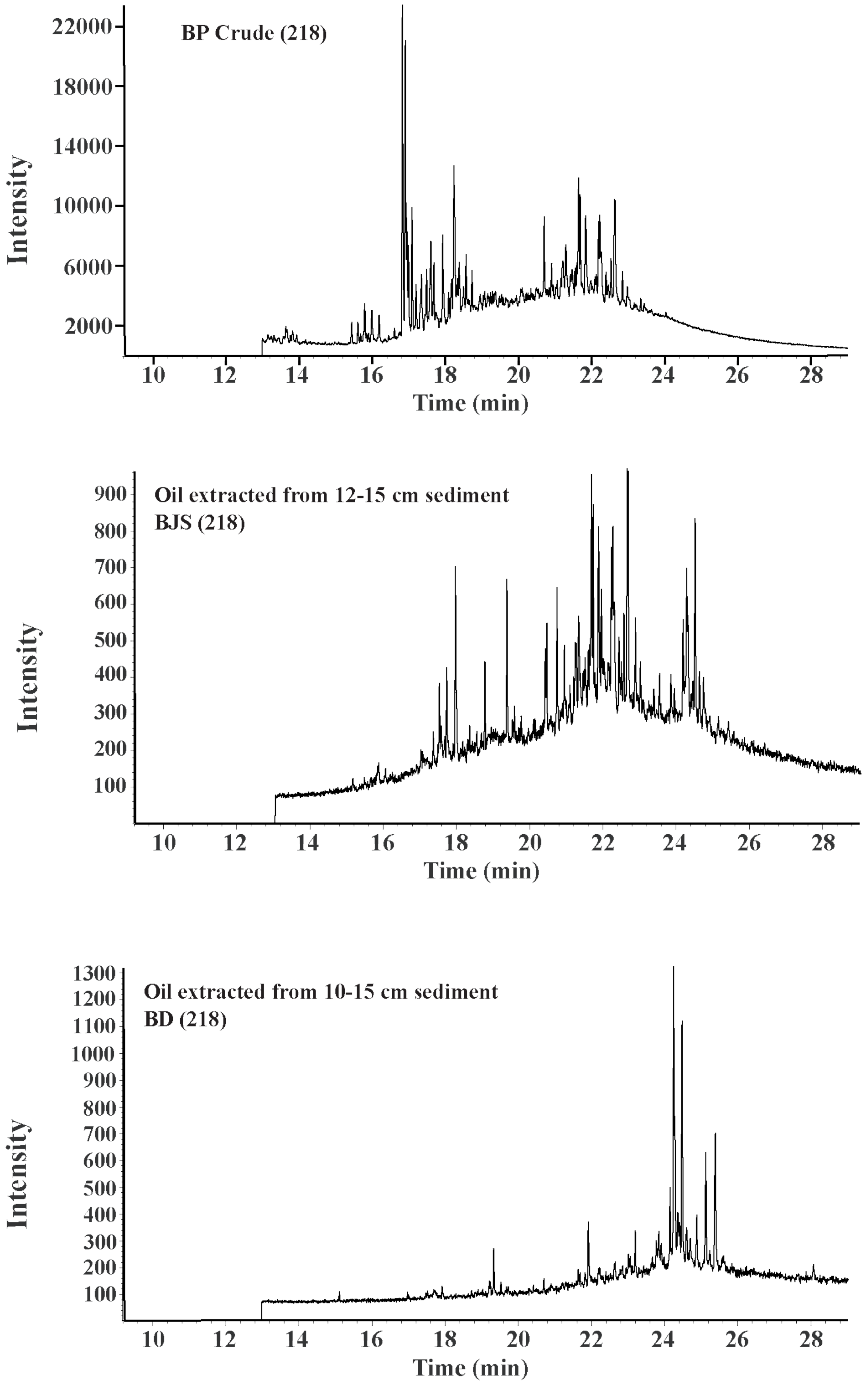

Figure 16. A GC-MS-SIM m/z 218 fragmentogram of initial MC-252 crude oil (top) in comparison to weathered oil recovered from sediments at a depth of 12-15cm at sites BJS (middle) and BD (bottom).

Fingerprinting of a Tarball

Tarballs were collected from the shore in Gulf State Park, Alabama in September of 2012, shortly after they were washed ashore by Hurricane Isaac. Hydrocarbon fingerprinting was conducted on the tarball via GC-MS and GC-MS-SIM, targeting m/z 191, 217, and 218. Gas chromatography of the tarball was conducted at a different ramp speed and final temperature than the chromatography conducted on BP and BJS oil samples scraped from plants; therefore, the retention times of BP and BJS compounds vary from those of the tarball.

Full-scan chromatographs (Figure 17) highlight the apparent enrichment of heavier hydrocarbon compounds in weathered oil and the tarball with respect to the BP crude oil due to the preferential degradation of lighter compounds. Positive identification of BP crude oil within the tarball is difficult in full-scan chromatographs due to differences in retention times. Spectral matching in GC-MS-SIM m/z 191 fragmentograms (Figure 18) provides some evidence for positive identification. Several compounds were recorded in the fingerprints of both BP crude oil and the tarball. The ratios of several biomarkers are summarized in Table 3. A higher similarity in selected biomarker ratios of BP crude oil to the tarball represents a greater likelihood that the tarball is descended from oils released from the MC-252 wellhead. For example, Ts/Tm (Ts/Tm =18α-22,29,30-trisnorneohopane/17α-22,29,30-trisnorhopane) ratios of the tar ball sample and initial BP oil occur in a remarkably narrow range (0.913-1.070). Strong correlations are also notable for C29/C30 norhopane-hopane (0.530-0.586), 35S/34S pentakishomohopane-tetrakishomohopane (0.792-0.814), and C31S/C30 homohopane-hopane (0.507-0.520) biomarkers. Based on the similarity of these calculated ratios, it is very probable that BP crude oil accounts for at least some of the hydrocarbons present in this tarball.

Fragmentograms of m/z 217 and 218 (Figures 19 and 20) both reveal fingerprints that are strongly bimodal. However, the smaller mode (centered on 16 minutes) present in m/z 217 and 218 fragmentograms of BP crude oil and weathered oil is barely detectable in the tarball. Nevertheless, the two, strong modes that appear in m/z 217 and 218 fragmentograms of the tarball match those in the BP crude oil and weathered oil, indicating that the persistent hydrocarbons associated with both modes were preserved fairly well.

In all chromatographs, the only distinguishable polycyclic aromatic hydrocarbon (PAH) present at a high intensity is C2-phenanthrenes/anthracenes (C2-P/A) (Figure 17, bottom). Specific biomarkers of terpanes, hopanes, and steranes thus represent a more powerful tool than PAHs to fingerprint the source of oils in natural environments. A complete list of all alkylated PAHs detected in the tarball can be found in Table 4. Several PAHs derived from crude oils are potent carcinogens (Daudel & Daudel, 1966), and the long-term effects of persistent PAH compounds in marsh ecosystems remains unclear.

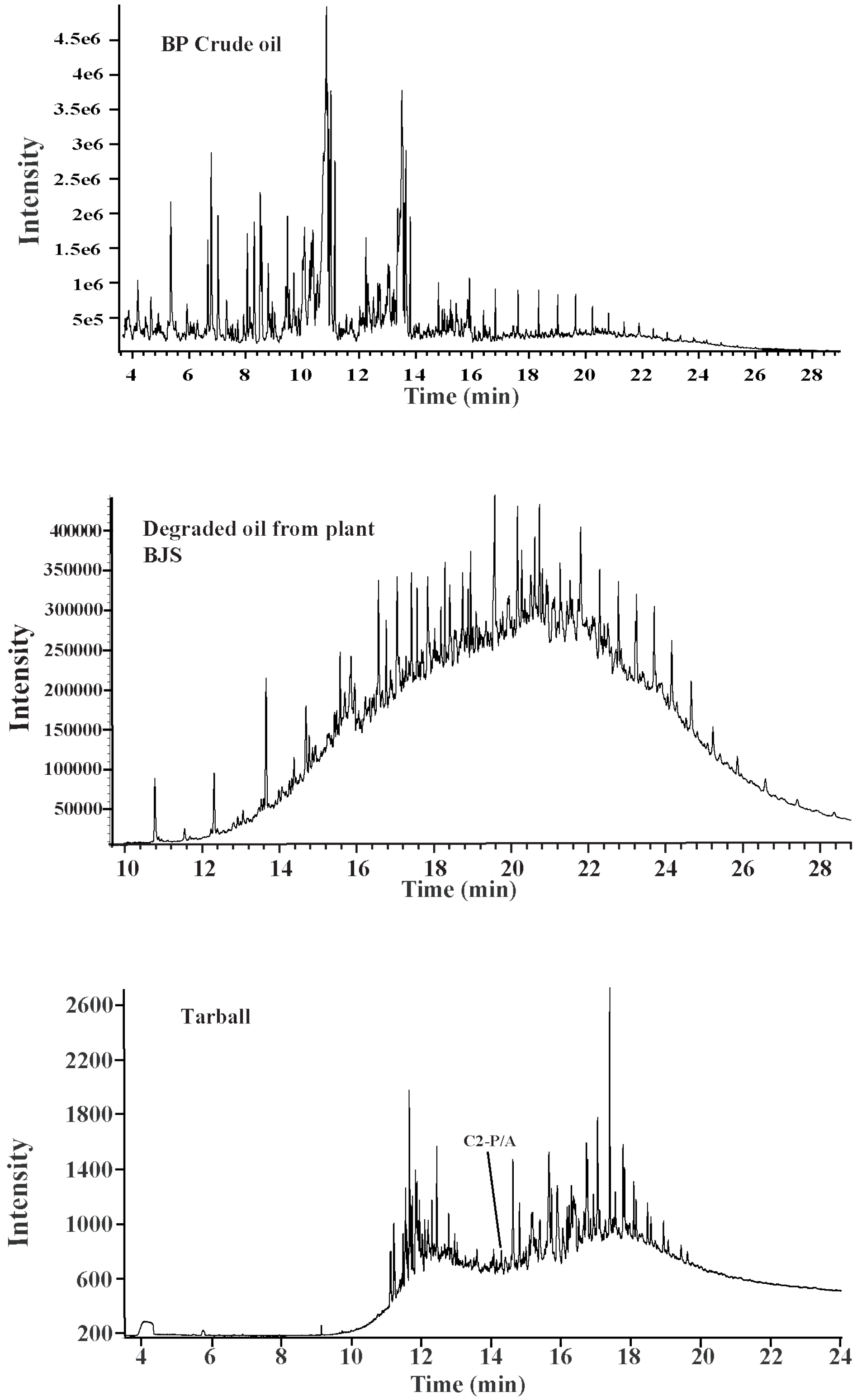

Figure 17. A full-scan GC-MS chromatograph of pure MC-252 crude oil (top; from Natter et al., 2012) in comparison to weathered oil scraped from suppressed plants at BJS (middle; from Keevan, 2012) and a tarball collected from the Gulf coast 2.5 years after the Deepwater Horizon spill (bottom).

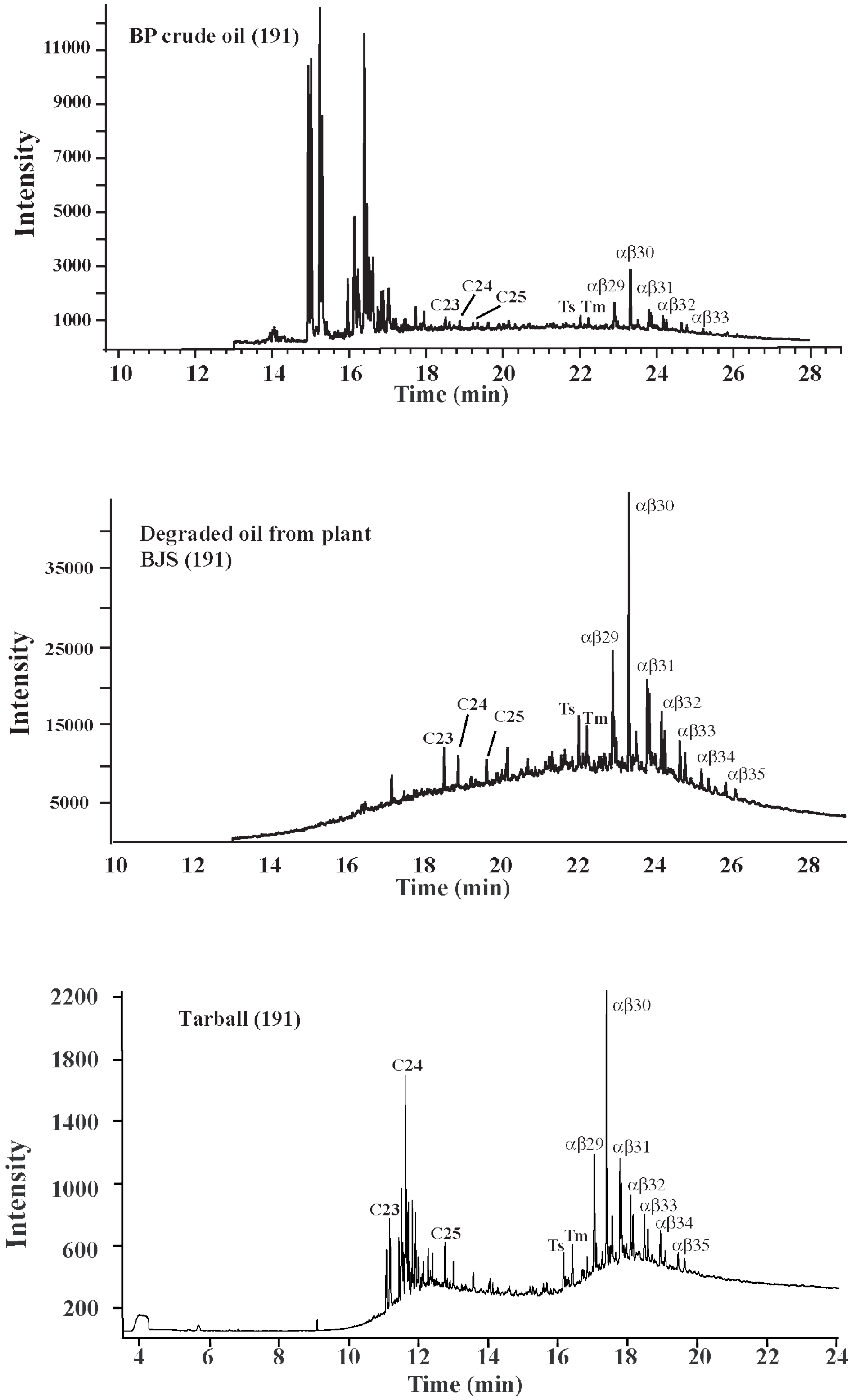

Figure 18. A GC-MS-SIM m/z 191 fragmentogram of pure MC-252 crude oil (top; from Natter et al., 2012) in comparison to weathered oil scraped from suppressed plants at BJS (middle; from Keevan, 2012) and a tarball collected from the Gulf coast 2.5 years after the Deepwater Horizon spill (bottom).

Table 3. Ratios of several biomarkers common to m/z 191 spectra. Closer ratios represent increased likelihood of matching hydrocarbon sources (ratios of BP crude oil, weathered oil/BJN, and surface sediment/BJN are reproduced from Natter et al., 2012).

Oil samples	**m/z 191**					
	Ts/Tm[1]	**24Tri/23Tri[2]**	**C29/C30[3]**	**29D/29H[4]**	**35S/34S[5]**	**C31S/C30[6]**
BP crude oil	1.070	0.914	0.586	0.564	0.814	0.507
Weathered oil/BJN	1.057	0.912	0.531	0.557	0.809	0.487
Surface sediment/BJN	0.965	1.001	0.592	-	-	-
Tarball	0.913	-	0.530	-	0.792	0.520

[1] Ts/Tm = 18α-22,29,30-trisnorneohopane / 17α-22,29,30-trisnorhopane

[2] 24Tri/23Tri = C24 tricyclic terpane / C23 tricyclic terpane

[3] C29/C30 = 17α,21β(H)-30-norhopane / 17α,21β(H)-hopane

[4] 29D/29H = 18α(H)-30-norneohopane / 17α,21β(H)-30-norhopane

[5] 35S/34S = 17α,21β(H)-20-pentakishomohopane (22S) / 17α,21β(H)-20-tetrakishomohopane (22S)

[6] C31S/C30 = 17α,21β(H)-20-homohopane (22S) / 17α,21β(H)-20-hopane (22S)

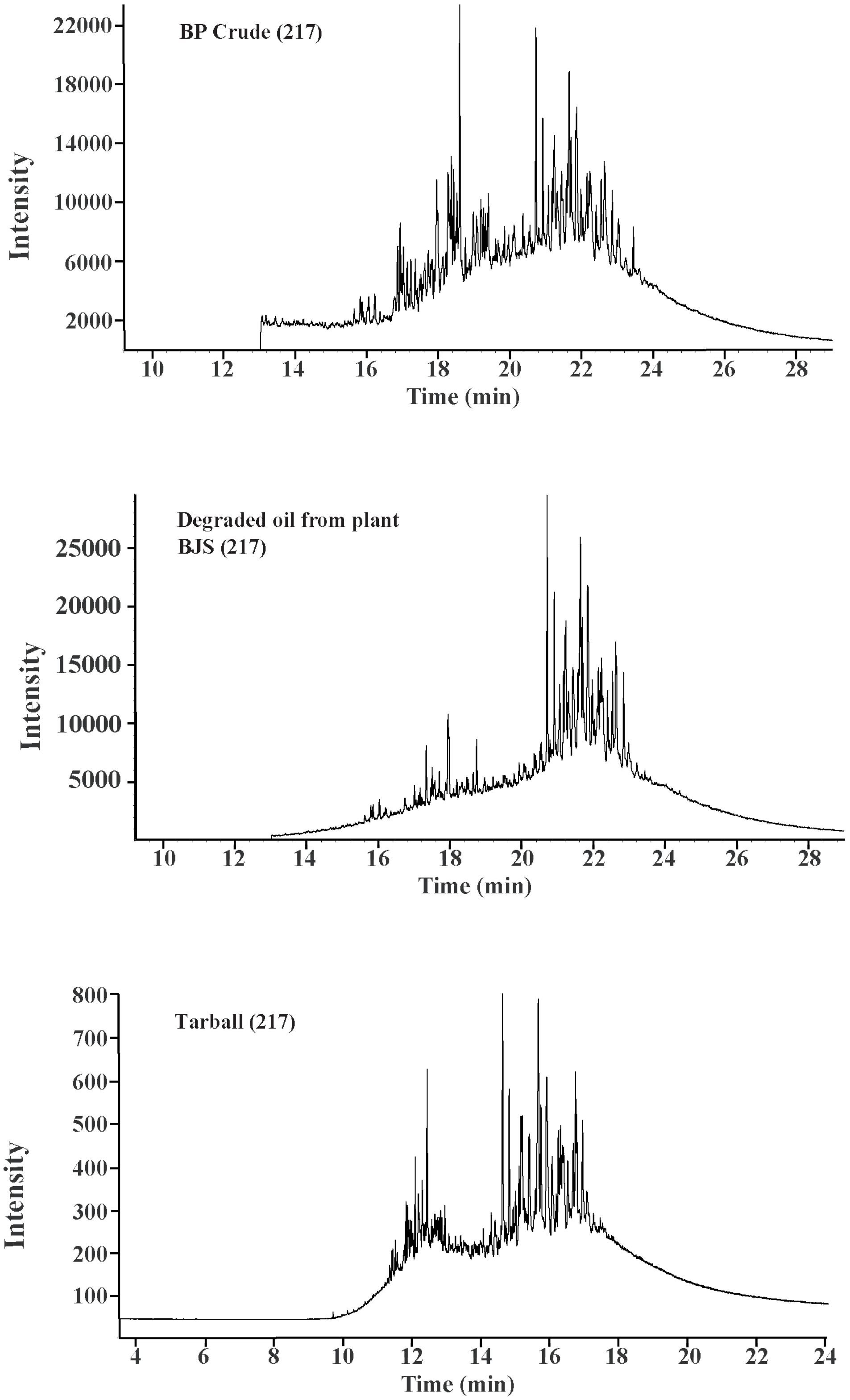

Figure 19. A GC-MS-SIM m/z 217 fragmentogram of pure MC-252 crude oil (top; from Natter et al., 2012) in comparison to weathered oil scraped from suppressed plants at BJS (middle; from Keevan, 2012) and a tarball collected from the Gulf coast 2.5 years after the Deepwater Horizon spill (bottom).

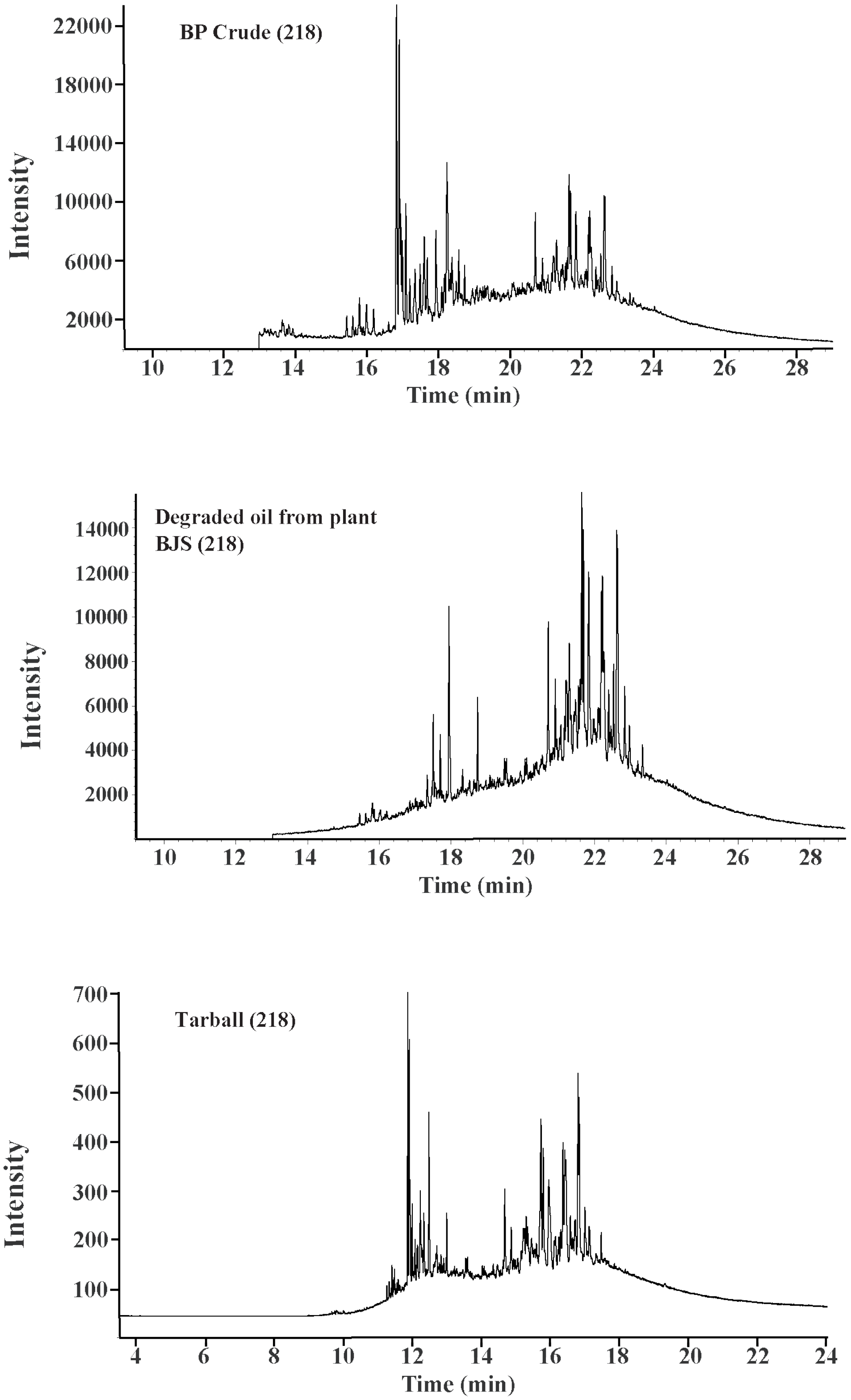

Figure 20. A GC-MS-SIM m/z 218 fragmentogram of pure MC-252 crude oil (top; from Natter et al., 2012) in comparison to weathered oil scraped from suppressed plants at BJS (middle; from Keevan, 2012) and a tarball collected from the Gulf coast 2.5 years after the Deepwater Horizon spill (bottom).

Table 4. Measurements of alkylated polycyclic aromatic hydrocarbons (PAHs) from a Gulf coast tarball (ND = not detected).

Alkylated PAH	Reading (mg/kg)
cis/trans-Decalin	0.190
C1-Decalins	0.336
C2-Decalins	0.443
C3-Decalins	0.635
C4-Decalins	0.812
Benzo(b)thiophene	ND
C1-Benzothiophenes	ND
C2-Benzothiophenes	ND
C3-Benzothiophenes	0.0198
C4-Benzothiophenes	ND
Naphthalene	0.281
C1-Naphthalenes	0.573
C2-Naphthalenes	0.592
C3-Naphthalenes	0.461
C4-Naphthalenes	1.11
Biphenyl	0.179
Dibenzofuran	0.0481
Acenaphthylene	0.0123
Acenaphthene	0.00801
Fluorene	0.116
C1-Fluorenes	0.570
C2-Fluorenes	5.00
C3-Fluorenes	9.93
Anthracene	0.120
Phenanthrene	0.294
C1-Phenanthrenes/Anthracenes	6.43
C2-Phenanthrenes/Anthracenes	26.3
C3-Phenanthrenes/Anthracenes	23.4
C4-Phenanthrenes/Anthracenes	16.1
Retene	1.71
Dibenzothiophene	0.150
C1-Dibenzothiophenes	1.67
C2-Dibenzothiophenes	9.02
C3-Dibenzothiophenes	9.84
C4-Dibenzothiophenes	9.61
Benzo(b)fluorene	0.392
Fluoranthene	0.232
Pyrene	0.606
C1-Fluoranthenes/Pyrenes	2.99
C2-Fluoranthenes/Pyrenes	4.11
C3-Fluoranthenes/Pyrenes	4.25
C4-Fluoranthenes/Pyrenes	5.10
Naphthobenzothiophene	2.01
C1-Naphthobenzothiophenes	8.65
C2-Naphthobenzothiophenes	9.34
C3-Naphthobenzothiophenes	6.62
C4-Naphthobenzothiophenes	2.95
Benz(a)anthracene	0.0603
Chrysene	6.77
C1-Chrysenes	12.0
C2-Chrysenes	10.5
C3-Chrysenes	4.99
C4-Chrysenes	3.09
Benzo(b)fluoranthene	0.726
Benzo(k)fluoranthene	ND
Benzo(a)fluoranthene	ND
Benzo(e)pyrene	1.09
C30-Hopane	16.3
Benzo(a)pyrene	0.0593
Perylene	0.0461
Indeno(1,2,3-cd)pyrene	ND
Dibenz(a,h)anthracene	0.175
Benzo(g,h,i)perylene	0.194
4-Methyldibenzothiophene	0.781
2-Methyldibenzothiophene	0.318
1-Methyldibenzothiophene	0.312
3-Methylphenanthrene	1.29
2-Methylphenanthrene	1.26
2-Methylanthracene	ND
9-Methylphenanthrene	1.90
1-Methylphenanthrene	1.41
2-Methylnaphthalene	0.578
1-Methylnaphthalene	0.266
2,6-Dimethylnaphthalene	0.381
2,3,5-Trimethylnaphthalene	0.143
Carbazole	ND

Dispersant Fingerprinting

A pure sample of COREXIT 9500A, the primary dispersant used in BP's remediation efforts for the Deepwater Horizon spill, was obtained for chemical analysis. Following the spill, dispersant was applied directly into the flowing wellhead and aerially to the surficial Gulf oil slick, but it is suspected that the dispersant may have migrated to coastal wetlands along with oil through the physical wave action of Gulf waters. This study aims to characterize the chemical nature of the dispersant so that future studies may determine the fate and geochemical evolution of COREXIT 9500A along Gulf coast saltmarshes. COREXIT 9500A can be characterized by its volatile compounds through gas chromatography-mass spectrometry (GC-MS) and its non-volatile ions through liquid chromatography-mass spectrometry (LC-MS). The chromatographs produced through GC-MS and LC-MS collectively serve to identify the potential compounds that may act as tracers in natural environments.

NALCO, the manufacturers of COREXIT, have reported some of the ingredients in COREXIT 9500 through Material Safety Data Sheets (MSDS). Hazardous substances revealed by the MSDS's include organic sulfonic acid salt, propylene glycol, and hydrotreated light petroleum products (NALCO). Several of these published compounds and others are revealed through GC-MS and LC-MS analyses of a pure COREXIT sample.

The most prominent compounds displayed in the GC-MS chromatograph (Figure 21) are polyethylene glycol and light hydrocarbon compounds. Polyethylene glycol is used in the dispersant as a surfactant. A surfactant induces emulsification by coating the surface of the crude oil and lowering the tension at the interface between the oil and surrounding water. Another compound that registered a high intensity was a branched hydrocarbon, $C_{15}H_{32}$ (Dodecane,2,6,10-trimethyl). The polyethylene glycol and hydrocarbon account for the surfactant and hydrocarbon-based solvent components discussed by Judson et al. (2010). These dominant components of COREXIT 9500A are light, as indicated by their quick elution (i.e. under 10 minutes). In Figure 21, the shaded red box outlines a region where the intensity has been scaled up by a factor of 36. At this level, another peak is evident; this exaggerated peak indicates the presence of a saturated 16C-hydrocarbon fatty acid chain and carboxyl group, $CH_3(CH_2)_{14}COOH$, or palmitic acid.

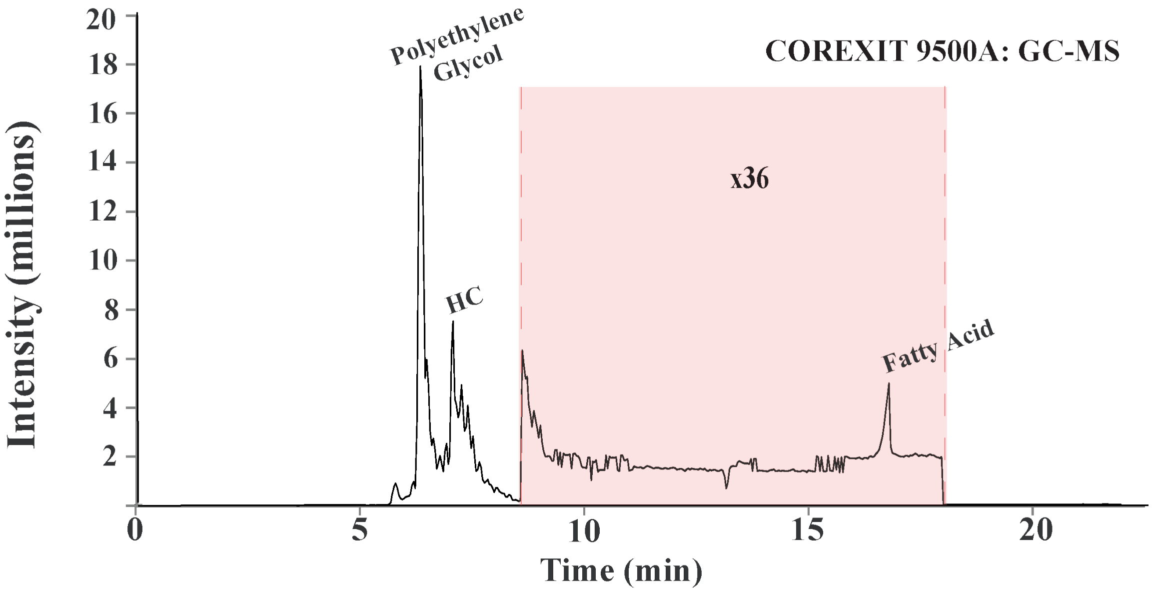

Figure 21. Chemical analysis of dispersant COREXIT 9500A via gas chromatography-mass spectrometry (GC-MS), indicating the presence of polyethylene glycol, light hydrocarbon compounds, and fatty acids.

Liquid chromatography of positive ions (Figure 22) from COREXIT 9500A revealed a single spike of high intensity and a trend of related peaks of lower intensity. The highest individual peak occurs at m/z 213.1471. Within the segment of 5x exaggeration, there is a clear trend of rising and falling m/z values that occur at regular intervals. This trend appears similar to the process of wax enrichment that occurs in many spilled oils (Wang and Stout, 2007). However, a key feature of this trend is the consistent spacing of 44 m/z between each peak. A regular spacing of 44 is highly indicative of polyethylene glycol (PEG). PEG is composed of repeating $(C_2OH_4)_n$ units, each of which have an atomic mass unit (amu) of 44. Although it appears unrelated, the high intensity peak at m/z 213.1471 falls along the repeating interval of 44 m/z. The peak at 213.1471 is likely created by a compound of organic sulfonic acid and PEG; a compound of sulfonic acid (SO_3H; 81 amu) and 3 PEG, $(C_2OH_4)_{3}$,;132 amu) amounts to a total mass of 213 amu. If this compound is a sulfonic acid, it may represent the base in a series of compounds that regularly increase by 44 amu with the presence of additional individual PEGs. PEGs adsorb onto the surface of oil to promote uniform distribution and eliminate the attractive forces that form thick slicks. Finally, one peak at 467.1990 does not fall within the regular PEG interval. This peak likely represents dioctyl sodium sulfosuccinate (DOSS), a neutral compound with an atomic mass of 444.56 amu ($C_{20}H_{37}NaO_7S$). Its presence in a liquid chromatograph indicates that the molecule has been ionized. The detected DOSS was likely ionized by an additional sodium (23 amu), resulting in the recorded m/z of 467.1990.

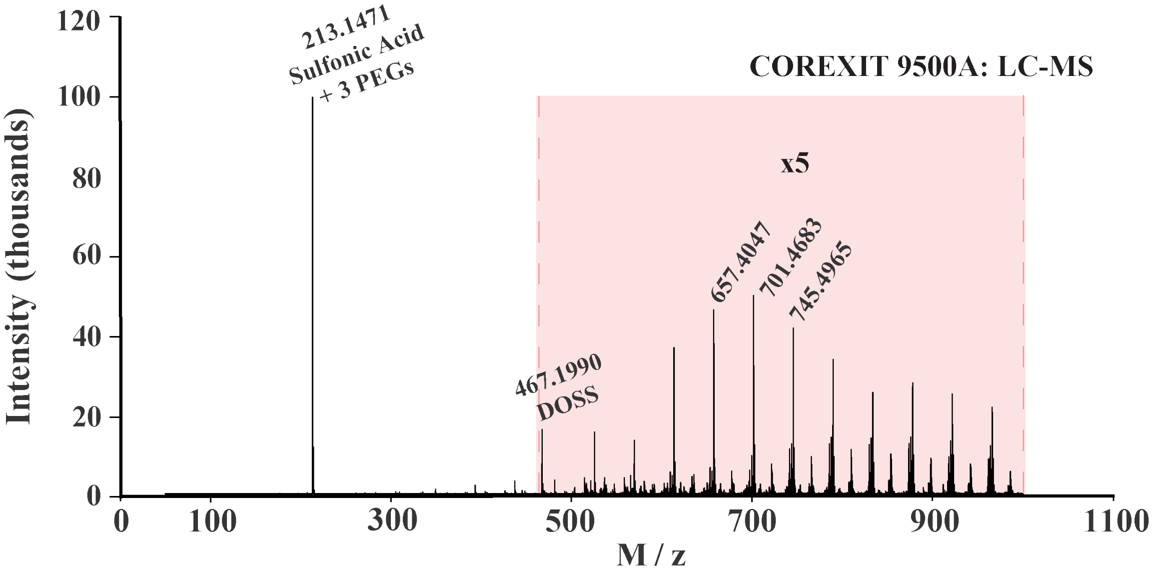

Figure 22. Chemical analysis of dispersant COREXIT 9500A via liquid chromatography-mass spectrometry (LC-MS) illustrating a polyethylene glycol (PEG) series, sulfonic acid base, and dioctyl sodium sulfosuccinate (DOSS).

Not all compounds identified can be used as reliable tracers for COREXIT 9500A in the natural environment. Some compounds identified here (i.e. organic sulfonic acid, etc.) biodegrade readily and therefore will not persist long enough in the natural environment to act as a biomarker. PEGs are resistant to thermal degradation when protected by water (Padfield et al., 1990), but studies have shown PEGs to be biodegradable by some bacteria (Obradors & Aguilar, 1991; Watson & Jones, 1977).

Other compounds may resist biodegradation, but it is difficult to trace their origin back to one particular source. Palmitic acid is one of the most common fatty acids found in animals, plants, and microorganisms. The palmitic acid identified in COREXIT 9500A also appears in the pore-water samples extracted from heavily-contaminated saltmarsh sites. However, it is likely that the palmitic acid in contaminated porewaters was derived from a local, biological source. Therefore, although palmitic acid is resistant to biodegradation, it cannot act as a reliable biomarker because its origin cannot be traced to one particular source. The same is true of the branched hydrocarbon revealed in GC-MS analysis.

Overall, DOSS likely provides the most reliable dispersant tracer. Kujawinski et al. (2012) reported that little to no DOSS had degraded in seawater four months after the initial application of COREXIT 9500A. It is also possible that DOSS may enter groundwater along coastal saltmarshes through anthropogenic means, as it is a common ingredient in some pesticides and suppositories. Therefore, a confident identification of COREXIT 9500A by DOSS will require a strong correlation between DOSS concentrations and the degree of oil spill contamination.

Trace Metals

In previous studies (Keevan, 2012; Natter, 2012), the bulk geochemical composition of saltmarsh sediments was determined through inductively coupled plasma-mass spectrometry (ICP-MS). The results for the geochemical analysis of sediments indicated high levels of metal contamination as a result of the influx of spilled oil from the Deepwater Horizon event. High concentrations of metals in sediments reflect the high capacity of fine-grained, saltmarsh sediments to sequester various elements (e.g. Ni, Cu, Pb, Zn, Sr, Co, V, Ba, Hg, As, S, and Fe) via adsorption or co-precipitation. This study quantifies the concentrations of dissolved sulfur and trace metals in pore waters at the same saltmarsh sites. Trace element analyses were conducted using the ICP facility at Vassar College.

Figures 23—25 display the concentrations of sulfur and various trace metals in the extracted pore waters from each site. A complete dataset, including removed outliers, can be found in Tables 5-8. For easy visual grouping, depth plots are color-coded by level of contamination: heavily contaminated sites are shown in shades of red, intermediate sites in shades of yellow, and pristine sites in shades of green. Box-and-whisker plots illustrate the ranges of metal concentrations and their correlations with degree of contamination.

Figure 23 (top) illustrates higher concentrations of total sulfur (representing all reduced and oxidized forms of H_2S, SO_4^{2-}, etc.) in pore water at heavily oiled sites. Unlike most other metals analyzed, sulfur concentrations were recorded on the scale of ppm in both sediment and pore water. Measurements of total sulfur concentrations have an average range of 249ppm at pristine sites, 261ppm at moderately contaminated sites, and 806ppm at heavily contaminated sites. Natter et al. (2012) also reported very high levels of reduced sulfur concentrations in pore waters (up to 80ppm) in heavily contaminated sediments. The influx of spilled oil probably provided new sulfur and additional substrate for sulfate-reducing bacteria that convert sulfate to sulfide.

Depth profiles of sulfur concentration in pore water and sediment are shown in Figure 26. Total sulfur concentrations in pore water are higher near the sediment surface than at depth. The same trend was observed in the populations of SRB estimated by Natter et al. (2012). Total sulfur concentrations near the sediment surface are higher at the heavily contaminated sites than the pristine sties, likely due to higher inflow of spilled oil on the top of marsh sediments.

Iron concentrations in pore water have an average range of 250ppb at pristine sites, 245ppb at moderately contaminated sites, and 221ppb at heavily contaminated sites (Figure 23, middle; Figure 27). Similarities in concentration ranges indicate no significant difference between oiled and pristine sites. Low dissolved iron and very high levels of sulfide indicate that bacterial sulfate reduction has fixed most reduced Fe by forming iron sulfide solids. Biogenic sulfide minerals such as pyrite with distinct framboidal form are found in oiled marsh sediments (Natter et al., 2012). Pyrite-like sulfide is the stable mineral phase formed under sulfate-reducing conditions enhanced by the massive inflow of oil and organic matter. The total concentrations of iron in sediments are slightly higher at oiled sites and Weeks Bay; the enrichment of trace metals in Weeks Bay is directly related to riverine input derived from industrial sources (Bonzongo and Lyons, 2004, Lee et al., 2013). Higher iron levels in sediments at contaminated sites can be interpreted as the result of pyrite precipitation (and thus Fe fixation) enacted by the reducing conditions of increased FeRB and SRB activity.

Ranges in arsenic concentrations in pore water (Figure 23, bottom) are highest at heavily contaminated sites. Measurements of arsenic concentrations have an average range of 15 ppb at pristine sites, 16 ppb at moderately contaminated sites, and 21 ppb at heavily contaminated sites. Heavily-contaminated sites BJN and BJS display the widest ranges in dissolved arsenic concentrations in pore water. Ranges in manganese follow the same trend; the average concentration range is 848ppb at pristine sites, 1132 ppb at moderately contaminated sites, and 3273 ppb at heavily contaminated sites.

Arsenic concentrations in sediments (Figure 28, right) are also notably higher at oiled sites than those at pristine sites. Due to chemical complexation among organic compounds and metals, crude oils often contain elevated levels (up to hundreds of mg/kg) of trace metals. Higher levels of arsenic and other metals in sediments are likely derived from spilled oil or industrial sources. Pyrite-like sulfides with distinct framboidal form are found in oiled sediments and Weeks Bay. Laser ablation inductively coupled plasma mass spectrometer (LA-ICP-MS) analyses show that sulfide solids contain various levels of trace metals such as As, Hg, Pb, Cu, Zn, V, and Zn (Keevan, 2012). These sulfide solids likely serve as local sinks for trace metals under sulfate-reducing conditions. The formation of pyrite and other sulfide solids explains the high levels (a few ppm) of arsenic in bulk sediments and the low concentrations of dissolved arsenic in pore-waters (< tens of ppb).

Chromium and copper are both common constituents of crude oil (Karchmer and Gunn, 1952; Ball et al., 1960) and therefore may be indicative of crude oil metals contamination. Ranges in copper (R = 0.011) follow no trend relative to the degree of contamination: the average Cu concentrations in pore water are 9.6 ppb at pristine sites, 10.2 ppb at moderately contaminated sites, and 7.7 ppb at heavily contaminated sites. However, chromium concentrations (Figure 24, bottom) display a more positive correlation with the degree of contamination; the average concentration range is 1.9 ppb at pristine sites, 2.2 ppb at moderately contaminated sites, and 4.9 ppb at heavily contaminated sites. Concentrations of copper at all depths are generally low (Figure 24, middle); every measurement is well below the maximum contamination level (MCL) for copper, 1.3 ppm. Spikes in copper (up to 27.4 ppb) occur around 10 cm depth at sites RG and WB; these spikes are very similar to those observed in iron at the same sites. In the case of both iron and copper, it is likely that these peaks are due to pre-spill anthropogenic factors. Spikes in chromium concentration also appear around a depth of 10 cm at the BJN site; the spikes in chromium occur only at heavily contaminated sites. Fluctuations in chromium may be a result of sequestration into minerals or organic matter. Chromium often displays a very low DTMP, but it commonly associates with silicate surfaces or organic matter (Alvarez-Iglesias, 2008). The highest concentration of chromium, 60.8 ppb, occurs at 3 cm depth at site BD (omitted from Figure 31 as an outlier). This especially high peak in chromium may be related to the influx of chromium along with oil contamination or other industrial sources, and the high intensity relative to other heavily contaminated sites may be a result of its enclosed setting and lack of tidal flushing.

Concentrations of Zn in pore water range from 21.0 to 472.3 ppb (Figure 25, bottom). Cobalt concentrations (R = 0.27471) were exceptionally low (0.0 to 5.3 ppb) (Figure 25, top).

Concentrations of Co in pore water at every sampling site and at nearly all depth intervals were measured as <1 ppb. There is no notable enrichment of Co and Zn in pore water at heavily oiled sites with respect to those at pristine sites.

In summary, concentrations of trace metals dissolved in pore waters are generally low (a few to hundreds of ppb), despite high levels of trace metals in bulk sediments (a few to tens of ppm). It is very likely that high organic matter content and bacterially-mediated sulfate reduction promote metal retention through the formation of sulfide solids. The bacterial sulfate reduction process can diminish the levels of trace metals dissolved in pore waters of marsh sediments. Several metals display strong trends with the degree of oil contamination. Concentrations of sulfur, arsenic, manganese, and chromium in pore waters all display a positive trend with increased degree of oil spill contamination. In sediments, concentrations of S, Fe, As, Mn, Cr, Cu, Ni, and Co also increase with increased oil contamination.

Table 5. ICP-MS results for sulfur (ppb) and iron (ppb) concentrations in subsurface pore waters down to 30 cm at various Gulf coastal saltmarsh sites.

SULFUR (ppb)

	BJN	BJS	BB	BD	RG	WB	LB	WI	BH	PACB
0-3cm	1146956.5	1230159.1	911652.1	1076081.5	709967.3	188691.5	572916.6		626024.5	
3-6cm	1059862.1	925973.8	670601.4	871791.0	609049.4	109944.6	473354.0	696901.5	640001.5	786562.9
6-9cm	816196.0	774351.9	427470.2	514679.9	347053.5	34010.4	283291.7	770637.5	611678.5	739367.3
9-12cm	675219.4	835025.4	298125.2	523254.1	308735.4	47977.3	143084.1	732816.4	620353.9	698267.1
12-15cm	483166.5	670030.0	195340.6	439583.2	222945.3	22275.9	235381.3	712992.1	628376.9	683693.6
15-18cm	405993.4	491512.4	127306.3	396979.4	314004.4	18502.9	426979.8		695990.2	627931.4
18-21cm	415367.8	428411.4	89617.3	333165.3	264795.0	19521.4			624570.0	648433.9
21-24cm	377503.9	523118.3	58000.7	415249.6	321780.3	48389.2			563799.0	564951.5
24-27cm	362073.5	467438.3	71464.7	518016.6	339552.1	65077.0			549146.5	645091.4
27-30cm	322506.3	591083.9	63154.8	408346.9		89086.1			583480.2	597392.2

IRON (ppb)

	BJN	BJS	BB	BD	RG	WB	LB	WI	BH	PACB
0-3cm	50.8	236.7	160.1	1212.4	46.1	107.9	100.2	73.0	64.5	
3-6cm	71.3	129.0	52.1	317.5	100.9	69.6	28.1	33.5	129.3	45.4
6-9cm	53.7	79.6	35.7	51.5	54.9	62.3	74.9	57.1	21.1	289.1
9-12cm	99.1	54.2	39.0	31.3	46.7	384.1	26.9	28.4	16.3	22.3
12-15cm	301.3	42.2	55.3	32.8	425.7	170.8	63.7	102.5	15.0	209.2
15-18cm	60.8	54.1	41.2	201.3	32.4	236.3	45.9	33.8	61.9	32.2
18-21cm	107.2	33.4	52.1	42.3	850.2	132.2	206.3		142.7	41.9
21-24cm	107.1	58.5	44.7	15.5	37.6	29.1	206.2		197.6	532.7
24-27cm	112.8	99.8	46.3	31.0	71.6	43.3	117.0		188.8	47.8
27-30cm	45.7	45.4	39.5	25.9		38.4	95.6		231.4	94.8

Table 6. ICP-MS results for arsenic (ppb) and manganese (ppb) concentrations in subsurface pore waters down to 30 cm at various Gulf coastal saltmarsh sites.

ARSENIC (ppb)

	BJN	BJS	BB	BD	RG	WB	LB	WI	BH	PACB
0-3cm	6.7	12.1	10.4	11.8	4.6	25.8	2.9	6.1	2.4	
3-6cm	6.7	18.6	9.5	27.4	5.5	9.6	3.4	4.7	3.1	12.1
6-9cm	8.3	24.7	8.2	8.5	4.1	3.1	4.5	5.3	2.0	5.5
9-12cm	11.2	33.2	7.4	6.0	7.2	8.5	9.9	7.1	1.5	3.5
12-15cm	13.5	25.3	8.2	6.4	10.0	6.0	5.3	29.4	1.4	4.5
15-18cm	15.9	40.2	8.2	9.0	6.7	8.0	13.0	6.4	1.1	2.8
18-21cm	19.9	41.0	10.9	7.1	16.9	4.9	1.3		1.9	4.7
21-24cm	24.7	43.7	7.1	7.6	6.6	5.0	2.4		3.0	4.5
24-27cm	30.1	36.9	8.3	6.6	4.4	5.3	2.1		2.9	4.2
27-30cm	32.1	29.8	7.0	5.8		6.3	1.3		11.9	3.0

MANGANESE (ppb)

	BJN	BJS	BB	BD	RG	WB	LB	WI	BH	PACB
0-3cm	429.7	964.1	5308.6	7353.1	4245.4	2984.9	524.0	23.9	543.4	
3-6cm	1153.1	2068.5	2422.4	1459.2	4571.5	2244.2	216.9	27.0	221.1	974.6
6-9cm	1395.3	2332.2	1915.7	921.0	3085.7	1346.7	179.5	20.0	217.9	640.6
9-12cm	1368.8	2652.7	1989.0	896.7	3029.1	1441.0	147.7	18.1	223.7	540.0
12-15cm	1285.1	2522.2	1998.3	838.3	1966.4	1619.5	141.6	33.0	215.7	530.1
15-18cm	1320.0	2007.4	1769.9	774.5	2775.2	1534.3	95.9	36.5	213.8	444.7
18-21cm	1362.7	2166.9	1979.7	807.9	2246.3	1405.6	23.3		241.1	467.8
21-24cm	1278.9	2274.2	1980.7	992.8	1844.1	1308.4	21.2		312.8	482.6
24-27cm	1574.1	2222.9	2200.3	1093.5	1723.6	1314.1	32.1		303.2	463.1
27-30cm	1717.1	2395.2	2337.0	809.2		1274.8	75.3		290.0	454.7

Table 7. ICP-MS results for copper (ppb) and chromium (ppb) concentrations in subsurface pore waters down to 30 cm at various Gulf coastal saltmarsh sites.

COPPER (ppb)

	BJN	BJS	BB	BD	RG	WB	LB	WI	BH	PACB
0-3cm	3.6	3.7	1.6	3.1	2.1	4.6	5.1	4.2	3.5	
3-6cm	3.6	4.0	2.1	11.3	1.1	4.6	2.8	4.7	3.2	2.9
6-9cm	6.8	3.8	2.2	4.2	1.1	5.1	4.2	3.2	2.6	2.2
9-12cm	3.0	4.9	2.4	4.3	27.4	22.2	4.7	2.2	5.3	2.2
12-15cm	2.3	4.8	5.1	2.5	9.2	3.6	4.1	3.2	2.3	3.0
15-18cm	3.7	5.5	2.3	6.8	3.6	4.2	5.0	3.9	2.8	1.8
18-21cm	15.7	5.6	6.3	3.5	15.5	8.9	7.1		3.5	3.5
21-24cm	3.8	4.7	1.9	2.9	3.4	3.9	9.4		4.7	3.5
24-27cm	2.7	6.2	3.3	1.5	3.2	4.1	6.3		3.9	3.5
27-30cm	5.3	4.9	2.6	1.2		3.3	8.7		5.7	3.3

CHROMIUM (ppb)

	BJN	BJS	BB	BD	RG	WB	LB	WI	BH	PACB
0-3cm	4.4	4.6	3.2	9.0	1.2	1.1	1.6	1.2	1.6	
3-6cm	4.4	4.4	2.9	60.8	1.2	2.1	2.7	1.4	1.6	1.2
6-9cm	4.5	3.9	2.9	7.7	1.0	2.8	1.5	1.4	1.1	1.6
9-12cm	11.0	7.5	2.9	3.5	4.9	126.4	1.2	1.1	1.1	1.0
12-15cm	4.4	3.9	3.3	4.3	65.6	1.5	1.2	1.5	1.1	1.9
15-18cm	3.9	3.8	3.0	4.2	4.0	1.8	1.1	1.3	1.4	1.0
18-21cm	4.3	4.5	4.3	3.9	141.2	20.6	1.1		1.7	1.3
21-24cm	4.2	4.6	2.9	3.1	3.6	2.0	0.8		3.0	3.3
24-27cm	4.6	6.2	3.4	2.4	2.6	1.1	1.5		1.6	1.7
27-30cm	4.2	3.9	3.5	1.7		0.8	1.4		1.9	1.4

Table 8. ICP-MS results for cobalt (ppb) and zinc (ppb) concentrations in subsurface pore waters down to 30 cm at various Gulf coastal saltmarsh sites.

COBALT (ppb)

	BJN	BJS	BB	BD	RG	WB	LB	WI	BH	PACB
0-3cm	0.2	0.4	0.5	3.8	0.7	0.4	0.2	0.2	0.1	
3-6cm	0.3	0.5	0.2	5.3	1.0	2.9	0.2	0.5	0.1	0.2
6-9cm	0.3	0.3	0.3	1.0	0.4	0.7	0.4	0.2	0.0	0.2
9-12cm	0.1	0.7	0.3	0.3	0.6	2.7	0.3	0.3	0.1	0.2
12-15cm	0.7	0.4	0.3	0.4	7.8	0.4	0.2	0.3	0.0	0.2
15-18cm	0.3	0.5	0.4	0.5	0.4	0.4	0.1	0.1	0.1	0.1
18-21cm	0.2	0.6	0.5	0.4	15.7	1.6	0.6		0.1	0.2
21-24cm	0.4	0.5	0.7	0.3	0.4	0.4	0.9		0.2	0.2
24-27cm	0.3	0.8	0.6	0.5	0.3	0.4	0.5		0.1	0.2
27-30cm	0.4	0.4	0.6	0.3		0.3	0.3		0.2	0.1

ZINC (ppb)

	BJN	BJS	BB	BD	RG	WB	LB	WI	BH	PACB
0-3cm	21.6	123.4	45.8	98.5	21.0	144.2	110.4	131.0	122.2	
3-6cm	42.5	77.7	52.9	100.0	31.1	105.9	112.1	98.1	87.9	90.1
6-9cm	177.1	70.7	32.9	95.0	51.6	101.4	136.6	95.6	96.8	94.2
9-12cm	30.6	107.7	84.3	103.0	388.7	118.9	123.0	83.9	87.2	78.9
12-15cm	31.5	102.0	69.7	91.5	11693.5	89.2	101.4	121.2	81.8	97.7
15-18cm	60.2	161.2	39.4	99.7	388.6	114.1	99.6	113.6	82.2	96.3
18-21cm	47.7	1065.2	47.9	779.9	21593.8	99.3	133.8		77.5	170.4
21-24cm	48.2	111.3	50.4	51.2	472.3	116.2	186.7		98.0	139.5
24-27cm	63.7	148.5	98.6	49.9	222.0	101.4	134.4		101.6	179.4
27-30cm	177.4	166.1	101.5	97.7		96.1	104.6		136.3	130.1

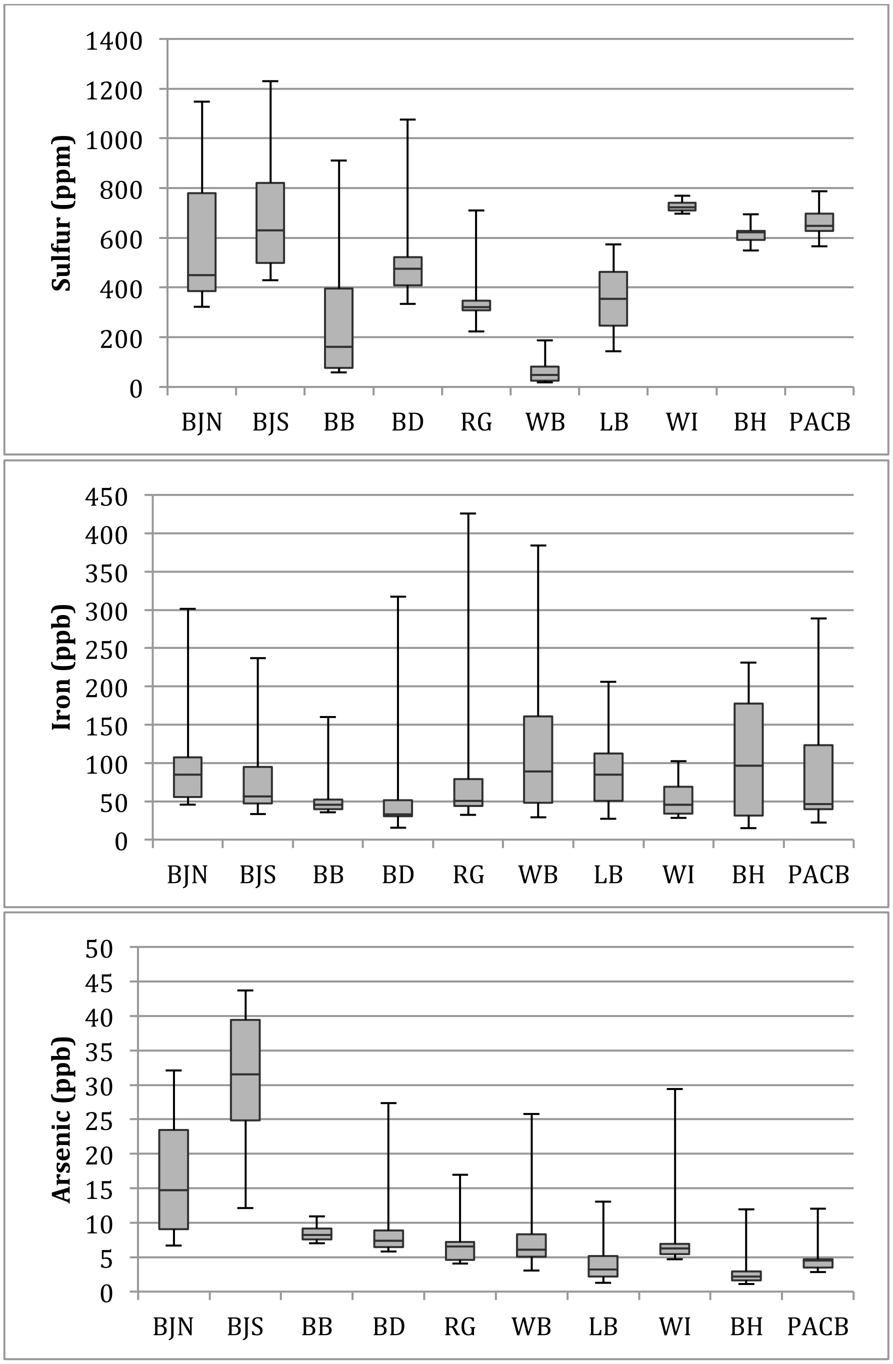

Figure 23. Box and whisker plots illustrating the ranges in concentrations of sulfur, iron, and arsenic at all sampling sites. Plots of sulfur and arsenic both display trends of increased concentration ranges with an increase in the degree of oil contamination.
[Heavily contaminated=BJN, BJS, BB, BD; moderately contaminated=RG, WI, PACB; pristine=LB, WB, BH.]

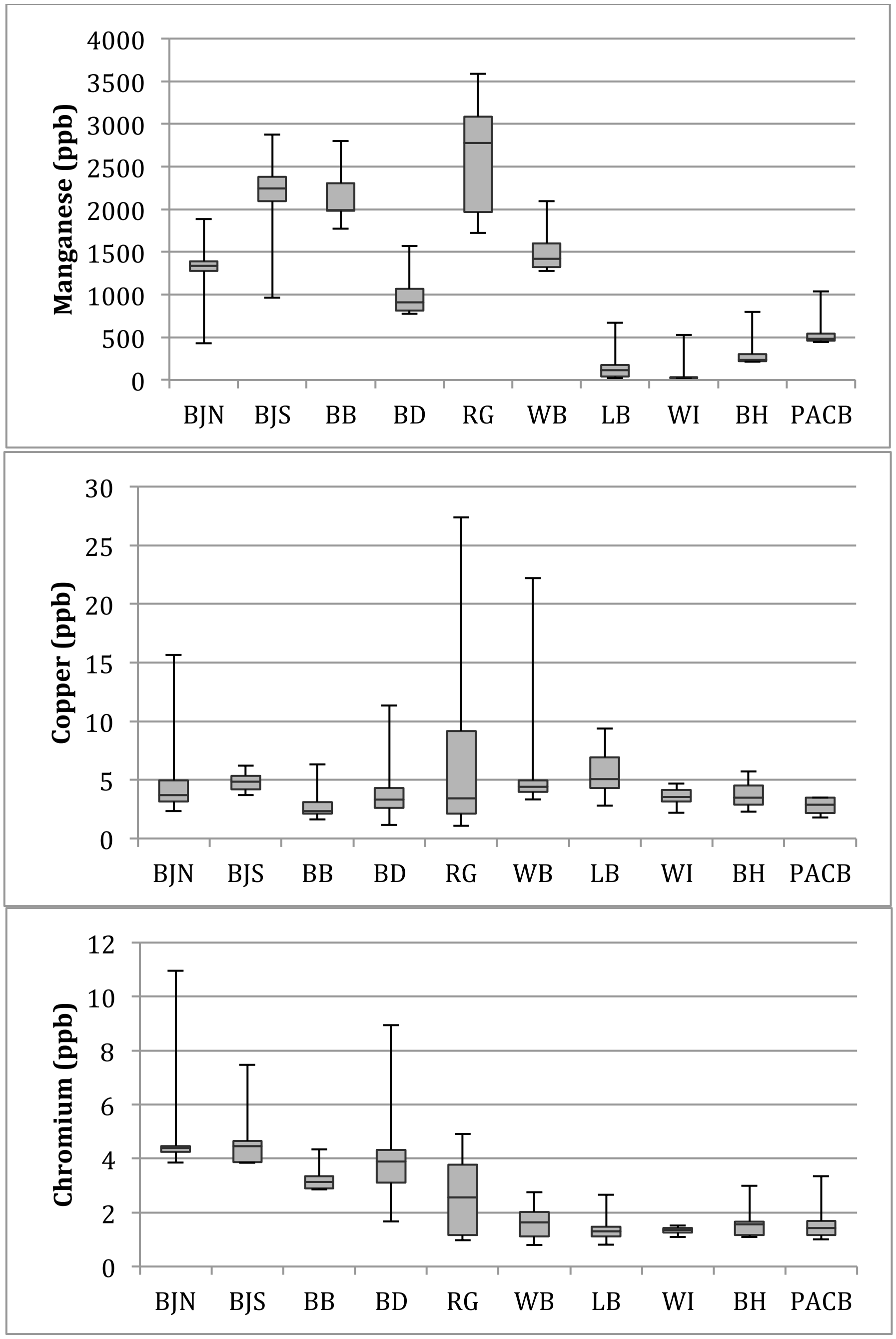

Figure 24. Box and whisker plots illustrating the ranges in concentrations of manganese, copper, and chromium at all sampling sites. Plots of manganese and chromium both display trends of increased concentration ranges with an increase in the degree of oil contamination.
[Heavily contaminated=BJN, BJS, BB, BD; moderately contaminated=RG, WI, PACB; pristine=LB, WB, BH.]

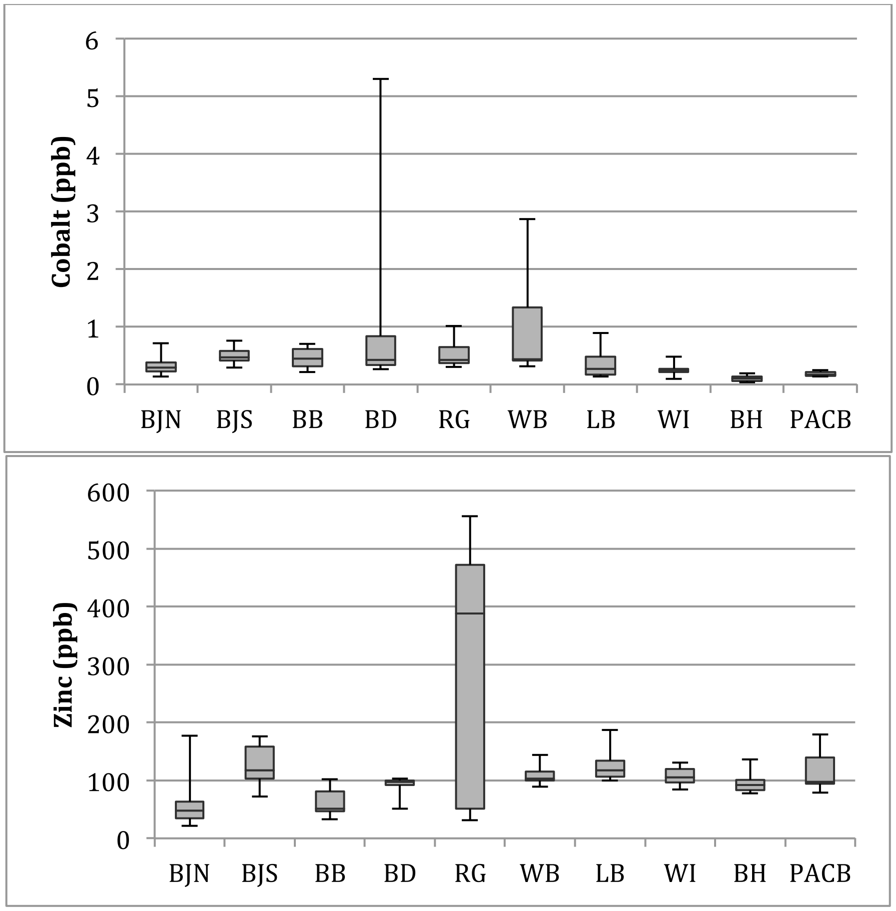

Figure 25. Box and whisker plots illustrating the ranges in concentrations of cobalt and zinc at all sampling sites. Neither cobalt nor zinc displays any strong trends with the degree of oil contamination.
[Heavily contaminated=BJN, BJS, BB, BD; moderately contaminated=RG, WI, PACB; pristine=LB, WB, BH.]

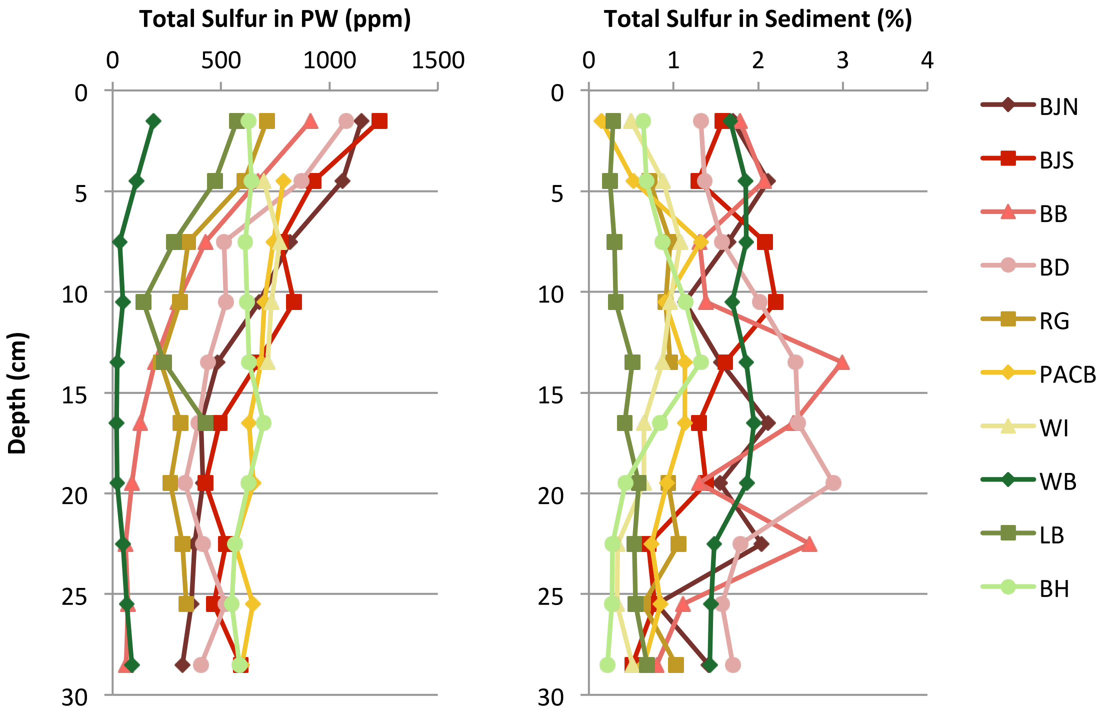

Figure 26. Plot of sulfur concentrations with depth as measured in pore waters (left) and sediments (right; after Keevan, 2012 and Natter; 2012). In pore waters, sulfur displays a strong trend of decreasing concentration with increasing depth; this profile matches that of sulfate-reducing bacteria (SRB) with similar decreasing trends with depth.

[Heavily contaminated sites colored in shades of red; moderately contaminated in yellow; pristine in green.]

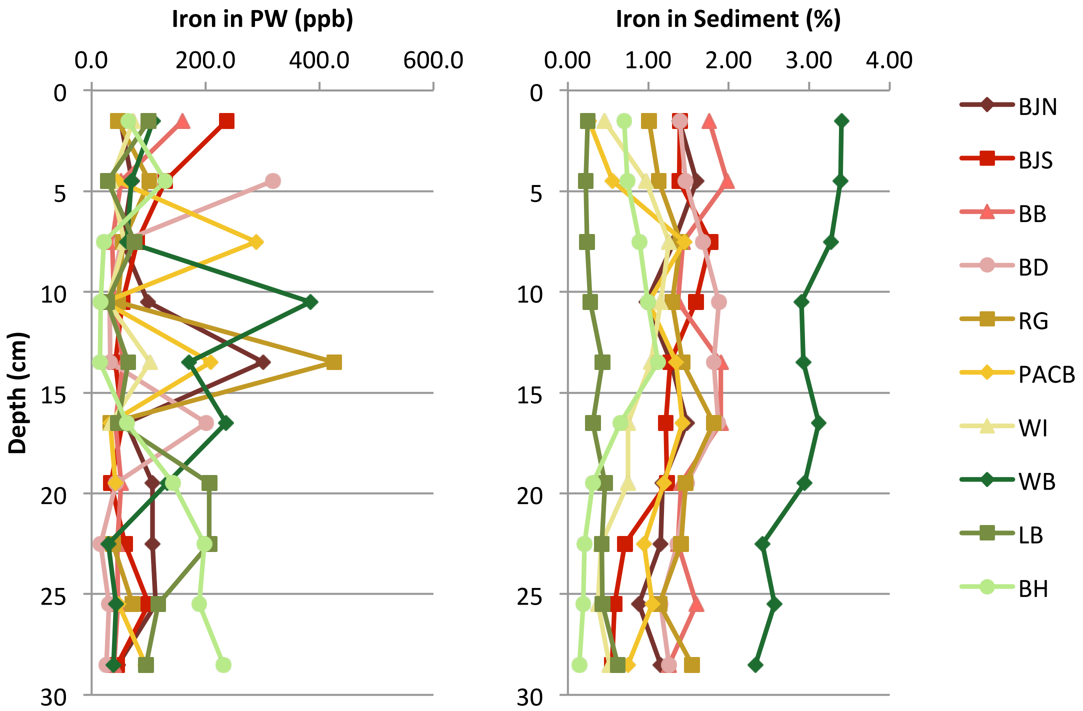

Figure 27. Plot of iron concentrations with depth as measured in pore waters (left) and sediments (right; after Keevan, 2012 and Natter; 2012). The strongest trend occurs in the sediment profile, where iron concentrations display a correlation with degree of oil contamination.
[Heavily contaminated sites colored in shades of red; moderately contaminated in yellow; pristine in green.]

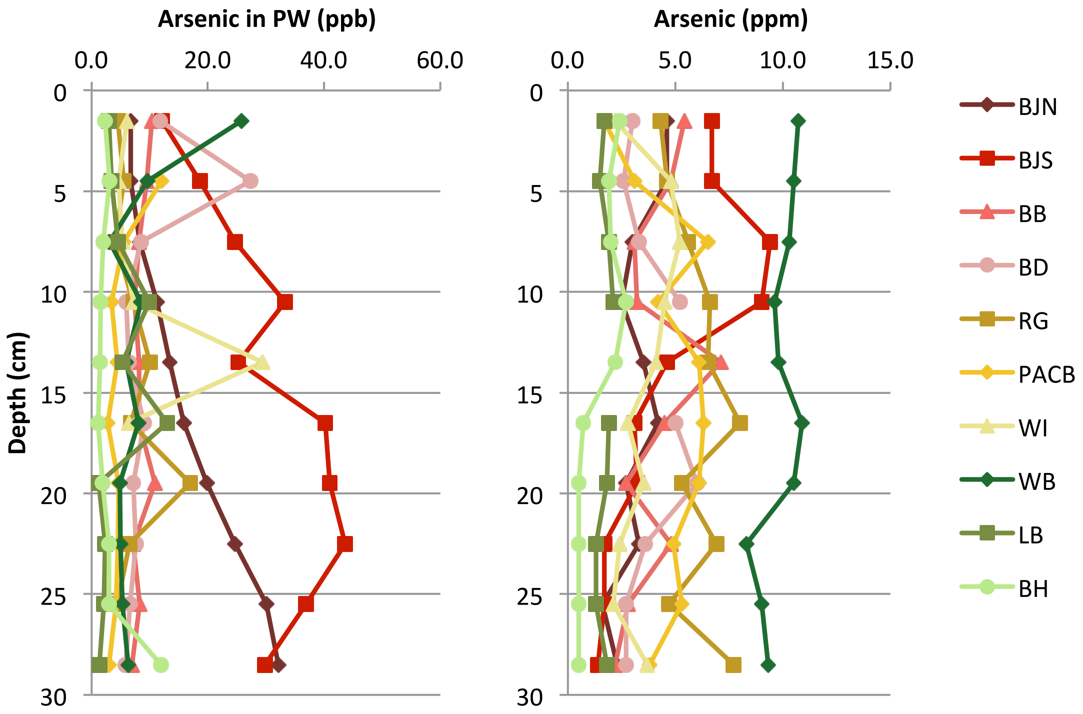

Figure 28. Plot of arsenic concentrations with depth as measured in pore waters (left) and sediments (right; after Keevan, 2012 and Natter; 2012). In pore waters, arsenic concentrations have highest ranges at sites BJN and BJS; at these sites, pore-water arsenic concentrations generally increase with depth.

[Heavily contaminated sites colored in shades of red; moderately contaminated in yellow; pristine in green.]

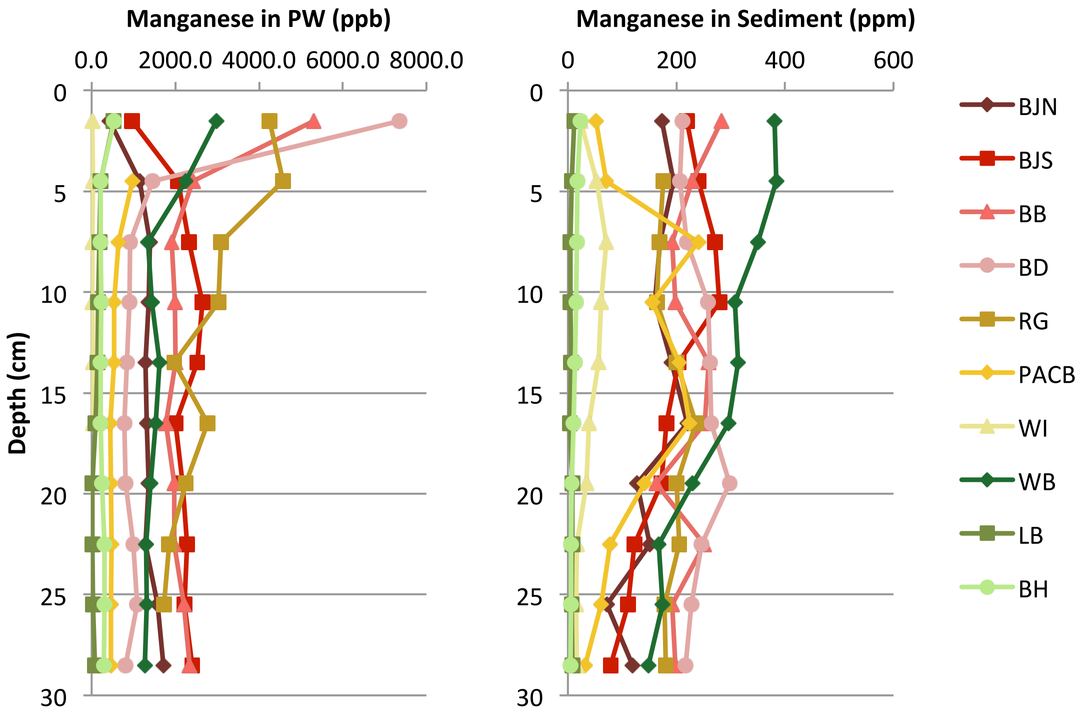

Figure 29. Plot of manganese concentrations with depth as measured in pore waters (left) and sediments (right; after Keevan, 2012 and Natter; 2012). Surficial concentrations at heavily-contaminated sites BB and BD are higher than at heavily-contaminated sites BJN and BJS, which may illustrate the effects of tidal flushing.

[Heavily contaminated sites colored in shades of red; moderately contaminated in yellow; pristine in green.]

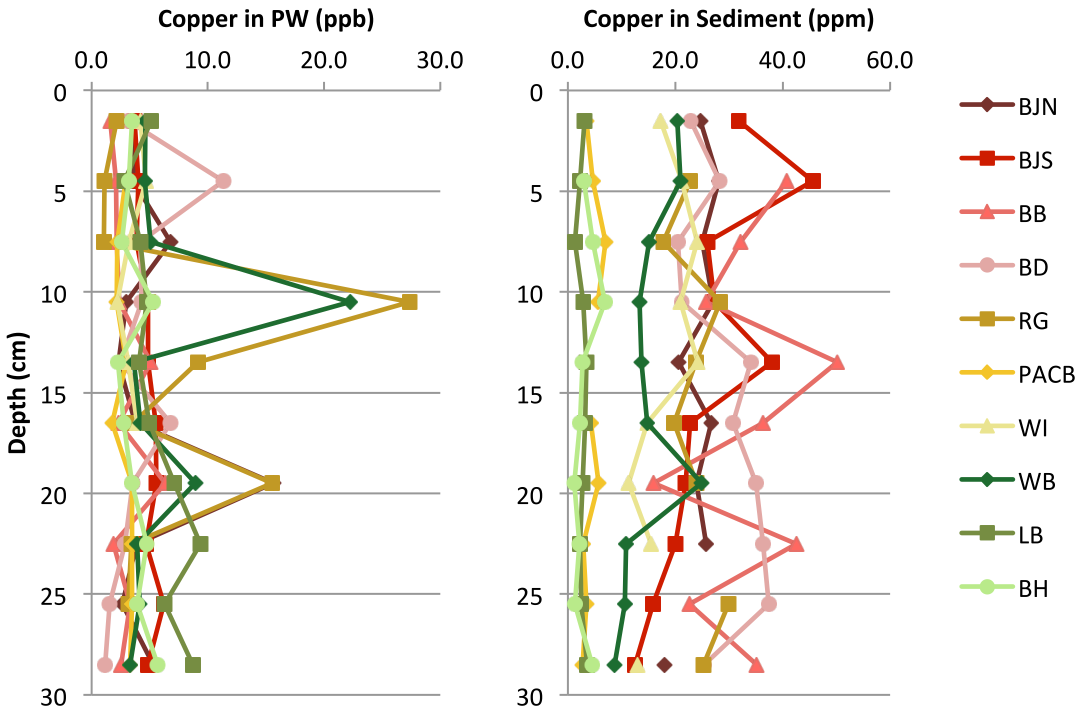

Figure 30. Plot of copper concentrations with depth as measured in pore waters (left) and sediments (right; after Keevan, 2012 and Natter; 2012). Unlike most other metals, copper in pore water does not display any correlation with the degree of oil contamination; however, in sediments, copper concentrations increase with higher degrees of oil contamination.
[Heavily contaminated sites colored in shades of red; moderately contaminated in yellow; pristine in green.]

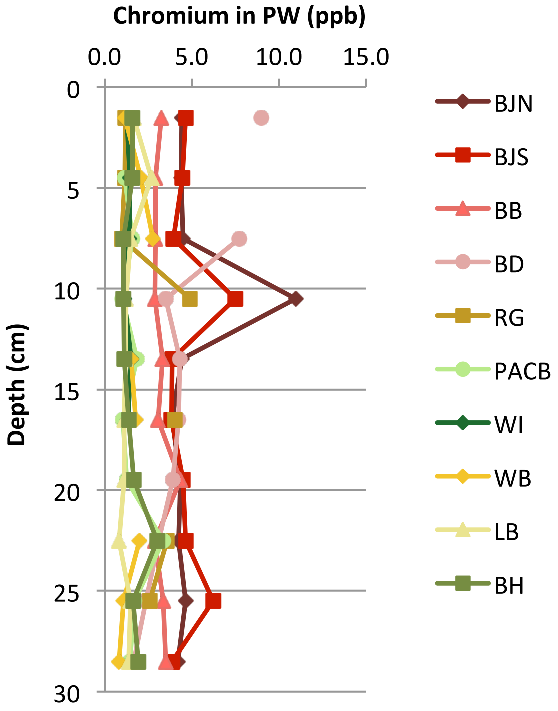

Figure 31. Plot of chromium concentrations with depth as measured in pore waters. Such low concentrations (most <5 ppb) make interpretations difficult. At site BD, unusually high concentrations of chromium at depths <5 cm may indicate the effects of an enclosed environment that lacks tidal flushing.

[Heavily contaminated sites colored in shades of red; moderately contaminated in yellow; pristine in green.]

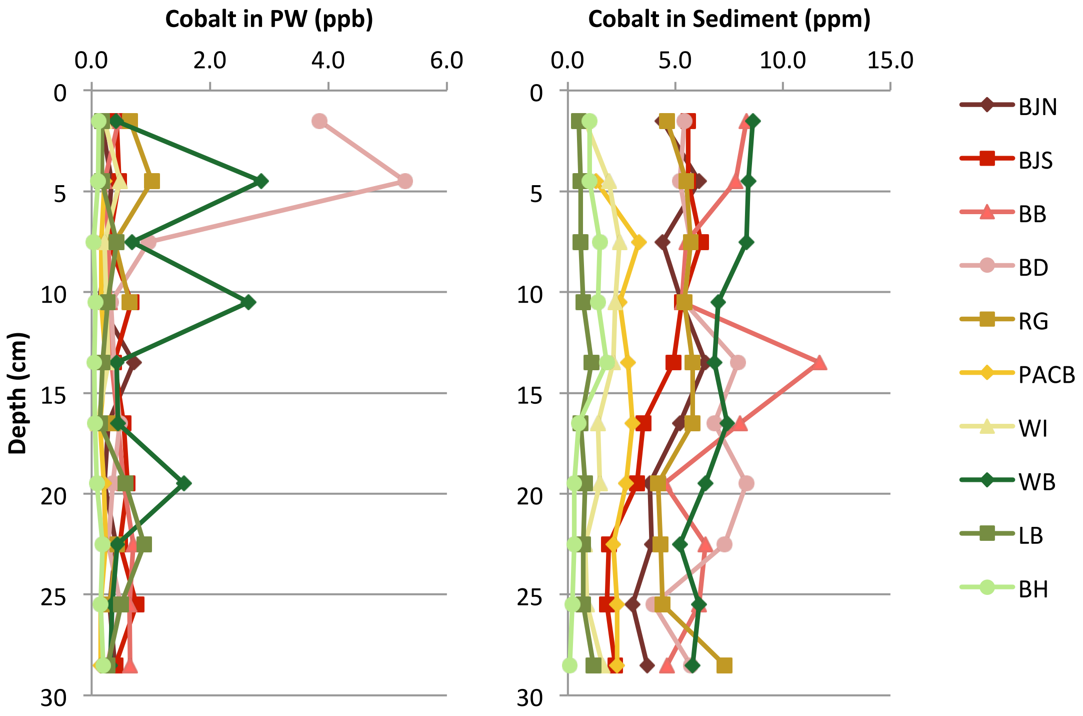

Figure 32. Plot of cobalt concentrations with depth as measured in pore waters (left) and sediments (right; after Keevan, 2012 and Natter; 2012). Cobalt concentrations in sediments vary with degree of contamination; however, cobalt concentrations in pore waters show no such trend.
[Heavily contaminated sites colored in shades of red; moderately contaminated in yellow; pristine in green.]

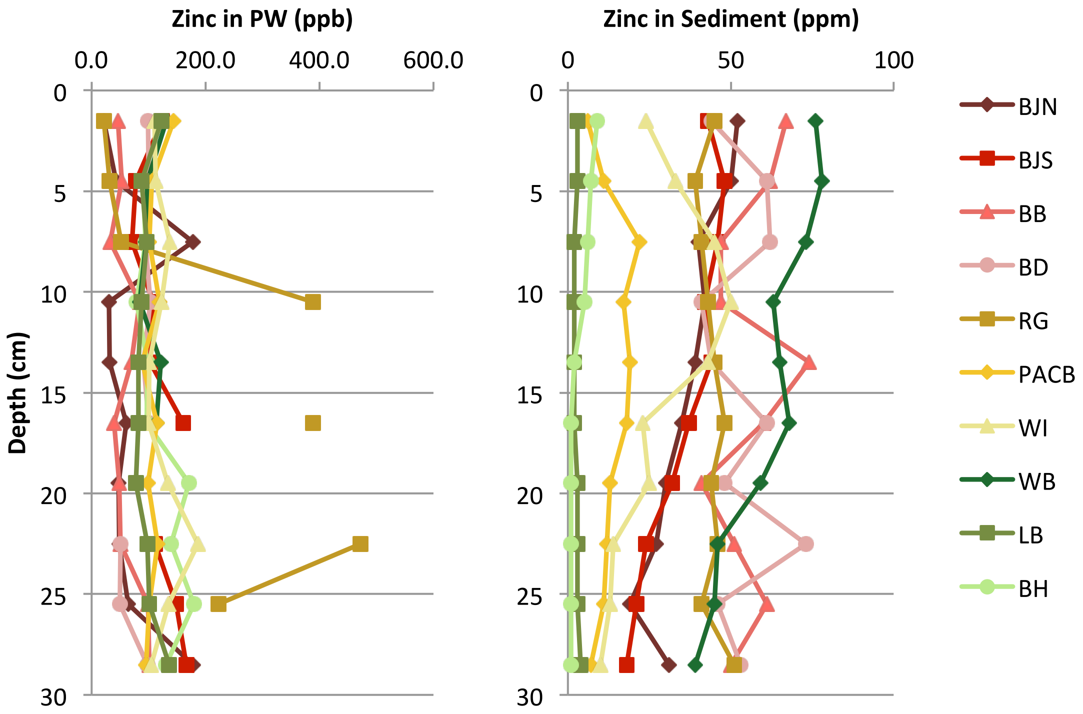

Figure 33. Plot of zinc concentrations with depth as measured in pore waters (left) and sediments (right; after Keevan, 2012 and Natter; 2012). Zinc concentrations of sediments generally increase with degree of oil contamination.
[Heavily contaminated sites colored in shades of red; moderately contaminated in yellow; pristine in green.]

Geochemical Modeling

Several types of geochemical models were constructed to investigate the evolution of geochemical conditions in coastal saltmarshes in response to spilled oil and saltwater intrusion. These models include: (1) the speciation of Fe phases in the presence of S, (2) the transformation of Fe oxides and sulfides in response to inflow of oil and changes in redox conditions, and (3) the adsorption and sorption of arsenic under different geochemical conditions. Activity-activity diagrams illustrate the minerals thermodynamically favored to precipitate due to the shift in geochemical conditions augmented by spilled oil. Reaction path models illustrate the partition of metals among aqueous and solid phases and their sorption reactions with pyrite and hydrous ferric oxides due to changes in Eh, pH, and ionic-competition processes.

Activity Model

Figure 34 displays a calculated activity diagram for an Fe-S system based on varying pH and activity of hydrogen sulfide. The diagram outlines the stability fields for iron phases at varying conditions. H_2S and pH measurements of pore waters at oiled sites (listed in Appendix 2) are projected as black dots within the stability field. The clustering of Gulf saltmarsh geochemical conditions within the pyrite field indicates the thermodynamic stability of pyrite under reducing conditions. The formation of pyrite and other iron sulfides is dependent upon the activity of e- (pE); enhanced microbial respiration spurred by an oil spill likely creates highly reducing conditions, so the model in Figure 34 assumes a low pE value of -3. The geochemical manifestation of this activity model was shown previously by Keevan (2012) and Natter (2012), who reported high quantities of framboidal pyrite crystals within heavily contaminated Gulf coast marsh sediment.

Oiled saltmarsh pore water is characterized by relatively high pH values and very high H_2S concentrations (Natter et al., 2012). High pore water pH and sulfide concentrations reflect the combined effects of seawater intrusion and possibly enhanced bacterial sulfate reduction induced by spilled oils. Pyrite will remain stable in neutral pH or slightly alkaline conditions, but an increase in pH to 8.5 or more indicates the beginning of pyrite dissolution. Additionally, more oxidized conditions (with less negative pE) may reduce the stability of pyrite. Oiled saltmarshes likely maintain highly reducing conditions due to high organic carbon contents and active microbial processes. Organic matter, especially those associated with the heavy fraction of spilled oils, can remain in marsh sediments for decades (Natter et al., 2012).

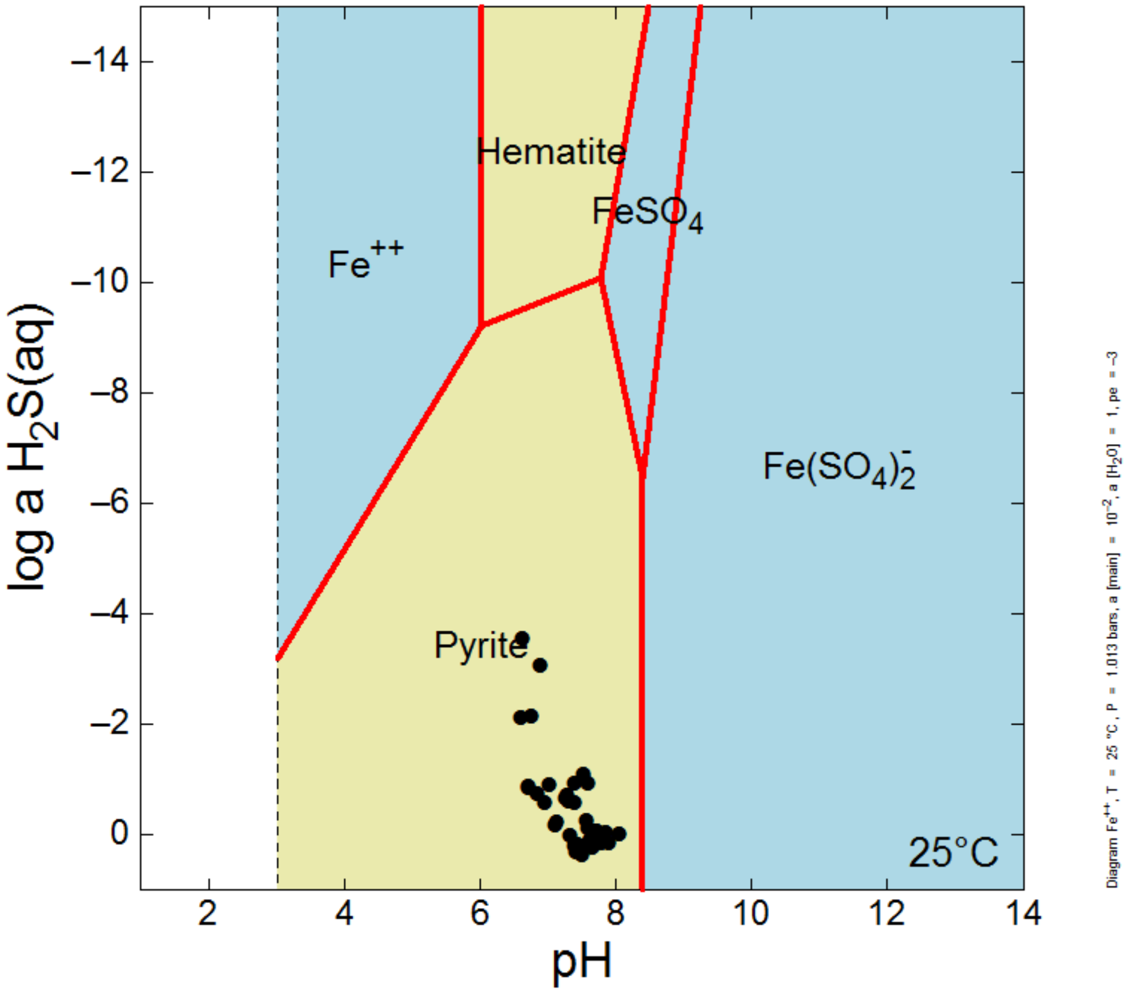

Figure 34. Plot showing stability field of Fe^{2+} under varying pH and H_2S conditions, assuming a pE of -3. The measured pH and concentrations of H_2S at each site (Appendix 2) are plotted as black dots. The diagram was calculated using the ACT2 subprogram of Geochemist's Workbench.

Mineralogical Reactions Resulting from Inflow of Organic Matter

The second geochemical model was constructed to trace the mineralogical reactions resulting from inflow of oil and organic matter. The initial geochemical condition was set by equilibrating seawater (Table X) with hematite (a proxy of Fe(III) oxyhydroxides) under oxidized conditions (Eh = +0.1 V) at 25°C. The model then simulates the biogeochemical effects of titration of acetate (a proxy of organic matter) into the system. In the simulation, fluid reactants containing 500 μmol of CH_3COO^- were added into the system over the course of the reaction path. To calculate the effect of microbial metabolism processes associated with sulfate-reducing bacteria, the fluid redox potential Eh decreases linearly from +0.1 V to -0.2 V over the course of the reaction path. The accompanying mineralogical reactions were calculated. The transformation of hematite is considered as follows:

$$4\ Fe_2O_3\ (\text{hematite}) + CH_3COO^- + 15\ H^+ \rightarrow 8\ Fe^{2+} + 2HCO_3^- + 8H_2O \qquad (1)$$

Here, hematite (as electron acceptor) is reduced to ferrous iron, and acetate (as electron donor) is broken down into simple forms of HCO_3^- in the system. The reduction of sulfate in seawater may be expressed as:

$$SO_4^{2-} + 2\ CH_3COO^- + 2H^+ \rightarrow H_2S + 2\ HCO_3^- + 2H_2O \qquad (2)$$

Hydrogen sulfide (H_2S) produced by bacterial sulfate reduction can quickly react with dissolved metals (e.g., Fe^{2+}) to precipitate iron sulfides such as pyrite:

$$Fe^{2+} + H_2S(aq) \rightarrow FeS(solid) + 2H^+ \qquad (3)$$

The modeling results (Figure 35) show the effect of decreasing redox potential (Eh) and the inflow of organic matter on the precipitation and dissolution pathways of various minerals. First, hematite becomes thermodynamically unstable as Eh drops. Sulfide produced by bacterial sulfate reduction then reacts with ferrous iron to form pyrite at Eh <0.1 V. Previous studies

(Saunders et al., 2008; Lee et al., 2013) have shown that Fe-sulfides formed in reducing systems also sequester many other dissolved metals and metalloids (e.g., As, Cu, Ni, Co, Zn, U, Pb, etc.). Bicarbonate produced by the breakdown of organic matter (acetate) may react with Ca and Mg in seawater to form carbonate minerals. However, such reactions may be kinetically prohibited in a short span of time.

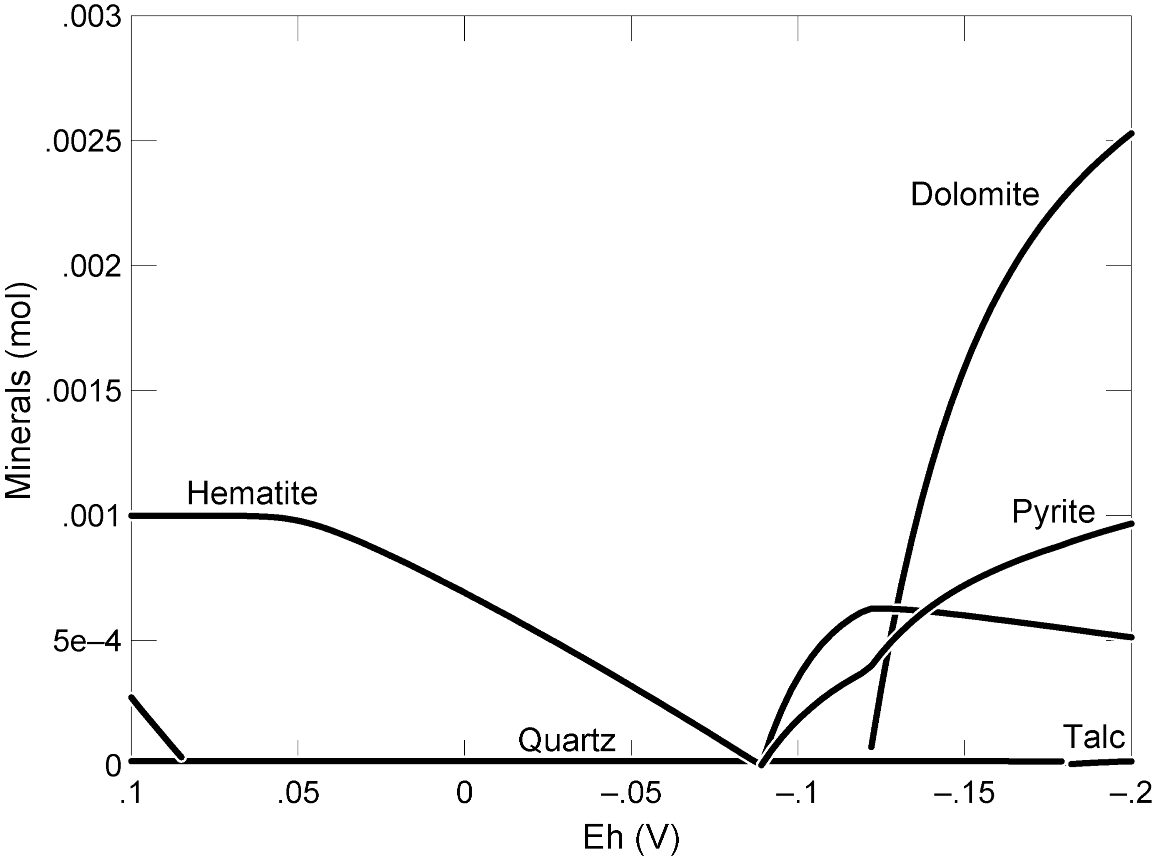

Figure 35. Plot showing reaction paths of hematite, pyrite, and dolomite as Eh changes from positive (0.1 V) to negative (-0.2 V). Hematite is shown to dissolve, whereas pyrite and dolomite are shown to precipitate.

Saltwater Intrusion and Desorption of Arsenic – pH Effects

The third geochemical model employed the surface complexation theory of Dzombak and Morel (1990) to simulate the desorption of arsenic species associated with oxide minerals in response to saltwater intrusion in coastal environments. The intrusion of seawater in shallow alluvial aquifers may lead to desorption of arsenic from the surface of hydrous ferric oxides (HFOs) due to pH effects and ionic competition for HFO sorbing sites. The initial system contains 1 kg of fresh groundwater (Table 1) equilibrated with 1 g of $Fe(OH)_3$ at pH 7. The groundwater contains 1 µg/kg of As(III), 1 µg/kg of As(V), and 0.05 molal of NaCl. The calculation prevents the redox coupling between As(III) and As(V). Ferric hydroxides used in the simulation have high specific surface areas (600 m^2/g) for sorption reactions. The surface of HFOs is composed of weakly sorbing sites (density = 0.4 mol/mol mineral) and strongly sorbing sites (density = 0.01) (Dzombak and Morel, 1990; Bethke, 2008). The simulations assess desorption of various arsenic species in response to pH increases caused by saltwater intrusion. Seawater pH ranges from 7.5 to 8.5.

Modeling results (Figure 36) illustrate the changes of dissolved arsenic concentrations as pH increases from 7 to 9. At a starting pH of 7, 19.5 mg/kg of As are sorbed onto HFOs (19.22 mg/kg as As(V) and 0.28 mg/kg as As(III)). Therefore, at near-neutral pH conditions, arsenic shows a strong tendency to adsorb to the surfaces of HFOs. Iron oxyhydroxides with a net positive surface charge have a high capability to adsorb the negatively-charged anionic complexes of As(V), such as AsO_4^{3-}. By contrast, an HFO's adsorption capabilities for the non-ionic complexes (e.g., $As(OH)_3$) of As(III) are poor. The adsorption and desorption tendencies of all complexes are affected by changes in pH. Figure 37 shows significant desorption of As(V) and minor desorption of As(III) as pH increase from 7 to 9. At higher pH, the surfaces of HFOs become negatively charged and tends to expel anions of As(V) complexes. The rise in arsenic concentrations as pH passes through the range of typical seawater simulates the potential desorption reactions induced by saltwater intrusion. At a final pH of 9, arsenic concentrations in sorbate decreased to 19.0 mg/kg, whereas the final arsenic concentrations in fluid increased to over 500 µg/kg (Figure 37), fifty times higher than the maximum contamination level of arsenic set by the EPA.

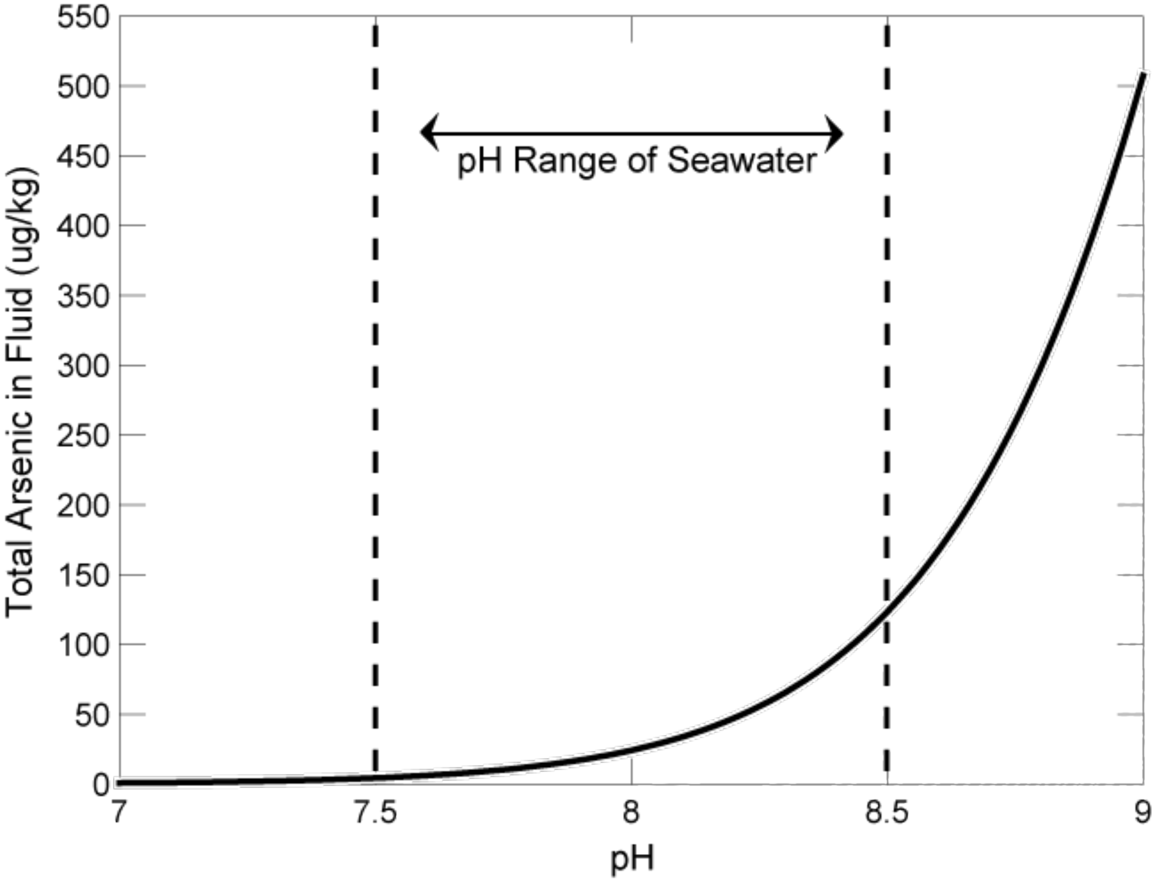

Figure 36. Model results showing a rise of total arsenic concentration in solution due to desorption processes from HFOs as pH increases from 7 to 9, passing through the range of typical seawater.

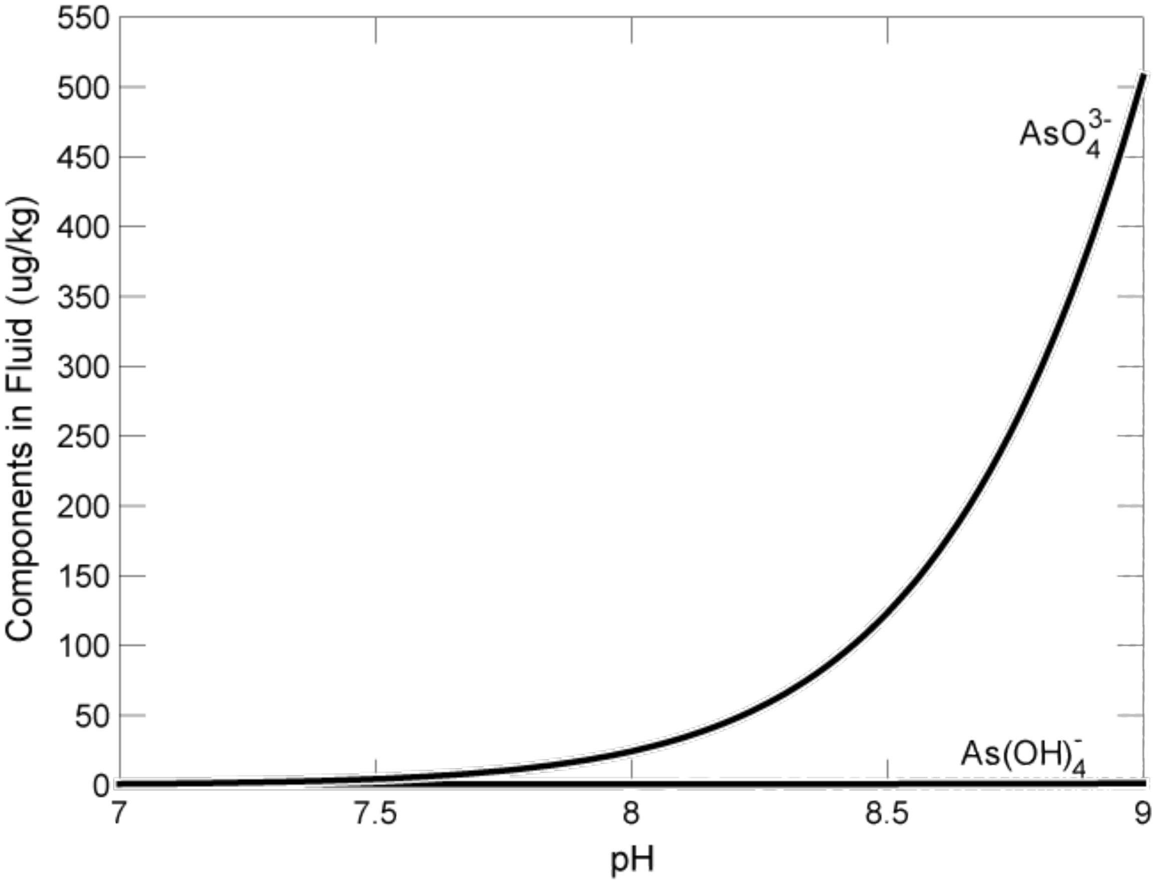

Figure 37. Plot of model results showing a rise of arsenic concentrations in solution for each arsenic complex of As(III) and As(V) as pH increases from 7 to 9.

Saltwater Intrusion and Desorption of Arsenic – Effects of Ionic Competition

The fourth model was conducted to investigate arsenic desorption resulting from the introduction of competing ions (e.g. silicates, carbonate, calcium, sulfate, etc.) with seawater. This model begins with a 1 kg basis of typical freshwater (see Table 1) in equilibrium with As-sorbed HFOs. Figure 38 illustrates the changes in fluid chemistry as increasing amounts of seawater (Table 2) are titrated into the system. As they account for a large portion of dissolved ions in seawater, Ca^{2+} and SO_4^{2-} increase at a linear rate with the steady titration of seawater. The added saltwater contains no dissolved arsenic; therefore, the only possible source of increasing arsenic within the fluid is the desorption of arsenic from HFOs in the initial freshwater system. Calculated concentrations of these ions in HFO sorbate (Figure 39) further support this hypothesis. In the early stages of saltwater titration, the concentration of ions Ca^{2+} and SO_4^{2-} increase within the fraction of sorbate; in contrast, AsO_4^{3-} decreases in sorbate concentration as it is desorbed and replaced by Ca^{2+} and SO_4^{2-}. Similar to the effects of rising pH, the fraction of sorbed arsenic decreases and the concentration of arsenic in solution increases to more than 25 μg/kg (Figure 40). However, in this case, the removal of sorbed arsenic is due to the high concentrations of competing ions within the intruding saltwater.

Two controlling processes appear to be occurring in Figure 39. In the earliest stages of seawater titration, changes in Ca^{2+} and SO_4^{2-} sorbate concentrations are positive, whereas arsenic concentrations are decreasing. This is likely due to the competing ion effect between newly introduced ions and previously sorbed arsenic ions. As titration of seawater continues, sorbing surfaces of oxides are quickly occupied by various ions present in seawater. The sorbed concentrations of Ca^{2+} and SO_4^{2-} in sorbate peak after the addition of only about 0.1 kg of seawater and then level off (Figure 39). The cessation of sorption at higher salinities indicates that HFO surfaces possess a finite number of sorption sites, which is consistent with the Langmuir sorption isotherm. It is unclear why the concentrations of Ca^{2+} and SO_4^{2-} in sorbate slowly decline after the adsorption capabilities of HFOs peak. The addition of seawater and subsequent increase in ionic strength may reduce the stability of the HFOs and their overall adsorption capacity.

Each of the factors discussed here may impact desorption of arsenic and other metals in coastal wetlands. Saltwater intrusion raises the overall pH of a system, which may alter the overall surface charge of iron oxyhydroxides and therefore encourage the desorption of arsenic anionic complexes. Further desorption from HFOs may occur as a result of ionic replacement by the introduction of competing ions dissolved in seawater. Minor desorption also may occur as a result of iron oxyhydroxide dissolution, which decreases the availability of sorbing sites. Metals contamination from spilled oil threatens the coastal water resources. The sequestration of toxic metals into pyrite and hydrous ferric oxides (HFOs) may help to mitigate groundwater contamination concerns. The modeling results demonstrate that the mobility and transformation of trace metals are strongly influenced by multiple factors, including Eh, pH, ionic strength, sorption, and mineral precipitation and dissolution.

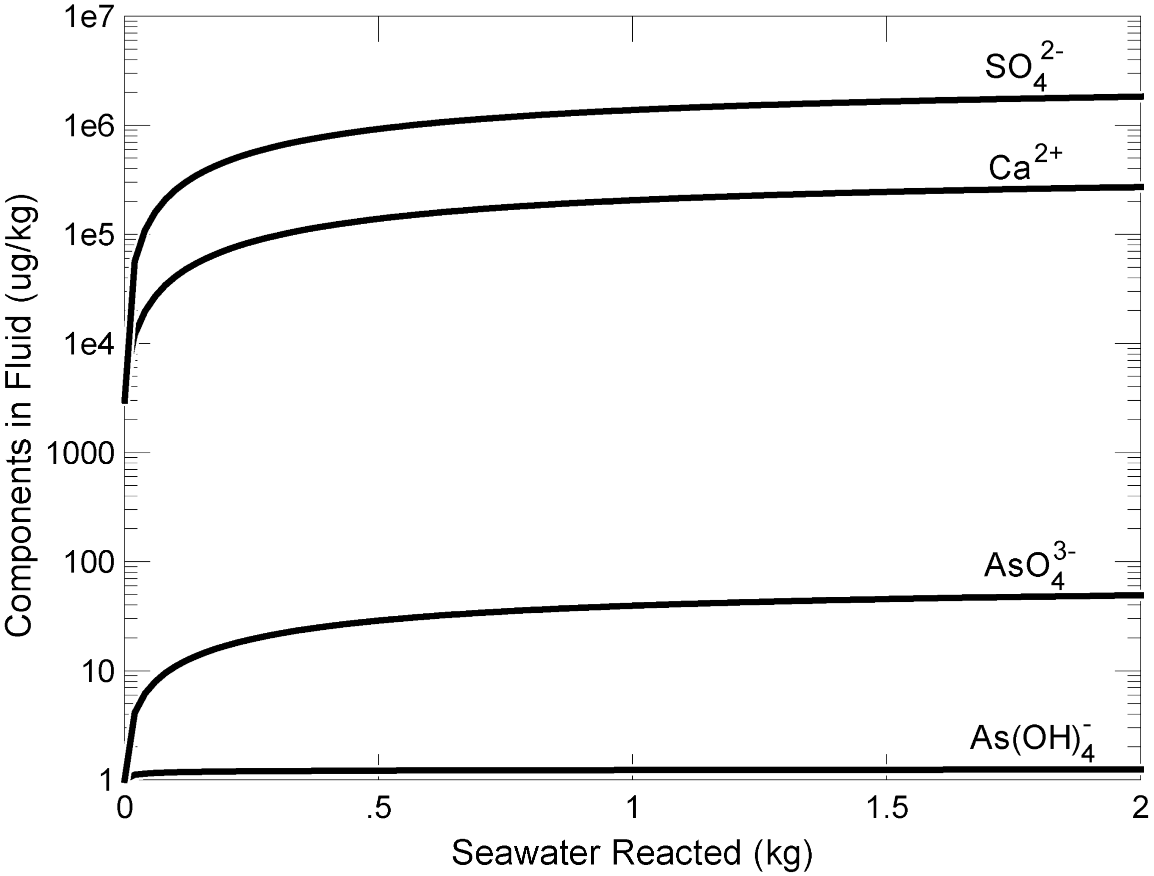

Figure 38. Plot of model results showing the reaction path of dissolved ions Na^+, Cl^-, AsO_4^{3-}, and $As(OH)_4^-$ through titration with saltwater. Na^+ and Cl^- increase linearly during titration, whereas arsenic complexes increase at the rate that they are desorbed from hydrous ferric oxide surfaces.

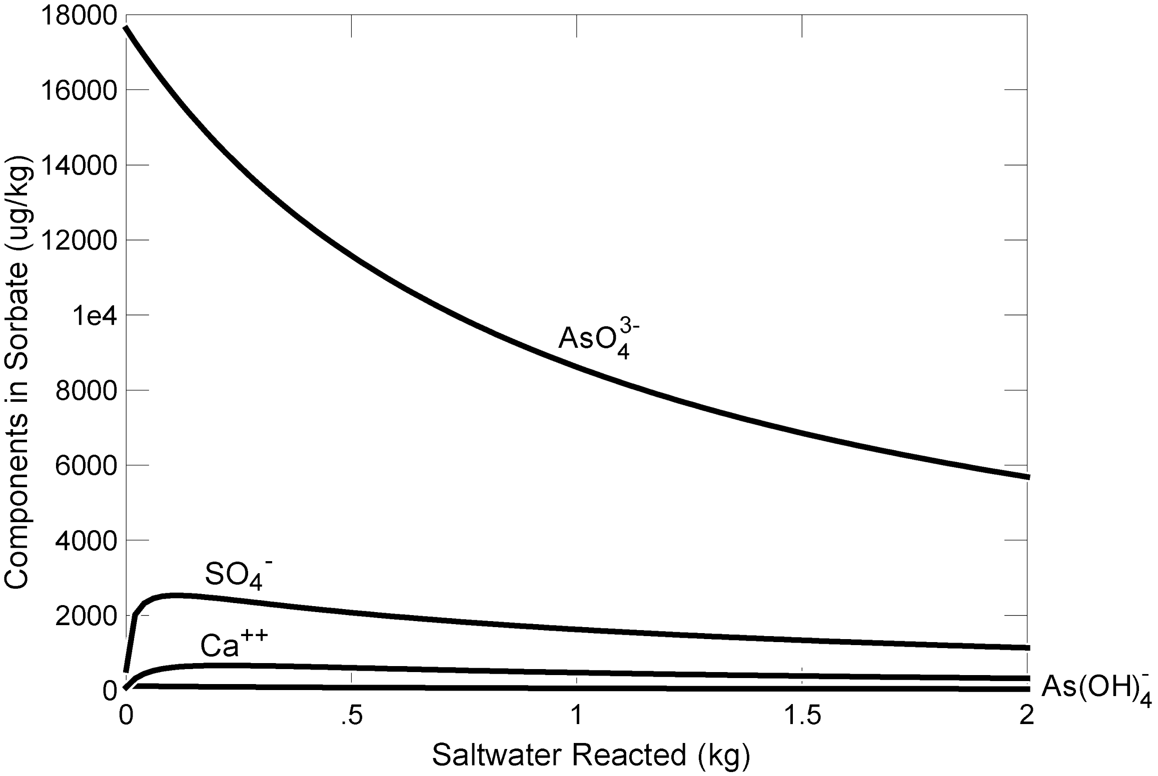

Figure 39. Plot of model results showing the reaction path of sorbate constituents Ca^{++}, SO_4^{2-}, AsO_4^{3-}, and $As(OH)_4^-$ through titration with seawater. Whereas Ca^{++} and SO_4^{2-} increase in sorbate concentration, AsO_4^{3-} rapidly decreases as a sorbate component due to replacement by Ca^{++} and SO_4^{2-}.

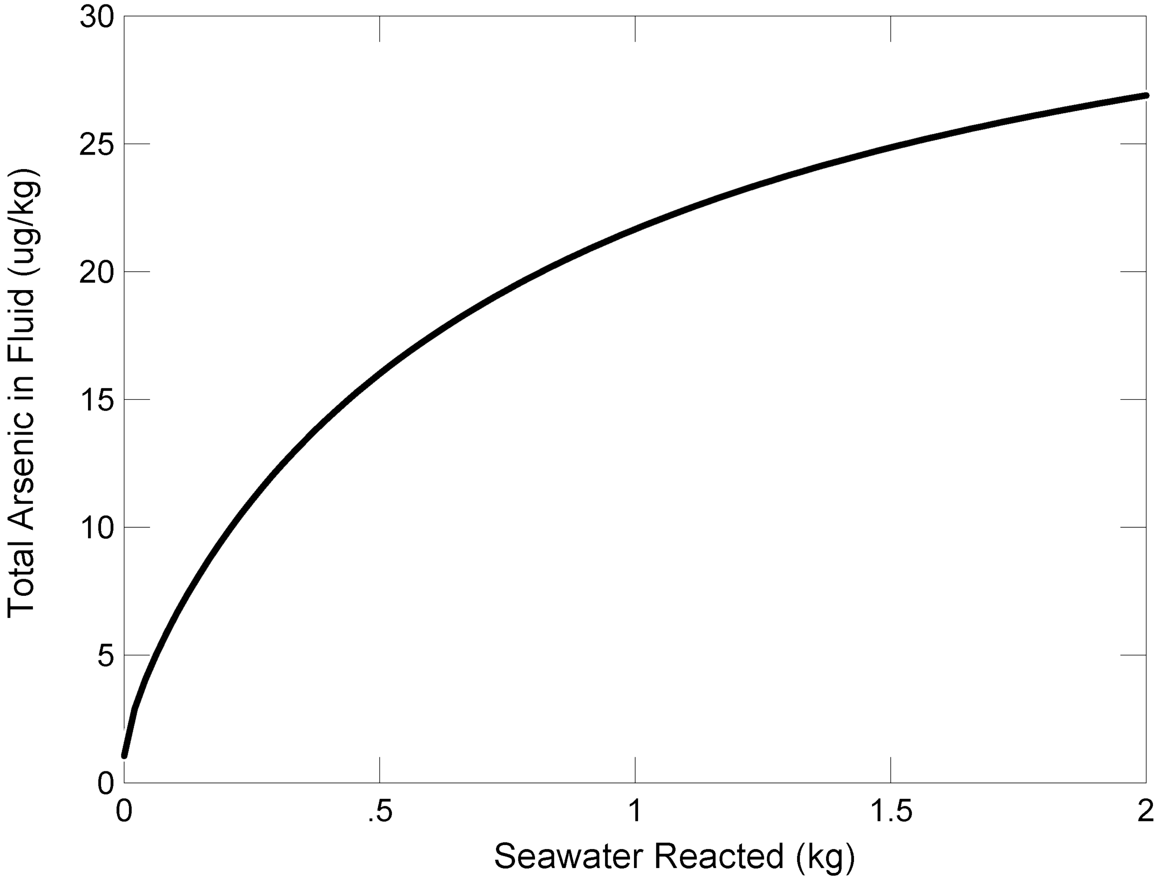

Figure 40. Plot of model results showing how concentrations of arsenic in solution increase as a result of titration with seawater. Arsenic complexes are desorbed from the surface of HFOs as sorbing sites are replaced by competing ions introduced by seawater.

Hydrodynamics of Saltwater and Oil Intrusion

Aquifer Tank Experiments

Elevated levels of organics, whose fingerprint matches that of the MC-252 wellhead, were found at depths down to 15 cm in Gulf wetland sediments (Natter et al., 2012). It was suspected that saltwater intrusion dynamics along Gulf coastlines might control the presence of crude oil down to such depths. To investigate the interactions of saltwater, freshwater, and oil, a laboratory-scale hydrogeologic tank, designed by Matt Obley (Lee et al., 2012) was employed in several modeling experiments.

Saltwater intrusion at depth: The first tank experiment was developed to locate the position of a saltwater wedge. To facilitate observations over a reasonable timeframe, the tank was packed with glass beads with high permeability (see Permeameter Study below). Highly permeable media allow the hydrologic system to quickly adjust to a steady state in response to changes in hydraulic head. For the experiment, freshwater was first transmitted through the tank via the freshwater chamber at a fixed hydraulic gradient. Once saturated with freshwater, saltwater (salinity = 0.48 molal, dyed red) was injected into the system at a constant rate via a constant-head saltwater chamber. Overflow outlets controlled the water levels in both the freshwater and saltwater chambers. The first saltwater wedge (Figure 41, top) was created with a saltwater head of 25.5 cm and freshwater head of 27.0 cm (relative to the bottom of the tank). The dense saltwater rapidly intruded along the bottom of the aquifer from left to right to form a steady saltwater wedge. Once the first wedge was stabilized, the saltwater head was raised by 0.8 cm to 26.3 cm to simulate saltwater intrusion processes. The rise in saltwater head prompted the progradation of the wedge to the right until it once again stabilized after about 3.5 minutes.

Propagation of the saltwater front illustrates the dynamics of density-driven saltwater intrusion outlined in the Ghyben-Herzberg equation (Freeze and Cherry, 1979). The Ghyben-Herzberg relationship equates z to roughly $40 \times h_f$ (Figure 42), where z is the depth of freshwater below sea level and h_f is the height of freshwater above sea level. According to the Ghyben-Herzberg equation, an increase in saltwater head by 0.8 cm, or a decrease in freshwater head by the same amount, would lead to a decrease of z value by 32 cm (i.e., saltwater front will rise by

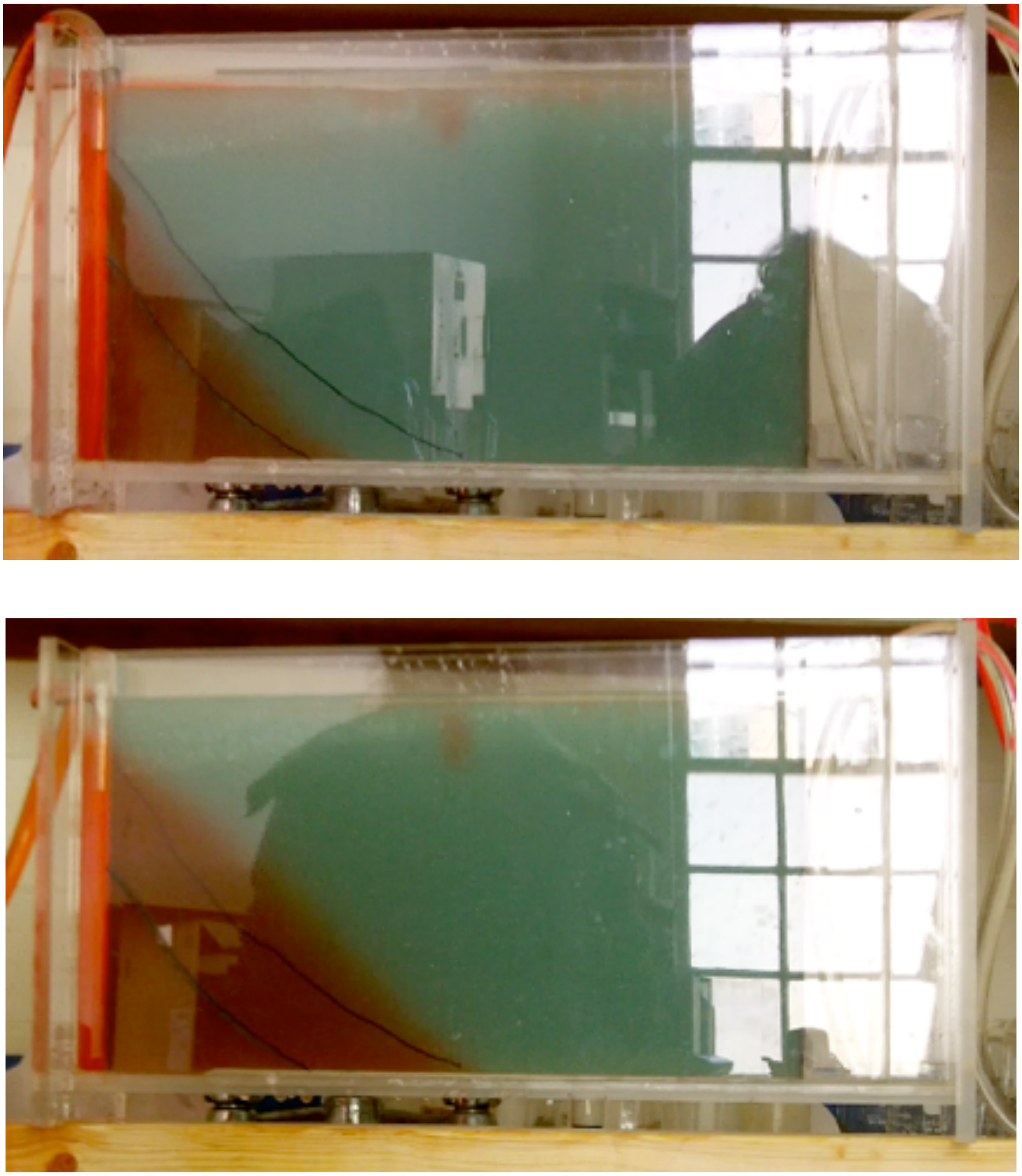

Figure 41. Photographs of initial (top) and final (bottom) stages in the first tank experiment to build a steady freshwater-saltwater interface in response to a 0.8 cm increase in saltwater head. Total time elapsed: 3.5 minutes.

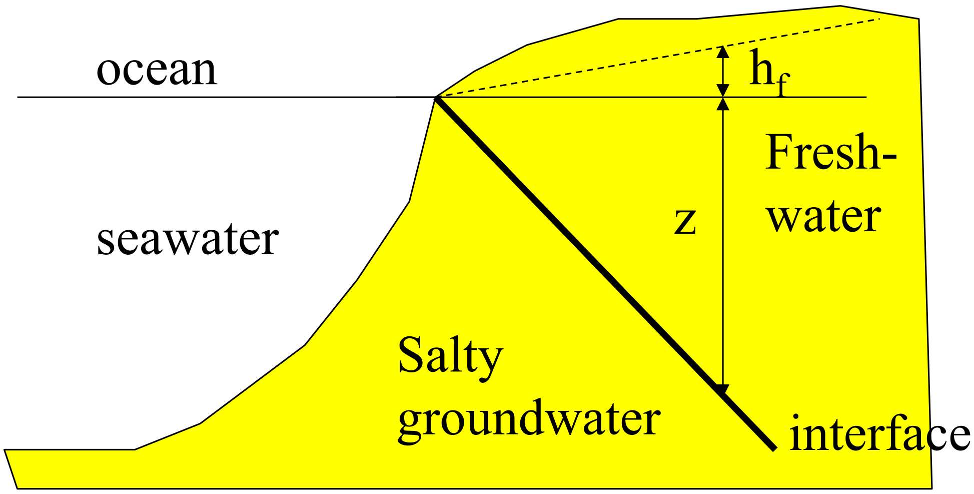

Figure 42. Illustration of the Ghyben-Herzberg equation, which governs the saltwater-freshwater interface under hydrostatic conditions (Freeze and Cherry, 1979).

32 cm). The experimental results (Figure 41), however, resulted in a lower *z* (<10 cm). In the tank setup and real aquifer situations, freshwater flow tends to push the saltwater further offshore. The Ghyben-Herzberg equation assumes a simple hydrostatic (i.e., no-flow conditions) balance between freshwater and saltwater, thus underestimating the depth to the saltwater front. A more accurate position of the saltwater front can be determined for any given boundary condition by groundwater flow and solute transport modeling (see Numerical Modeling section below).

At heavily oiled Louisiana sites, greater pore-water levels of dissolved organic carbon (DOC) are found at depth (Figure 43), indicating mixing of saltwater, freshwater, and oil below the sediment surface. DOC in near-surface sediments may be reduced by freshwater recharge from rainfall or shallow fresh groundwater. This tank experiment demonstrates that it is also very likely that seawater and perhaps oil may invade along the deeper portion of the marsh sediments. This result suggests that not all spilled oil rose to the surface; a fraction of oil, especially heavier compounds, may have spread downward through the water column and ultimately contaminated underlying sediments.

Saltwater infiltration along the surface: In the second tank experiment, a new source of saltwater was introduced at the sediment surface to simulate conditions in which seawater and spilled oil wash ashore during high tide. The experiment began with the formation of a stable interface between freshwater and red-dyed saltwater (h = 25.5 cm; salinity = 0.48 molal). Then, a separate saltwater solution of the same salinity, dyed blue, was added to the system from the top surface of the glass beads (Figure 44). This experiment was designed to show the interactions of a deeper saltwater wedge with seawater onlapping onto the coast above; it was hypothesized that the onlapping seawater at the surface (dyed blue) would migrate downward through the freshwater aquifer due to its higher density. The infiltrating saltwater, due to mixing with surrounding freshwater, would become diluted and less dense than the salty groundwater below the saltwater-freshwater interface.

Figure 44 shows a stable red saltwater wedge and the introduction of blue saltwater through a funnel at the tank’s surface. As more blue saltwater was added to the system, it became clear that the blue saltwater’s primary direction of movement was toward the left and bottom of the tank. The blue saltwater infiltrated down from the surface, mixed with surrounding freshwater, and then flowed left under the hydraulic gradients of the freshwater regime. Originally, the blue saltwater did not reach the deep saltwater wedge interface as it discharged into the left saltwater chamber. To increase interaction between the blue and red saltwater, the input location of the blue saltwater was shifted further to the right (Figure 45). Figure 46 shows the first stage of interaction between blue and red saltwater after continued input of blue saltwater. As the blue plume reached the saltwater wedge, the saltwater-freshwater interface was pushed downward and formed local depressions, but the toe of the wedge remained in place. Finally, Figure 47 shows the continued interactions of red and blue saltwater after the input of blue saltwater ceases.

At the onset of the experiment, the interface between freshwater and red saltwater was linear; however; the introduction of blue saltwater disrupted the linear interface. At the end of the experiment (Figure 47), the interface between red and blue saltwater appears scalloped. Additionally, some small red saltwater fingers can be seen extending upward several centimeters into the descending blue plume.

The interactions of the two saltwater sources observed in the tank experiments reveal possible oil intrusion mechanisms along the Gulf coast. If the blue saltwater near the surface also contained a crude oil mixture, the experiments illustrate one mechanism by which the spilled oil potentially infiltrated into coastal sediments as deep as 12-15 cm. Along the interface of red and blue saltwater (Figure 47), blue saltwater is being driven left by freshwater flow and upward as it reaches the barrier of denser red saltwater. The effect of these two directional forces creates scallops in the upper boundary of the red saltwater wedge. The mixing and swirling at the saltwater wedge front also creates small upwellings of red saltwater. A schematic of this interpretation is shown in Figure 48.

The presence of MC-252 crude oil and high pore water DOC contents at depths > 15 cm may be the result of either of the two intrusion processes illustrated in the tank experiments. It is possible that heavier fractions of crude oil penetrated into deeper sediments through either the movement of a saltwater wedge at depth or through the infiltration of onlapping seawater. The initial saltwater wedge occurs as a result of differences in density and is controlled by the differences in saltwater and freshwater heads. The infiltration of surficial saltwater is controlled by both density-driven and hydraulic gradients of freshwater (i.e., topographic-driven) flow.

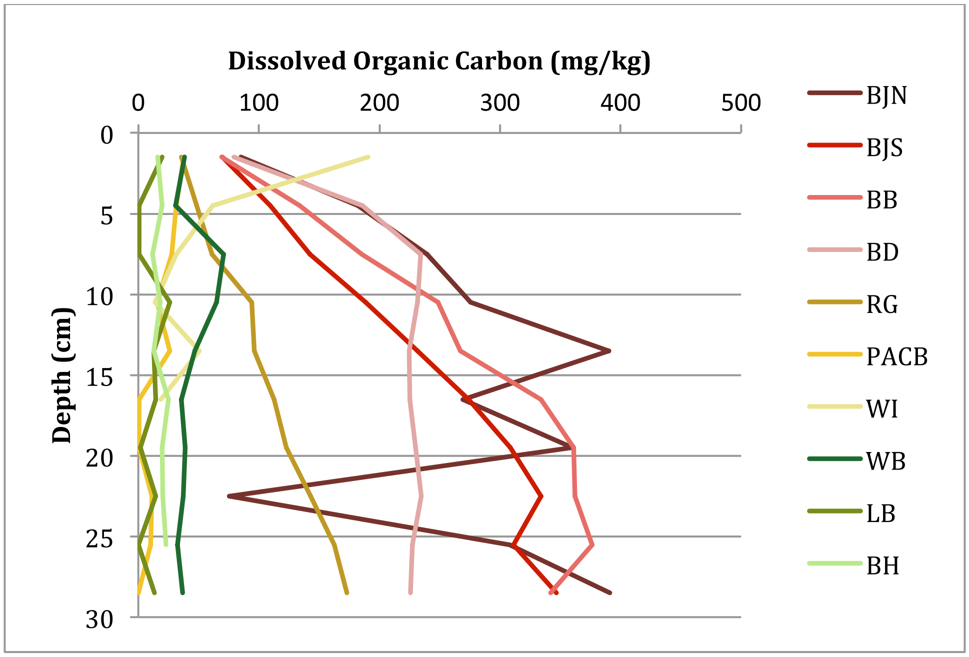

Figure 43. Plot showing the depth profile of dissolved organic carbon (DOC) in sediments at various saltmarsh sites (Natter et al., 2012). Contaminated sites show much higher DOC levels compared to those at non-contaminated sites.

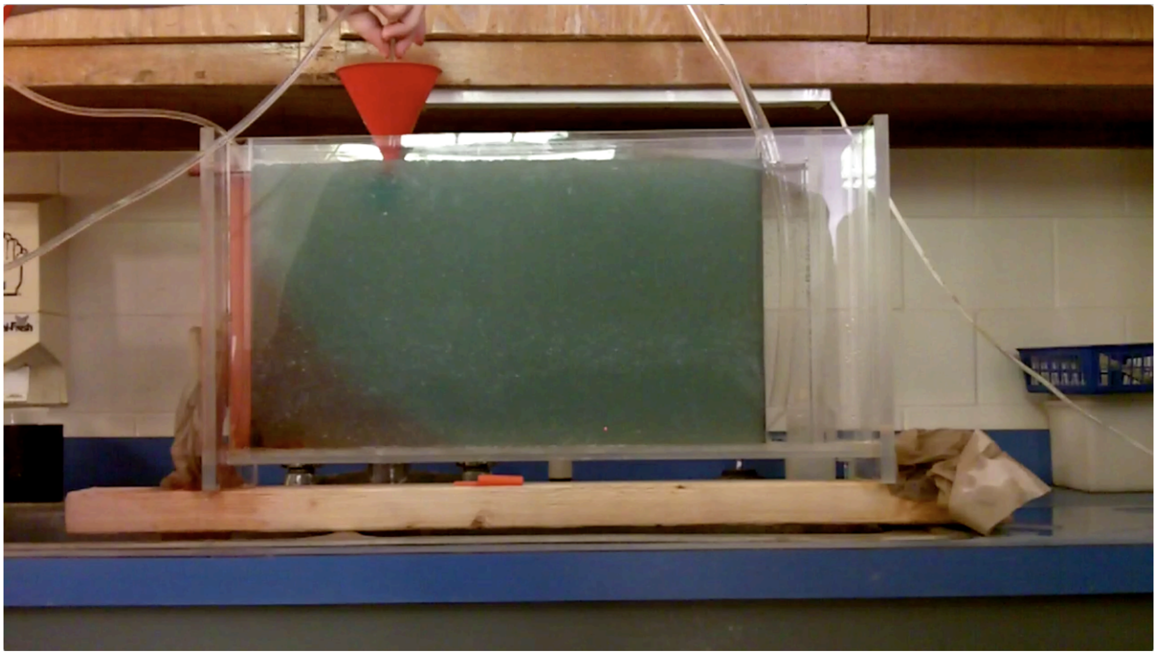

Figure 44. Photograph showing the introduction of a second saltwater source (dyed blue) near the tank's surface.

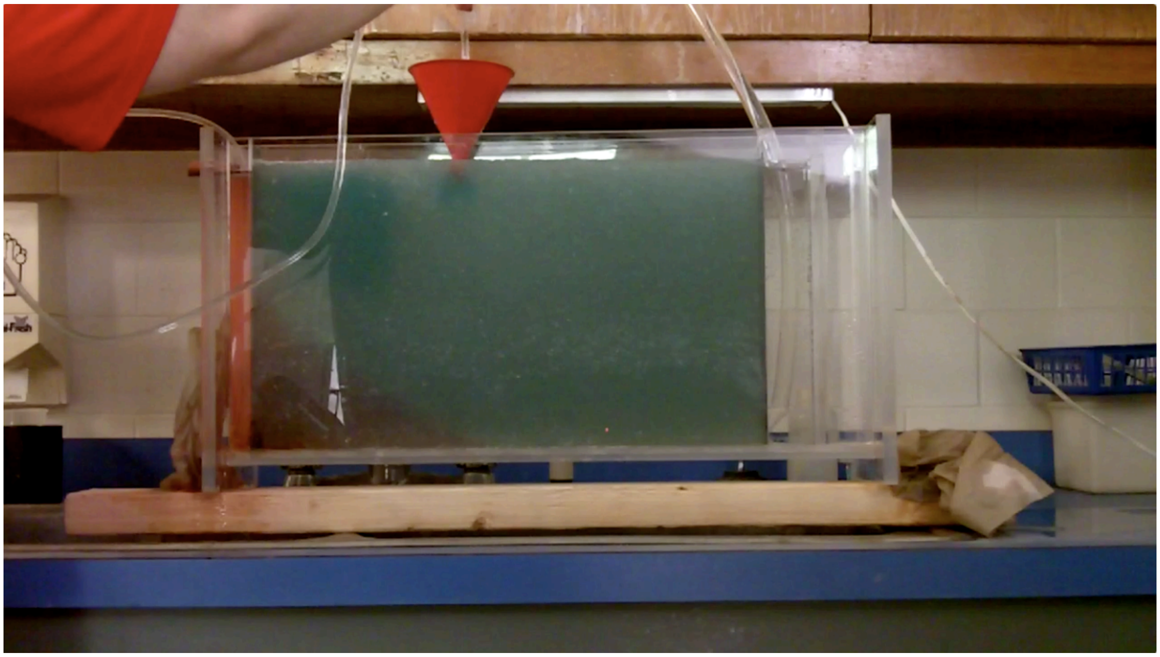

Figure 45. Photograph showing the transition of the blue saltwater sources further toward the center of the tank allows blue saltwater to reach the red saltwater wedge at depth.

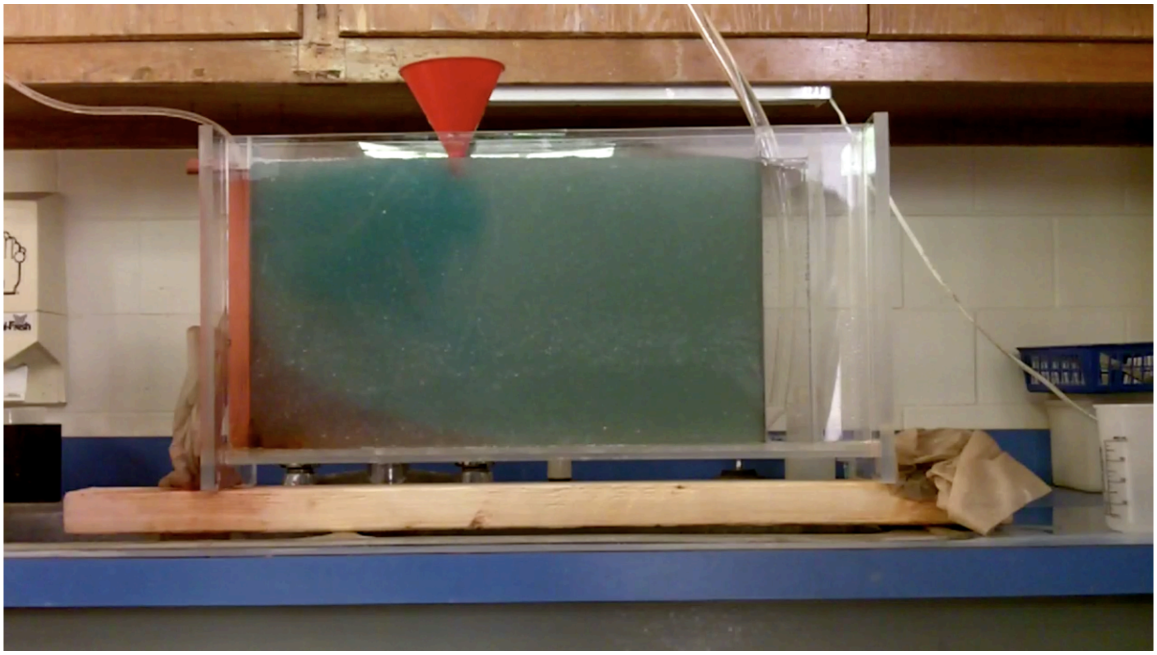

Figure 46. Photograph showing how blue saltwater follows a downward and leftward movement toward the original red saltwater-freshwater interface.

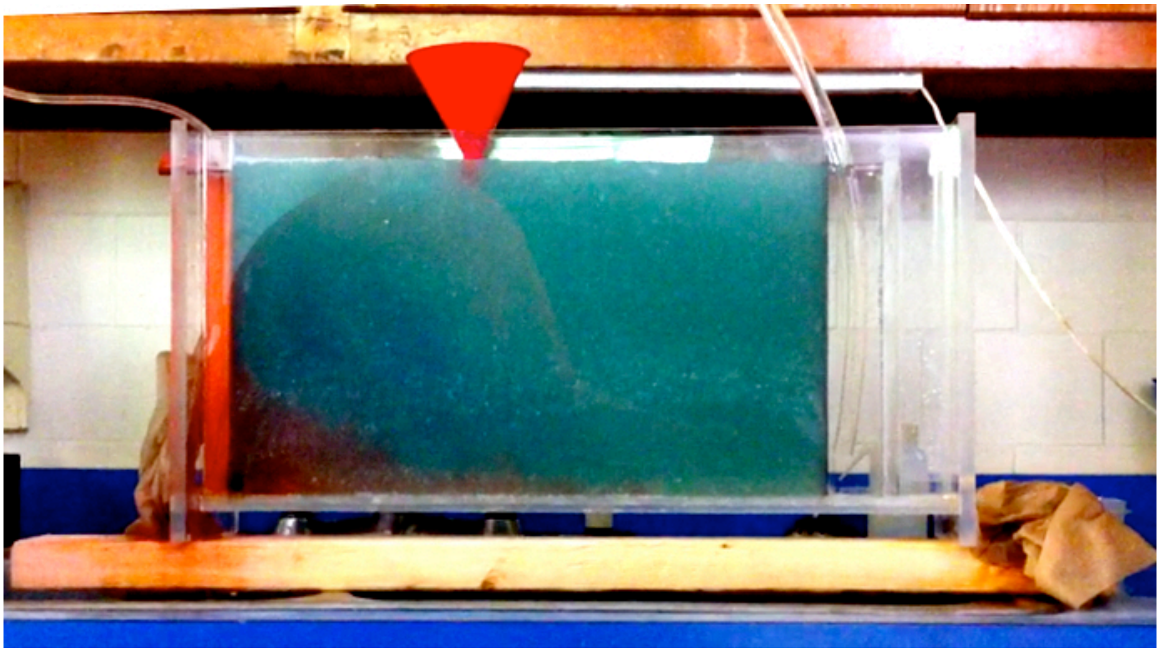

Figure 47. Photograph of blue saltwater reaching the red saltwater wedge. Red saltwater fingers can be seen growing upward through blue saltwater.

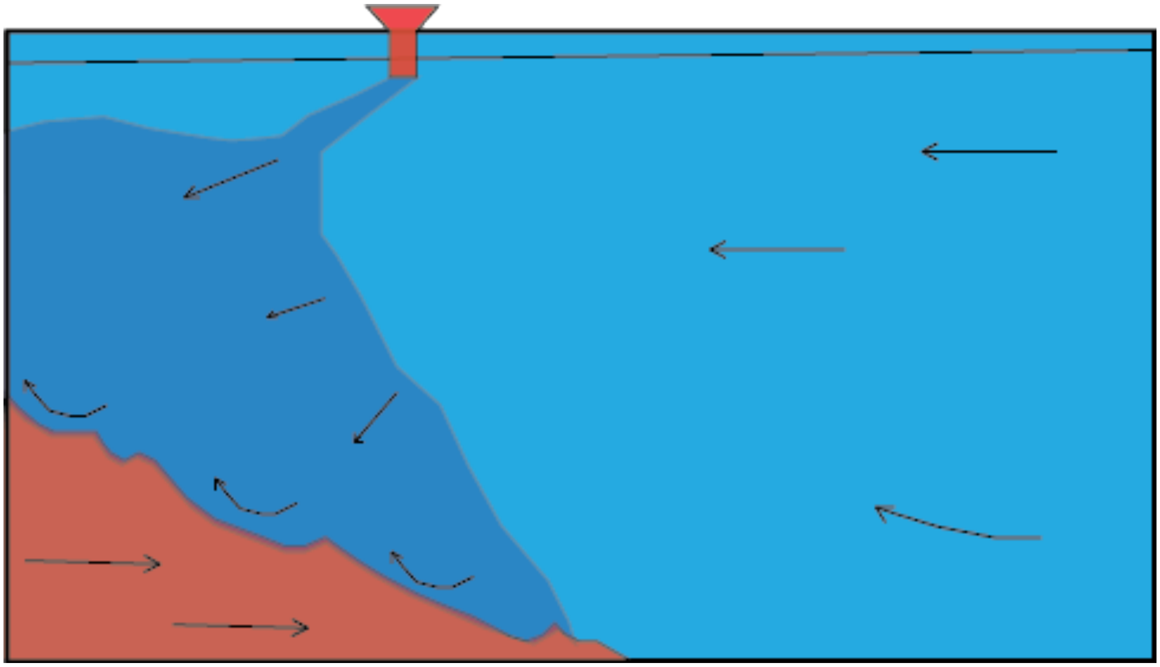

Figure 48. Schematic diagram showing the interpreted interactions of red saltwater (denser) and dark blue saltwater (lighter) along the face of the red saltwater wedge. Scalloping and small upwellings are created along the interface due to competing directional flows of freshwater and a component of upward density-driven flow.

Permeameter Studies

In a separate setup, a constant-head permeameter (Figure 9) was used to determine the hydraulic conductivity of the beads used in the idealized physical tank model. The experiments measure the flow rates Q through a sand layer under a controlled constant head gradient ($\Delta h/\Delta l$). The head gradient can be controlled by adjusting water levels in two constant-head reservoirs. The hydraulic conductivity, K, of tested sample was calculated using Darcy's equation: $Q = -KA\Delta h/\Delta l$. The results of the permeameter experiments are shown in Figure 49 and Table 9. Average hydraulic conductivity was calculated as 0.075 ±0.0115 cm/s. This value falls within the $10^{-3} – 10^{-1}$ cm/s range of a typical unconsolidated sand (Fetter, 2000).

Table 9. Head and volumetric data used to calculate discharge and hydraulic conductivity of glass beads. Constants: chamber height (Δl) = 0.125m; chamber area (A) = 0.003217m^2; time = 180 s.

Head (Δh,m)	Volume (m^3)	Q (m^3/s)	K (m/s)	K (cm/s)
0.61	0.002695	0.0000150	0.000954	0.095
0.71	0.002880	0.0000160	0.000876	0.088
0.81	0.003060	0.0000170	0.000815	0.082
0.91	0.003200	0.0000178	0.000759	0.076
1.01	0.003440	0.0000191	0.000735	0.074
1.11	0.003575	0.0000199	0.000695	0.070
1.21	0.003710	0.0000206	0.000662	0.066
1.31	0.003835	0.0000213	0.000632	0.063
1.41	0.003980	0.0000221	0.000609	0.061

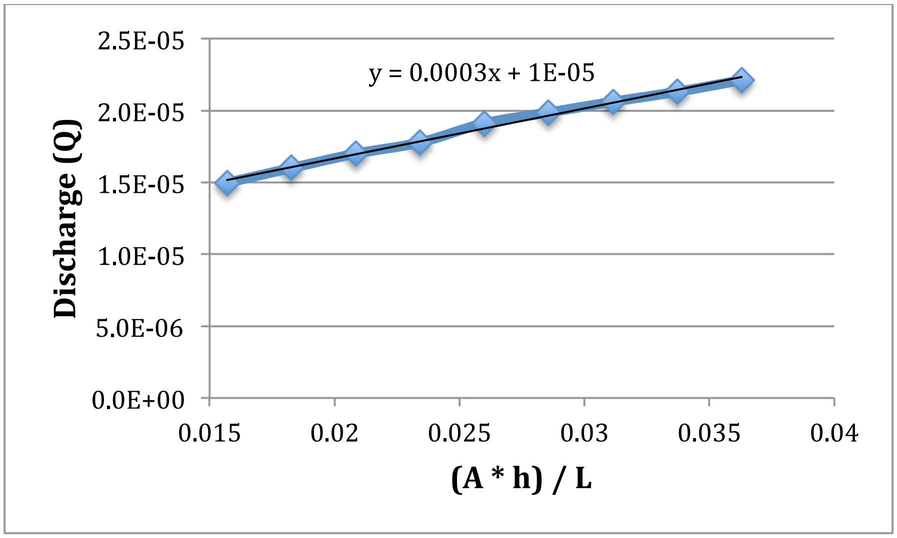

Figure 49. Regression trend of hydraulic conductivity (K) values derived from constant-head permeameter experiments.

Numerical Modeling

Numerical models were constructed using the program Basin2 to simulate saltwater intrusion at the same scales of tank experiments. The physical and numerical models both represent a simplified version of a real world coastal setting.

Steady-State model: The first model (Appendix 3) simulates steady-state hydrologic conditions and accounts for salt transport by advection. Groundwater salinity at the land surface is set to zero and groundwater at the seafloor is set to 0.48 molal, the same as in the tank model. The model domain (Figure 10), 60 cm long, is composed of a sandy layer with permeability of 0.01 darcy (10^{-7} m/s). The permeability of 0.01 darcy is similar to that of fine-grained, silty sand, but lower than that of glass beads used in the tank experiments. Figure 50 illustrates that freshwater table relief (0.4 to 0.2 cm over 60 cm) across the land surface drives the flow of freshwater from right to left. The steady-state model illustrates a saltwater-freshwater interface at equilibrium and the invasion of saltwater along the bottom of the aquifer, as seen in the physical tank experiments. The modeling results also demonstrate how a rise of sea level by 0.2 cm causes the saltwater front to advance upward and landward.

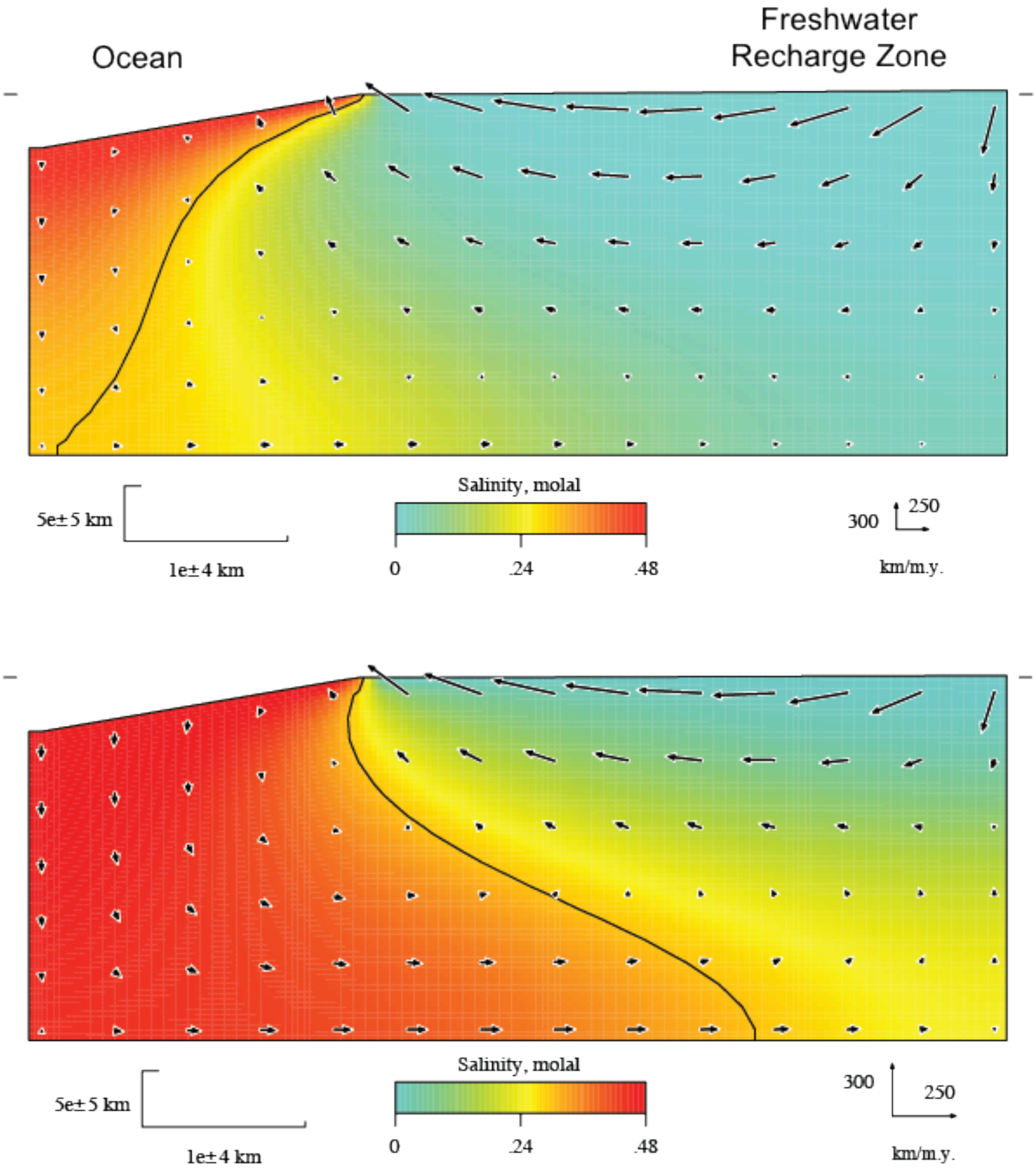

Figure 50. Model results showing predicted groundwater flow and saltwater intrusion under conditions of maximum freshwater table of 0.4 cm (top) and 0.2 cm (bottom) above sea level. Sea-level rise of 0.2 cm causes salty groundwater to move upwards and landwards. Colors map groundwater salinity from 0 (blue, corresponding to freshwater) to 0.48 molal (red, corresponding to seawater). Arrows show predicted flow vectors. Small tick marks denote sea level. A dark contour line tracks the position of salinity level 0.3 molal.

Transient model: The second model (Appendix 3) investigates the interactions over time of two saltwater sources, one from the seafloor and one from the surface. First, the model is given time to develop a stable saltwater-freshwater wedge interface similar to that produced in the steady-state model. Due to limitations of the Basin2 software, time restrictions allow only for a smaller wedge to form over the allotted time. In the simulations, the saltwater front is tracked by a contour of 0.3 molal. Figure 51 shows the early development of a wedge at 200 model years, and Figure 52 shows the growth and propagation of the wedge at the end of 1600 model years. Between 1500 and 3000 model years, an additional source of saltwater of the same salinity was introduced at the surface at a location 40 cm from the left boundary. During this time, the transient model illustrates the movement and interactions of the initial saltwater wedge and a second surficial saltwater source. Figure 53 shows the first introduction of the second, surficial saltwater source. By 2800 years, the surficial saltwater input forms a plume that migrates both downward and to the left, similar to that observed in the tank experiments. The plume's direction of movement is controlled primarily by freshwater table slope and density. Finally, at 3000 model years (Figure 55), the surficial saltwater migrates downward, mixes with freshwater through dispersion, and then flows laterally toward the ocean under the freshwater gradient.

Numerical modeling reveals some insight into possible intrusion dynamics that may explain the presence of crude oil identified in sediments as deep as 15 cm. Similar to the tank models, the numerical models reveal a stable saltwater wedge that intrudes along the deeper aquifer from the left. By contrast, the surficial plume of saltwater infiltrates downward by gravity and laterally by hydraulic gradient, gradually approaching the deep wedge interface. Both tank and numerical models indicate that the MC-252 crude oil could have reached deeper sediments either as a result of infiltration of a surface plume or the intrusion of a deep saltwater wedge from below.

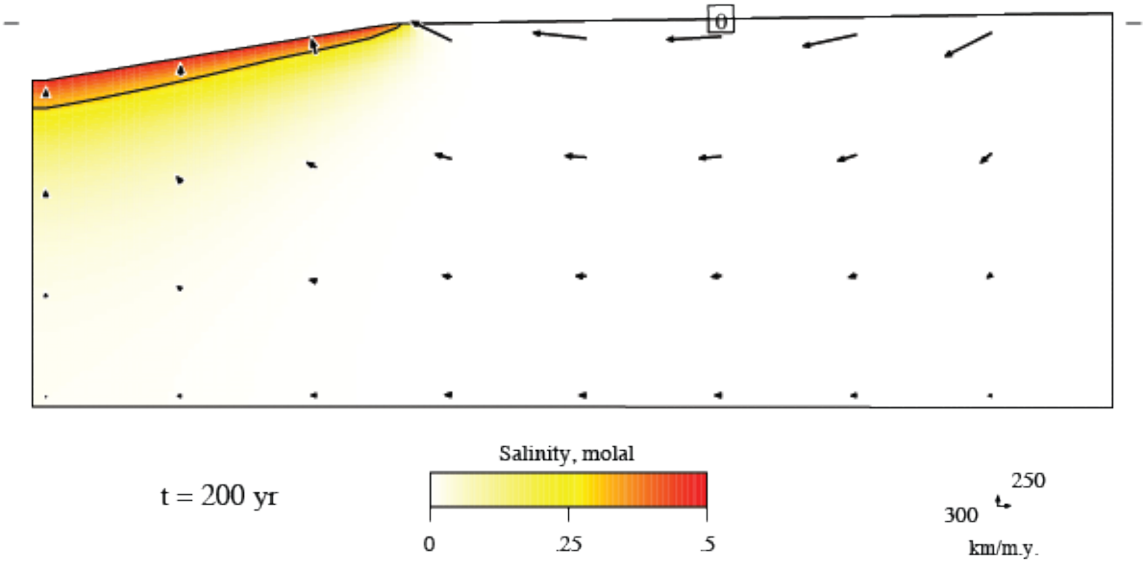

Figure 51. Transient model at 200 model years, the beginning stages of saltwater wedge development.

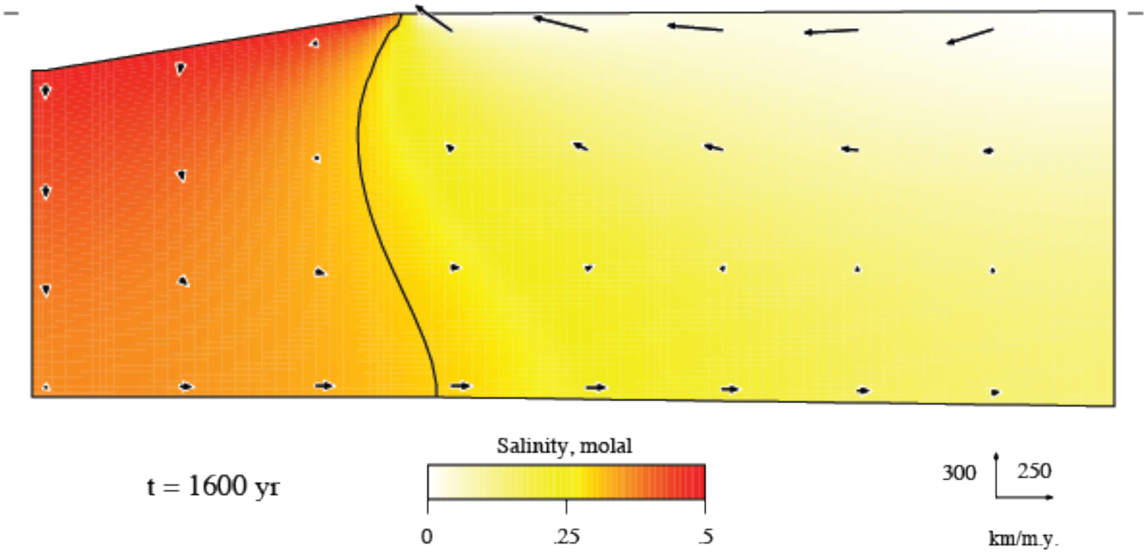

Figure 52. Transient model at 1600 model years, illustrating the extent of a saltwater wedge before a secondary source of surficial saltwater is added to the system (at 1500 model years).

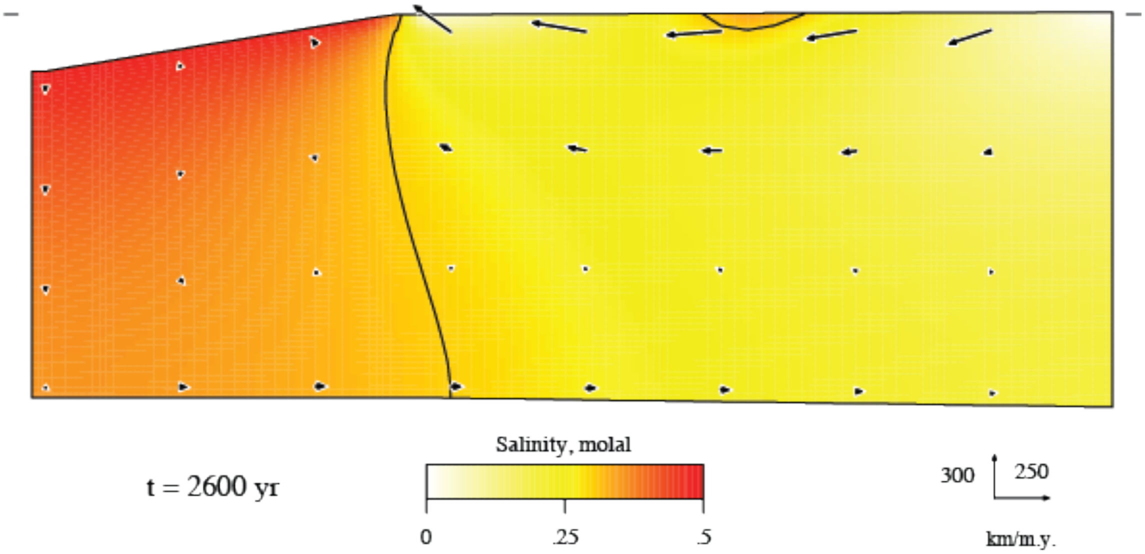

Figure 53. Transient model at 2600 model years, showing the first sign of saltwater infiltration from a secondary surficial point.

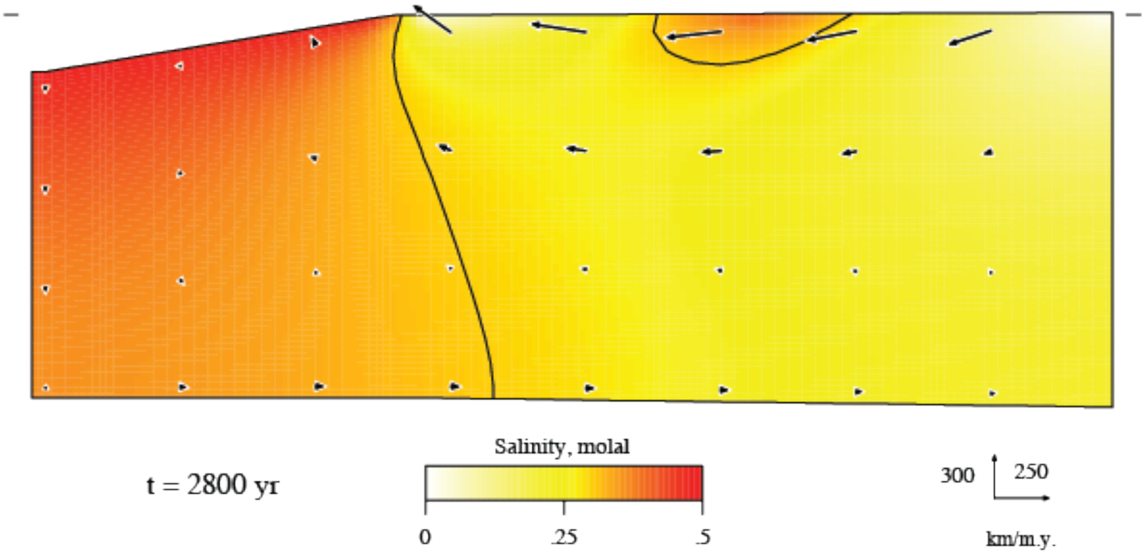

Figure 54. Transient model at 2800 model years as the surficial source of saltwater begins to form a slight plume that primarily migrates downward and toward the saltwater wedge at depth.

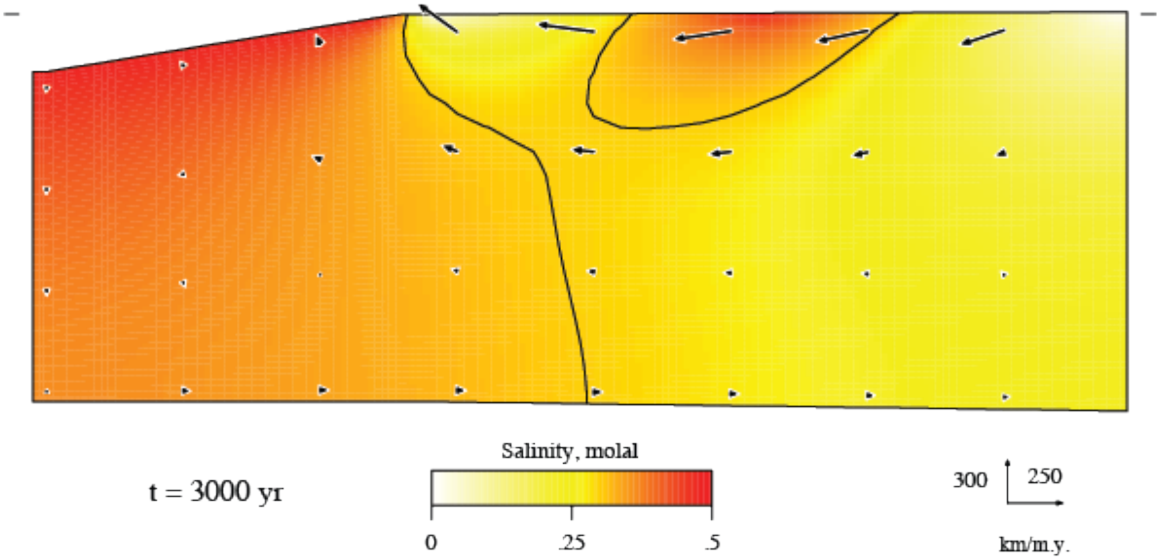

Figure 55. Transient model at 3000 model years, illustrating the impact of the surficial saltwater source on the original saltwater wedge interface.

CONCLUSIONS

This study investigated the fate, transport, and transformation of oil and metal contaminants at ten selected northern Gulf saltmarsh sites (i.e., Bay Jimmy North, Bay Jimmy South, Bayou Dulac, Bay Batiste, Rigolets, Point Aux Chenes Bay, Walker Island, Weeks Bay, Longs Bayou, and Bayou Heron) that were impacted to varying degrees by the 2010 Deepwater Horizon oil spill.

Oil was scraped from plants and extracted from surface sediments and deeper sediments (down to 15 cm) at heavily contaminated saltmarshes. Hydrocarbon fingerprinting via GC-MS and GC-MS-SIM confirms that the source of these oils is the Macondo-1 well of the Deepwater Horizon spill. Weathered oil on plants and in surface sediments is almost entirely Macondo-1 spilled crude; oil recovered from deeper sediments (12-15 cm) is partially MC-252 crude oil but also displays evidence of mixing, possibly with oil from a separate, natural oil seep. Chromatographs also show that weathered MC-252 oils remaining in saltmarshes have been enriched in heavier hydrocarbons by the preferential degradation of lighter hydrocarbons. Furthermore, tarballs brought to the Alabama Gulf shore by Hurricane Isaac, 28 months after the spill, were also positively tied to oil spilled from Macondo-1 by remarkably narrow ranges in selective biomarker ratios: 0.913-1.070 for Ts/Tm (Ts/Tm =18α-22,29,30-trisnorneohopane/17α-22,29,30-trisnorhopane), 0.530-0.586 for C29/C30 norhopane-hopane, 0.792-0.814 for 35S/34S pentakishomohopane-tetrakishomohopane, and 0.507-0.520 for C31S/C30 homohopane-hopane.

GC-MS and LC-MS analyses of dispersant COREXIT 9500A revealed several compounds: light hydrocarbons, dioctyl sodium sulfosuccinate (DOSS), palmitic acid, and a sulfonic acid base to a series of polyethylene glycols (PEGs). Of the compounds identified, DOSS likely acts as the most reliable tracer of COREXIT 9500A in natural environments. DOSS is highly resistant to biodegradation (Kujawinski et al., 2012) and its limited anthropogenic uses will likely allow for a strong correlation of environmental samples to a source. DOSS was identified through

LC-MS at m/z 467.1990. In future studies, it may be determined whether the degradation-resistant COREXIT 9500A dispersant has migrated from the gulf oil slicks to certain coastal saltmarsh environments. If DOSS can be identified at m/z 467.1990 in a sample, it may be used as a conservative biomarker to trace the occurrence and geochemical evolution of dispersant in natural environments.

Physical and numerical models reveal possible intrusion mechanisms responsible for the occurrence of MC-252 crude oil in coastal saltmarsh sediments at depths down to 15 cm. Physical modeling in a laboratory-scale tank reveals dynamic interactions between a deep saltwater wedge and a surficial, onlapping saltwater source. The position of the saltwater wedge is controlled by density and differences in freshwater and saltwater head, whereas the infiltration of surficial saltwater source is controlled by density and the hydraulic gradient of freshwater flow. High activity at the scalloped interface between these two mixing saltwater sources may be enough to entrain heavier compounds of crude oil deeper in the subsurface. Numerical models reveal similar intrusion dynamics; a stable saltwater wedge intrudes along the deeper aquifer from the ocean, whereas the surficial plume of saltwater infiltrates downward by gravity and migrates laterally by hydraulic gradient. Both tank and numerical models indicate that the MC-252 crude oil could have reached deeper sediments either as a result of infiltration of a surface plume or the intrusion of a deep saltwater wedge from below.

The concentrations of various trace metals in pore waters are generally low (a few to hundreds of ppb), despite high levels of those trace metals (on the level of ppm) in sediments. Concentrations of sulfur, arsenic, manganese, and chromium in pore water all display strong correlations with the degree of oil contamination. Sulfur ranges from 249 ppm at pristine sites to 806 ppm at contaminated sites, arsenic from 15 ppb to 21 ppb, manganese from 848 ppb to 3273 ppb, and chromium from 1.9 ppb to 4.9 ppb. Sulfur and iron concentrations in sediments also display a positive correlation with the degree of contamination, as do several trace metals (arsenic, copper, nickel, and cobalt) with moderate to high degrees of trace metal pyritization (DTMP). Manganese and chromium, which typically exhibit a low DTMP, also display a positive correlation with the degree of contamination. It is very likely that the abundance of spilled hydrocarbons, together with bacterially-mediated iron and sulfur reduction, promotes metal sequestration through precipitation of sulfide solids. The formation of sulfide solids may be responsible for the elevated concentrations of metals in sediments relative to their dissolved concentrations in pore water.

Results of geochemical modeling further support the hypothesis that the enhanced respiration of iron- and sulfate-reducing bacteria in coastal saltmarshes results in the sequestration of dissolved trace metals into sulfide solids, such as pyrite. An activity model indicates that pH and H_2S conditions at oiled saltmarshes are clustered within the stability field of pyrite under sulfate-reducing conditions (pE = -3). Enhanced microbial respiration spurred by the oil spill likely created such a reducing environment in which pyrite is thermodynamically stable. Reaction-path modeling of mineral transformations in a ferrous-sulfate system shows the precipitation of pyrite as redox potential (Eh) becomes increasingly negative past an Eh of approximately -0.8 V. Seawater titration models illustrate the impacts of rising pH and the introduction of competing ions. At near-neutral pH, arsenic shows a strong tendency to adsorb to hydrous ferric oxides (HFOs), but when pH rises to 9, arsenic in solution increases by over 500 ug/kg. Furthermore, additional calcium, sulfate, and bicarbonate ions introduced with seawater intrusion encourage desorption of arsenic from HFOs. These competitive ions replace arsenic in the sorbing sites of HFOs, resulting in tens of ug/kg increase of arsenic in solution. By contrast, the sequestration of toxic metals and metalloids such as arsenic into pyrite and HFOs may reduce groundwater contamination. The geochemical modeling results and field data suggest that the mobility and transformation of metals are strongly influenced by Eh, pH, the availability of competing ions, and mineral dissolution/precipitation. Future geochemical fluctuations in these tidally-influenced coastal marshes may prompt desorption of toxic metals such as arsenic from pyrite and HFOs.

REFERENCES

Alvarez-Iglesias, P, and B. Rubio, The degree of trace metal pyritization in subtidal sediments of a mariculture area: Application to the assessment of toxic risk, *Marine Pollution Bulletin*, 56, 973-983, 2008.

Amos, J., BP spill was a greater disaster than public knew, *SkyTruth*, http://mcbi.org/news/PR-Norse-Amos-2010.pdf, 2010.

Arulazhagan, P., N. Vasudevan, and I. T. Yeom, Biodegradation of polycyclic aromatic hydrocarbon by a halotolerant bacterial consortium isolated from marine environment, *International Journal of Environmental Science and Technology*, 4, 639-652, 2010.

Ball, J. S., W. J. Wegner, H. J. Hyden, C. A. Horr, and A. T. Myers, Metal content of twenty-four petroleums, *Journal of Chemical Engineering*, 5, 553-557, 1960.

Berner, R. A., Sedimentary pyrite formation, *American Journal of Science*, 268, 1-23, 1970.

Bethke, C. M., Geochemical and Biogeochemical Reaction Modeling, Cambridge University Press: London, 2008.

BP, Plume Monitoring and Assessment Plan for Subsurface Dispersant Application, *Dispersant Monitoring and Assessment Directive for Subsurface Dispersant Application*, May 10, 2010a.

BP, Re: May 19, 2010 Addendum 2 to Dispersant Monitoring and Assessment Directive, *EPA.gov*, 2010b, <http://www.epa.gov/bpspill/dispersants/5-21bp-response.pdf>. Accessed May 27, 2012.

Burnol, A., and L. Charlet, Fe(II)-Fe(III)-bearing phases as a mineralogical control on the heterogeneity of arsenic in Southeast Asian groundwater, *Environmental Science & Technology*, 44, 7541–7547, 2010.

Cappello, S., G. Caruso, D. Zampino, et al., Microbial community dynamics during assays of harbour oil spill bioremediation: a microscale simulation study, *Journal of Applied Microbiology*, 102, 184-194, 2007.

Crone, T.J., and M. Tolstoy, Magnitude of the 2010 Gulf of Mexico oil leak, *Science*, 330, 634, 2010.

Drever, J. I., *The Geochemistry of Natural Waters*, Prentice Hall: New Jersey, 2nd ed., 1988.

Dzombak, D. A., and F. M. M. Morel, Surface Complexation Modeling, Wiley: New York, 1990.

Edwards, B. R., C. M. Reddy, R. Camilli, et al., Rapid microbial respiration of oil from the Deepwater Horizon spill in offshore surface waters of the Gulf of Mexico, *Environmental Research Letters*, 6, 1-9, 2011.

Essaid, H. I., B. A. Bekins, W. N. Herkelrath, and G. N. Delin, Crude oil at the Bemidji site: 25 years of monitoring, modeling, and understanding, *Groundwater*, 49, 706-726, 2011.

Farquhar, M. L., J. M. Charnock, et al., Mechanisms of arsenic uptake from aqueous solution by interaction with goethite, lepidocrocite, mackinawite, and pyrite: An x-ray absorption spectroscopy study, *Environmental Science & Technology*, 36, 1757-1762, 2002.

Fetter, C. W., Applied Hydrogeology, Prentice Hall: Englewood Cliffs, New Jersey, 2000.

Freeze, R. A., & J. A. Cherry, Groundwater, Prentice Hall: Englewood Cliffs, New Jersey, 1979.

Hem, J. D., Study and interpretation of the chemical characteristics of natural water, *US Geological Survey Water-Supply Paper 2254*, 1985.

Lee, M. K. and J. A. Saunders, Effects of pH on metals precipitation and sorption: Field bioremediation and geochemical modeling approaches, *Vadose Zone Journal*, 2,177-185, 2003.

Hamdan, L. J. and P. A. Fulmer, Effects of COREXIT® EC9500A on bacteria from a beach oiled by the Deepwater Horizon spill, *Aquatic Microbial Ecology*, 63, 101-109, 2011.

Hazen, T. C., E. A. Dubinsky, et al., Deep-sea oil plume enriches indigenous oil-degrading bacteria, *Science*, 330, 204-208, 2010.

Hinkle, S. R., and D. J. Polette, Arsenic in ground water of the Willamette Basin, Oregon, *USGS Water-Resources Investigations Report 98-4205*, 1999.

Iverson, S. A., and D. Esler, Harlequin Duck population injury and recovery dynamics following the 1989 Exxon Valdez oil spill, *Ecological Applications*, 20, 1993-2006, 2010.

Judson, R. S., Martin, M. T., et al., Analysis of either oil spill dispersants using rapid in vitro tests for endocrine and other biological activity, *Environmental Science & Technology*, 44, 5979-5985, 2010.

Karchmer, J. H., and E. L. Gunn, Determination of trace metals in petroleum fractions, *Analytical Geochemistry*, 24, 1733-1741, 1952.

Keevan, J., Assessing transformation of trace metals and crude oil in Mississippi and Louisiana coastal wetlands in response to the Deepwater Horizon oil spill, Masters Thesis, Auburn University, Auburn, Alabama, 2012.

Kleikemper, J., M. H. Scroth, W. V. Sigler, M. Schmucki, et al., Activity and diversity of sulfate-reducing bacteria in a petroleum hydrocarbon-contaminated aquifer, *Applied Environmental Microbiology,* 68, 1516-1523, 2002.

Kujawinski, E. B., M. C. Kido Soule, D. L. Valentine, et al., Fate of dispersants associated with the Deepwater Horizon oil spill, *Environmental Science & Technology*, 45, 1298-1306, 2011.

Lee, M. K., and J. A. Saunders, Effects of pH on metals precipitation and sorption: Field bioremediation and geochemical modeling approaches, *Vadose Zone J*ournal, 2, 177-185, 2003.

Lee, M.-K., J. A. Saunders, R. T. Wilkin, and S. Mohammad, Geochemical modeling of arsenic speciation and mobilization: Implications for bioremediation, in Advances in Arsenic Research: Integration of Experimental and Observational Studies and Implications for Mitigation, *American Chemical Society Symposium Series*, eds. O'Day et al., 915, 398-413, 2005.

Maki, A. W., The Exxon Valdez oil spill: Initial environmental impact assessment, *Environmental Science and Technology*, 25:1, 24-29, 1991.

Marshall, A. G., and R. Podgers, Petroleomics: The next grand challenge for chemical analysis, *Accounts of Chemical Research*, 37, 53-59, 2004.

Morse, J. W., and G. W. Luther III, Chemical influence on trace metal-sulfide interaction in anoxic sediments, *Geochimica et Cosmochimica Acta*, 63, 3373-3378, 1999.

Natter, M., Fate and transformation of oils and trace metals in Alabama and Louisiana coastal marsh sediments associated with the British Petroleum Gulf oil spill, Masters Thesis, Auburn University, Auburn, Alabama, 2012.

Natter, M., J. Keevan, Y. Wang, A. Keimowitz, et al., Level and degradation of Deepwater Horizon spilled oil in coastal marsh sediments and pore-waters, *Environmental Science & Technology*, 46 (11), 5744-5755, 2012.

Obradors, N., and J. Aguilar, Efficient biodegradation of high-molecular-weight polyethylene glycols by pure cultures of Pseduomonas stutzeri, *Applied and Environmental Microbiology*, 57, 2383-2388, 1991.

Oudot, J. and F. Chaillan, Pyrolysis of asphaltenes and biomarkers for the fingerprinting of the Amico Cadiz oil spill after 23 years, *Comptes Rendus Chimie*, 13, 548-552, 2010.

Otero, X.L., M. A. Huerta-Diaz, F. Macías, et al., Influence of turbidite deposit on the extent of pyritization of iron, manganese, and trace metals in sediments from the Guaymas Basin, Gulf of California (Mexico), *Applied Geochemistry*, 18, 1149-1163, 2003.

Padfield, T., J. Winsløw, W. B> Pedersen, and J. Glastrup, Decomposition of polyethylene glycol (PEG) on heating, International Council of Museums – Conservation Committee (ICOM-CC) Conference, Dresden, 243-245, 1990.

Place, B., B. Anderson, A. Mekebri, E. T. Furlong, et al., A role for analytical chemistry in advancing our understanding of the occurrence, fate, and effects of Corexit oil dispersants, *Environmental Science & Technology*, 44, 6016-6018, 2010.

Plante, M., B. Bailey, I. Acworth, and M. Neely, Characterization of dispersants by reversed-phase high-pressure liquid chromatography and charged aerosol detection, *Thermo Scientific*, 2011.

Ribeiro, H., A. P. Mucha, C. M. R. Almeida, et al., Hydrocarbon degradation potential of salt marsh plant-microorganisms associations, *Biodegradation*, 22, 729-739, 2011.

Rosenbauer, R. J. et al., Reconnaissance of Macondo-1 Well oil in sediment and tarballs from the northern Gulf of Mexico Shoreline, Texas to Florida, *USGS Open-File Report 2010-1290*, 2010.

Saunders, J. A., M. K. Lee, M. Shamsudduha, P. Dhakal, A. Uddin, M. T. Chowdury, and K. M. Ahmed, Geochemistry and mineralogy of arsenic in (natural) anaerobic groundwaters, *Applied Geochemistry*, 23, 3205-3214, 2008.

Smedley, P. L., and D. G. Kinniburgh, A review of the source, behavior, and distribution of arsenic in natural waters, *Applied Geochemistry*, 17, 517-568, 2002.

Tyrovola, K., and N. P. Nikolaidis, Arsenic mobility and stabilization in topsoils, *Water Research*, 43, 1589-1596, 2009.

Valentine, D. L., J. D. Kessler, M. C. Redmond, et al., Propane respiration jump-starts microbial response to a deep oil spill, *Sciencexpress*, Report, pp. 5, 2010.

Wang, Z. and S. A. Stout, Oil Spill Environmental Forensics – Fingerprinting and Source Identification, Elsevier: Massachusetts, 2007.

Wang, J. H. and Y. M. Shen, Development of an integrated model system to simulate transport and fate of oil spills in seas, *Science China – Technological Sciences*, 53, 2423-2434, 2010.

Watson, G. K. and N. Jones, The biodegradation of polyethylene glycols by sewage bacteria, *Water Research*, 11, 95-100, 1977.

Ye, S., E. A. Laws, Q. Wu, S. Zhong, et al., Pyritization of trace metals in estuarine sediments and the controlling factors: a case in Jiaojiang Estuary of Zhejiang Province, China, *Environmental Earth Science*, 61, 973-982, 2010.

Ye, S., E. A. Laws, S. Zhong, X. Ding, and S. Pang, Sequestration of metals through association with pyrite in subtidal sediments of the Nanpaishui Estuary on the western bank of the Bohai Sea, China, *Marine Pollution Bulletin*, 62, 934-941, 2011.

APPENDICES

APPENDIX 1 – Microscale Solvent Extraction, derived from EPA Method 3570

Materials:

1. Anhydrous sodium sulfate
2. Sediments
3. PTFE glass extraction tubes
4. 25 mL glass syringe and 25mm syringe filters
5. Dichloromethane (DCM)
6. Rotator
7. Centrifuge
8. Glass pasteur pipettes

Method:

1. Add approximately 5 grams of anhydrous sodium sulfate to a pre-cleaned PTFE extraction tube with a PTFE screw cap.
2. Weigh 3 grams of sediments into the tared extraction tube.
3. Add 10mL of DCM to the extraction tube and cap tightly.
4. Shake the tube vigorously until slurry is free-flowing.
5. Add more sodium sulfate and manually mix as necessary to produce a free-flowing, finely divided slurry.
6. Extract the samples by rotating end over end for at least 24 hours (at 70%).
7. Centrifuge at 3000rpm for 10 minutes.
8. Transfer liquid phase (extract) with pasteur pipette to 16x100mm glass extraction vial.
9. Extract the soil once more by adding approximately 5mL of DCM to the sample, capping the extraction tube tightly, and shaking vigorously by hand for 2 minutes. More sodium sulfate can be added at this point as necessary to dry the extract and break up any clumps that may have formed.
10. Repeat steps 7 to 8.
11. Filter liquid phase using glass syringe and syringe filter to another 16x100mm glass vial.
12. Dry organics in a vent hood with nitrogen gas for 30 minutes.
13. Add 1.5mL of hexane chromatography grade.
14. Transfer the extract to a 2mL auto sampler vial. Add 15ul of internal standard. Cap the vial and store in the freezer until analysis.

APPENDIX 2 – Pore Water pH and H2S (ppb) Data (from Natter et al., 2012)

	pH	H2S
RG	7.4	8860
Bayou Dulac (BD)	6.88	30
	7.01	4400
	7.10	23520
	7.71	28960
	7.63	41840
	7.65	58680
	7.60	53600
	7.61	46000
Bay Batiste (BB)	7.58	4150
	7.57	19480
	7.59	26920
	8.04	33080
	7.84	32960
	7.67	41280
	7.69	44640
	7.78	48000
	7.90	49200
	7.86	30800
Bay Jimmy North (BJN)	6.60	270
	6.71	4820
	7.12	20120
	7.33	35340
	7.40	54240
	7.43	50800
	7.42	69100
	7.47	65100
	7.45	70400
	7.51	82800
Bay Jimmy South (BJS)	6.62	10
	6.75	240
	6.70	4620
	6.85	6320
	6.95	9120
	7.25	7520
	7.30	8320
	7.28	6640
	7.40	4060
	7.52	2780

APPENDIX 3 – Basin2 Input Files

Basin2 Input File: Steady-State Model

```
run = steady; start = 0 yrs
nx = 40;  delta_z = 2 cm
temperature = vertical; heat_flow = 1 HFU
salinity = full; salt_flux = 0
left = closed, right = closed


rock ss
    B_perm = -1.12; A_perm = 0
    alpha_L = 0; alpha_t = 0
end_rock


x_well(cm)  0  20  21  60


strat 'Upper beds'
    t_dep = 0 yrs
    X(ss) = 100%
    column    water_depth(cm)  thickness(cm)  surface_conc(molal)
    w(1)          5              27                 0.48
    w(2)          0              32                 0.48
    w(3)          0              32                 0.0
    w(4)         -0.2            32.2               0.0
```

Basin2 Input File: Transient Model

```
run = transient; start = 0 yrs; end = 3000 yrs
nx = 40;  delta_z = 2 cm
temperature = vertical; heat_flow = 1 HFU
salinity = full; salt_flux = 0
left = closed; right = closed
print_step = 200 yrs


rock ss
    B_perm = -1.12; A_perm = 0
    alpha_L = 0; alpha_t = 0
end_rock
```

```
x_well(m)  0   0.2  0.21  0.4  0.6


strat 'Upper beds'
    t_dep = 0 yrs
    X(ss) = 100%
    column    water_depth(cm)  thickness(cm)  surface_conc(molal)

    w(1)            5             27                0.48
    w(2)            0             32                0.48
    w(3)            0             32                0.0
    w(4)            &              &                0.0
    w(5)           -1.0           33                0.0


strat 'Upper beds'
    t_dep = 1500 yrs
    X(ss) = 100%
    column    water_depth(cm)  thickness(cm)  surface_conc(molal)

    w(1)            5             0                0.48
    w(2)            0             0                0.48
    w(3)            0             0                0.0
    w(4)            &             &                0.0
    w(5)           -0.2           0                0.0


strat 'Upper beds'
    t_dep = 3000 yrs
    X(ss) = 100%
    column    water_depth(cm)  thickness(cm)  surface_conc(molal)

    w(1)            5             0                0.48
    w(2)            0             0                0.48
    w(3)            0             0                0.0
    w(4)            &             &                0.48
    w(5)           -0.2           0                0.0
```